# MICROCELLULAR PROCESSING OF FLUOROPOLYMERS AND THE DESIGN OF A MICROCELLULAR FOAM EXTRUSION SYSTEM FOR WIRE COATING

by

**RAVI R. PATIL**

S.B., Mechanical Engineering
Massachusetts Institute of Technology
1993

Submitted to the Department of Mechanical Engineering
in Partial Fulfillment of the Requirements for
the Degree of

MASTER OF SCIENCE
IN MECHANICAL ENGINEERING

at the

MASSACHUSETTS INSTITUTE OF TECHNOLOGY

June 1995

Signature of Author______________________________
Department of Mechanical Engineering
March 31, 1995

Certified by______________________________
Nam P. Suh
The Ralph E. and Eloise F. Cross Professor of Manufacturing
Head of the Department of Mechanical Engineering
Thesis Advisor

Accepted by______________________________
Ain A. Sonin
Professor of Mechanical Engineering
Chairman of the Departmental Graduate Committee
Department of Mechanical Engineering

# MICROCELLULAR PROCESSING OF FLUOROPOLYMERS AND THE DESIGN OF A MICROCELLULAR FOAM EXTRUSION SYSTEM FOR WIRE COATING

by

**RAVI R. PATIL**

Submitted to the Department of Mechanical Engineering on March 31, 1995
in Partial Fulfillment of the Requirements for the Degree of
Master of Science in Mechanical Engineering

## ABSTRACT

Microcellular plastics are foamed plastics characterized by cell sizes smaller than 10 μm and cell densities in excess of $10^9$ cells/cm$^3$. This thesis addresses microcellular polymer processing in the context of the wire coating industry. Due to their exceptionally low dielectric constants, fluoropolymers commonly serve as the dielectric insulation in coaxial cables. A microcellular coating of such materials on the cable can significantly improve electrical performance. The first phase of research identified the key microcellular processing parameters for two different semicrystalline fluoropolymers, DuPont FEP 4100 and DuPont PFA 440 HP. In addition, weight gain experimentation revealed that both polymers exhibited induced crystallinity as a result of carbon dioxide sorption. The second phase of research implemented a newly designed scaled-up microcellular foam extrusion system featuring a gear pump as the cell nucleation device. Preliminary experimentation with Union Carbide DFD-6005 Natural low density polyethylene and Quantum Petrothene 1610-PF polypropylene revealed that gear pump nucleation produced submicron-sized cells which were neither affected by gear teeth memory effects nor shear effects in the wire coating processing dies.

Thesis Supervisor: Nam P. Suh, Ph.D.
Title: The Ralph E. and Eloise F. Cross Professor of Manufacturing
Head of the Department of Mechanical Engineering

# ACKNOWLEDGMENTS

I would first like to thank Professor Nam P. Suh for his guidance during the past two years. I appreciate the confidence he bestowed upon me from the very beginning. His visionary thinking has shown me that nothing is impossible.

None of this research would have been possible without the financial support of Dr. Howard Peiffer at AMP, Inc., and the guidance of Dr. Gene Skiens at Precision Interconnect. Thank you. Gene coordinated the research project and was instrumental in transferring one of PI's manufacturing-scale wire coating extrusion lines to MIT. Art Buck deserves special thanks in this regard for his confidence in letting a group of eager students permanently alter his extrusion equipment. (I hope he can still recognize it when we're all through!) I have to extend many many thanks to Doris Beck for her speedy responses to my constant barrage of questions and her words of encouragement as we solved one problem, only to encounter a host of others. All the folks at Precision Interconnect were extremely supportive from day one and it was a thrill to work with such a good-natured group of people.

Novacor, Quantum Chemical Corporation, and Union Carbide generously donated hundreds of pounds of polymers for the extrusion experiments. Maurice Bowman at DuPont provided the FEP and PFA samples for the batch processing investigation. Finally, Willem Melis at American Lewa was particularly kind with his quick arrangements to have the metering pump repaired. All these companies are thanked for their support as well.

I have made many valuable friendships during my stay at the Microcellular Plastics Lab. Dr. Dan Baldwin was the first to introduce me to the graduate world of MIT. He was especially keen on keeping the lab focused on its main priorities. Thanks so much for your advice. Likewise, Dr. Sung Cha was very helpful with his mystical intuition for batch microcellular processing. I would also like to thank Dr. Chul Park for our informative telephone conversations regarding microcellular extrusion. Dr. Mohsen Mosleh and Jorge Arinez of the Tribology Group are thanked for their companionship and support as we all worked to keep research moving in the Basement of Building 35. Toshi Ota remained amazingly calm and cheerful throughout all the struggles and unknowingly taught me the virtue of patience. I would like to thank Derrick Tate for his friendship and our unforgettable philosophical discussions about pursuing a Ph.D. I wish him all the best as he undertakes the challenge. I would also like to thank Yoddhojit Sanyal for his friendship, enthusiasm, and his solid mastery of thermodynamics and fluid mechanics. I sincerely hope the new extrusion system treats him well as he works towards his doctorate. The same well wishes are extended to Chin Yee Ng who has the challenging task of improving the wire coating system. Finally, Torsten Herrmann deserves a million thanks for relaying a portion of his polymer processing expertise to me during the course of the project. It was "the ultimate engineering experience" working with him on such a large-scale project. I certainly would not have made such progress without his assistance and companionship. Thanks again to everyone in the lab; I trust we will be in touch throughout the years to come.

There were several undergraduate assistants who heroically donated their time and efforts to our research project. Microcellular foaming of Teflon could not have been possible without Sharon John's diligent investigation. I owe her many thanks for running countless experiments and patiently overcoming the intricacies of batch processing. During the final months, Hung Hoang and Sieu Tru Duong, our undergraduate research assistants, were particularly helpful in setting up the extrusion system. They quickly machined many of the "invisible" components of the system and also helped prepare samples for the SEM. In particular, Sieu deserves a standing ovation for his unbelievable dedication to the project. He went beyond the call of duty too many times to count and his chocoholicity provided us with that extra burst of energy to keep on working.

Doris Elsemiller receives my unending thanks for keeping the ship afloat. She went out of her way practically every day to help us with requisitions and scheduling. Thank you very much. The same thanks are due for Maggie Beucler, Joel Gray, Ann Seaman, and Beverly Walker. Leslie Regan's words of encouragement were always spoken when needed the most.

Installing a manufacturing extrusion system required the synthesis of many people's talents. Fred Coté was the knight-in-shining-armor who always had a solution to our problems as well as the tools to implement those solutions. He is really the cornerstone of the LMP experience and I give him a heartfelt thanks for transforming a mechanical scientist into a mechanical engineer. Gerry Wentworth was extremely supportive with his assistance on the extruder/gear pump flanges. His confidence and expertise saved the day countless times. Norm Berube and Victor Lerman had a magical touch all of their own in the machine shop and it was exciting to see it in action. Thanks for your help (especially during the removal of purge stem valve!). Dr. Nannaji Saka defied all kinds of laws. I can't thank him enough for dropping by the lab unexpectedly and offering his witty advice. Kevin Baron, Dorothy Cavignano, Heather Cole, Dr. Greg Dillon, Bob Kane, Kathy Larson, and Karuna Mohindra were also very helpful during the crusade to relocate our lab to Albany Street. Robin Elices and Jim Coffin at the Magnet Lab went out of their way to help the group start from scratch in a new location. Sally Stiffler is thanked for allowing the MCP Group to charge the research account with all the expensive equipment needed to construct the extrusion system. Dr. Andre Sharon's financial support is gratefully acknowledged.

The people who really saw me through the grinder are my friends. It is going to be impossible to express my full gratitude to them and even harder to say good-bye: Laura Bonner, Steve Cimaszewski, Darrell Fruth, Angie Hinrichs, Jack Holt, Anne Kohnen, Marco Morales, Neal Mitra, Adam Nyman, Jason Olsen, James Page, Hoa Pham, Mehrdad Sarlak, Tushar Shah, Joel Sindelar, Goro Tamai, Sekhar Tatikonda, and Sara Zion. Thank you. They should all know that they defined the "MIT experience" and will be sorely missed. I am especially grateful to Tushar, Sara, Sekhar, Anne, and Jack for their beaming smiles and laughter. :) I extend many thanks to Paul "Bono" Hewson, Dave "Edge" Evans, Adam Clayton, and Larry Mullen, Jr., for producing some of the world's most amazing music and keeping my spirits soaring all these years. I think I have finally found what I am looking for.

The unwavering support that I have received from my family has always been greatly appreciated. My successes are a tribute to their love and encouragement. I thank them every day for giving me the opportunity to attend MIT.

"In God's Country"

*Desert sky*
*Dream beneath a desert sky*
*The rivers run*
*But soon run dry*
*We need new dreams tonight...*

U2

# TABLE OF CONTENTS

# *LIST OF FIGURES*

# LIST OF TABLES

# NOMENCLATURE

| | |
|---|---|
| $a$ | shield correction factor [in] |
| $A$ | capacitor plate area [$m^2$] |
| $c_{eq}$ | equilibrium concentration of gas in a polymer [kg(gas)/kg(polymer)] |
| $C$ | capacitance [F] |
| $C_o$ | capacitance in absence of dielectric insulation [F] |
| $d$ | distance between parallel plates of capacitor [m] |
| $d'$ | thickness of dielectric insulation in partially filled capacitor [m] |
| $d_{bw}$ | diameter of the bare wire [in] |
| $d_{cw}$ | outer diameter of the coated wire [in] |
| $D_D$ | inner diameter of the die opening [in] |
| $D_T$ | outer diameter of the guider tip [in] |
| $DDR$ | draw down ratio [dimensionless] |
| $DRB$ | draw ratio balance [dimensionless] |
| $\vec{E}$ | electric field in absence of dielectric insulation [V/m] |
| $\vec{E}_{free}$ | total electric field [V/m] |
| $f$ | stranded correction factor [dimensionless] |
| $F$ | frequency [MHz] |
| $H$ | annular die opening [in] |
| $L$ | length of the coaxial cable [m] |
| $L$ | die land length [in] |
| $\mathrm{p}$ | hydrostatic or thermodynamic pressure [Pa] |
| $P$ | pressure drop across die land [psi] |
| $q$ | volumetric flow rate [$in^3$/sec] |
| $Q$ | electrical charge [C] |
| $Q_{bound}$ | bound charge on dielectric [C] |
| $Q_{free}$ | charge in absence of dielectric insulation [C] |
| $Q_{\max}$ | maximum extrusion rate [lbs/hr] |
| $Q_{total}$ | total charge [C] |
| $r_{bw}$ | radius of the bare wire [m] |
| $r_{cw}$ | radius of the coated wire [m] |
| $R_t$ | total line resistance [ohms/mft] |
| $t_d$ | time delay [nsec/ft] |

| | |
|---|---|
| T | absolute temperature [K] |
| $W$ | average die circumference [in] |
| $V_{\max}^{wire}$ | maximum wire coating rate [ft/min] |
| $V_{prop}$ | normalized propagation velocity of electric energy [dimensionless] |
| $\Delta V$ | potential difference [V] |
| $\Delta V_o$ | potential difference in absence of dielectric insulation [V] |
| $Z_o$ | cable impedance [ohms] |

| | |
|---|---|
| $\varepsilon_o$ | permittivity constant [$C^2/N\text{-}m^2$] |
| $\dot{\gamma}_{cr}$ | critical shear rate [$sec^{-1}$] |
| $\dot{\gamma}_w$ | estimated shear rate at wall [$sec^{-1}$] |
| $\kappa$ | dielectric constant [dimensionless] |
| $\lambda$ | power factor [dimensionless] |
| $\rho$ | polymer melt density [$lbs/in^3$] |
| $\tau_w$ | estimated shear stress at wall [psi] |
| $\Gamma$ | attenuation [decibels/ft] |

# *CHAPTER 1*

# *INTRODUCTION*

## 1.0 Introduction

As worldwide competition in the manufacturing sector continues to grow fiercely, product and process engineers are striving to reduce material consumption to lower costs while retaining product functionality and improving product quality. As compliance with environmental regulations becomes increasingly tough, manufacturing decisions are further complicated. These issues are omnipresent in the polymer processing industry where demand for plastic parts has skyrocketed during the past few decades. Since roughly 75% of the total cost of mass-produced plastic parts is the material cost, reducing material usage can offer handsome cost benefits. Researchers at the Massachusetts Institute of Technology have developed an environmentally-friendly means to produce very unique polymer foams known as *microcellular plastics* which possess high density reductions and often improved material properties. This thesis addresses microcellular processing in the context of an important manufacturing process called wire coating.

## 1.1 Motivations for Research

The wire and cable industry is the single largest consumer of plastics in the electronics business, comprising roughly half of the total polymer consumption (Graff, 1993). Coaxial cables manufactured from wires as small as 1 mil in diameter are used by the communications, test equipment, and medical industries. The conventional manufacturing process consists of winding dielectric insulation in the form of a porous Teflon® tape around the cable.† The dielectric insulation not only separates the conducting wire from the grounded sheath located outside the wire, as shown in Figure 1.1, but also reduces the possibility of crosstalk between cables. Since the trend in technology has been towards the miniaturization of components, it is common for hundreds of coaxial cables to be placed in one bundle, thus making crosstalk an important issue. It is preferable to use as low a dielectric constant material as possible since lower dielectric constants permit faster

---

† Teflon® is the registered trademark for DuPont fluoropolymers.

data transmission across the wire. The implications for the supercomputing industry are evident.

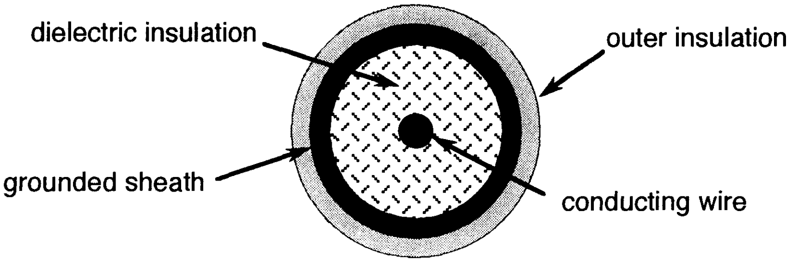

*Figure 1.1: Cross section of a coaxial cable.*

The current tape-winding process is very slow and difficult to control. It is, in fact, the most time consuming step in the manufacture of a complete coaxial cable. As the tape is wound around the cable, a certain region of tape overlap is necessary to completely cover the conducting wire. This overlap leads to an undesirable periodic nonuniformity in the insulation coating thickness as shown in Figure 1.2, making it impossible to maintain a constant outer diameter. The complications of tape winding are also manifested during product use. During installation or routing, the Teflon tape can kink and possibly tear if the cable undergoes a 90° bend. Any breakage in the insulation degrades performance and can lead to failure of the coaxial cable. Tape kinking becomes a crucial issue if the cable must move or flex during operation, as in the case of medical imaging equipment which navigates through a patient's digestive system, for example.

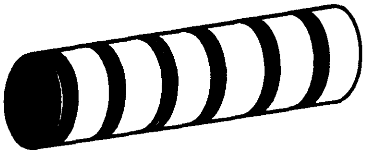

*Figure 1.2: Tape overlap during conventional winding process.*

Since there are numerous difficulties with tape winding, other innovative techniques should be sought if manufacturing costs are to be decreased and product quality is to be improved. One such solution is the continuous extrusion of microcellular foamed Teflon directly around the conducting wire. In comparison with tape winding, extruding the insulation is a substantially faster process and enables constant coating thicknesses. These two advantages are common to extrusion in general; however, the use of microcellular extrusion will capitalize on the unique material properties of the foamed product, namely, the dielectric constant. This property characterizes the material's ability to reduce the strength of an electric field. By introducing billions of voids into the material, the dielectric constant of the material decreases since the air gaps reduce the effective electric field.

Microcellular plastics are foamed plastics characterized by cell sizes smaller than 10 μm and cell densities in excess of $10^9$ cells/cm$^3$. By controlling the cell morphology, the dielectric constant can be tailored to suit the specific need. If very thin foamed coatings are extruded around the cable, the density reduction will result in both materials savings and improved performance since lower dielectric constants translate into faster data transmission speeds.

## 1.2 Microcellular Plastics

As mentioned earlier, microcellular plastics are a relatively new type of polymeric foam characterized by cell sizes smaller than 10 μm and cell densities greater than $10^9$ cells/cm$^3$. Figure 1.3 presents a scanning electron micrograph of a typical microcellular foam. Such cell morphology was motivated by the desire to reduce material consumption in mass-produced plastic parts without compromising mechanical performance. In fact, by producing cell sizes smaller than the natural flaws preexisting in the original polymer, microcellular foams often offer superior thermal, mechanical, and electrical properties in comparison to the unfoamed polymer. (The terms *cellular polymer*, *foamed plastic*, *expanded plastic*, and *plastic foam* are used interchangeably in current literature.) Microcellular plastics boast high stiffness-to-weight ratios, high impact strengths, high toughnesses, high fatigue lives, low thermal conductivities, and low dielectric constants. Toughness and fatigue life for microcellular plastics have shown a five-fold and fourteen-fold increase over the unfoamed polymers, respectively, while the stiffness-to-weight ratio increased by a factor of three to five (Collias and Baird, 1992; Seeler and Kumar, 1992, 1993). Density reductions commonly range from 30-50%. In addition, microcellular foam has a smooth surface finish. Due to these unique material properties, microcellular plastics will find diverse applications, from packaging containers and electrical insulation to automotive parts and even possibly molecular-grade filters.

Another advantage of microcellular processing is that it uses relatively environmentally-safe inert gases such as carbon dioxide and nitrogen, rather than the chlorofluorocarbons (CFCs) and hydrocarbons which are employed by conventional foam processing. CFCs are known to destroy the earth's ozone layer, and since their production is rapidly being phased out, safer foaming methods such as a microcellular processing are urgently needed. The Montreal Protocol, approved by 140 industrialized nations in 1987, originally banned CFC production and consumption by the year 2000. In 1990, however,

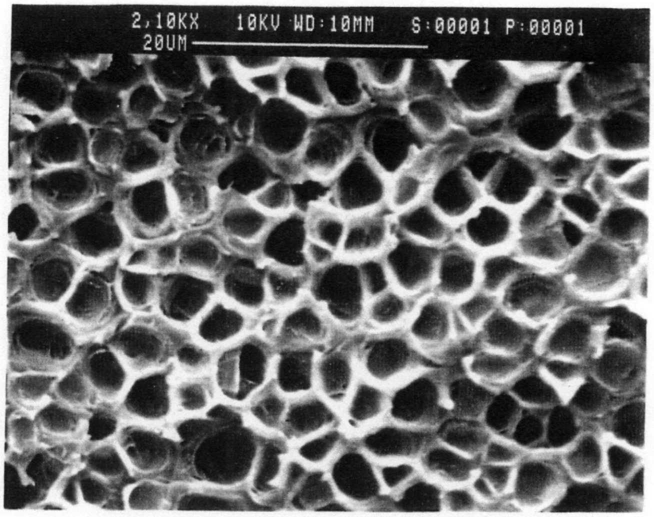

*Figure 1.3: SEM micrograph of microcellular polycarbonate.*

mounting environmental concerns prompted the participating nations to move the deadline back to January 1, 1996 (French, 1994). The U.S. phaseout goal is 1995 (Graff, 1992). Figure 1.4 reveals the effect of governmental regulation on the production of various CFCs, as reported by the 13 international companies participating in the study (AFEAS, 1993). Microcellular processing will receive considerable attention as these deadlines approach.

Microcellular processing technology has been applied to most polymers including amorphous thermoplastics, semicrystalline thermoplastics, liquid crystal polymers, elastomers, and thermosets to produce a closed-celled structure. This thesis extends microcellular processing to an important class of semicrystalline polymers known as *fluoropolymers*. FEP and PFA fluoropolymers are commonly used as dielectric insulation because of their extremely low dielectric constants. These materials also maintain their material properties over a wide range of temperature and electrical frequencies.

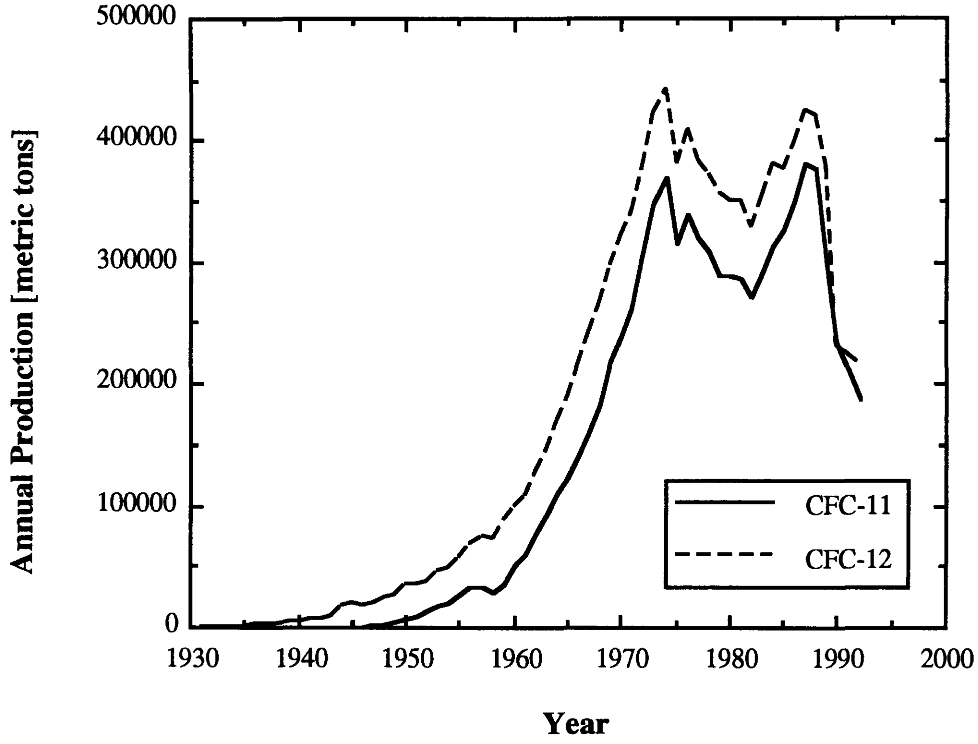

*Figure 1.4: Total annual production of CFC-11 and CFC-12.*

## 1.3 Research Objectives

The ultimate goal of the sponsored research is to develop the technology and processing to produce a microcellular plastic foam-coated wire with the desired cell size, cell density, and coating thickness. Fluoropolymers are the materials of choice because of their exceptionally low dielectric constants. There are complications with extruding such polymers, however. At the required elevated processing temperatures for fluoropolymers, the fluorine atoms in the polymer network become corrosive to many metals. For this reason, extruder barrels and dies used to process fluoropolymers are typically made from corrosion-resistant nickel-based alloys which are considerably more expensive than heat-treated steel and are inconvenient for machining purposes. Since extrusion of fluoropolymers requires specialized equipment not currently available to the MIT Microcellular Plastics Laboratory, extrusion of microcellular plastics will begin with low density polyethylene (PE-LD) and polypropylene (PP) because these materials have sufficiently low dielectric constants and have been successfully processed with microcellular extrusion technology (Park, 1993; Cha, 1994). The current microcellular extrusion system suffers from instabilities which prohibit processing for long periods of time. Since maintaining system stability is crucial if entire spools of wire are to be coated, the research will also modify the existing extrusion system to enable manufacturing processing rates.

Fluoropolymers will still be investigated, however, on the batch processing level to determine the feasibility of microcellular foaming such materials. The batch investigation will identify the key microcellular processing parameters. This information will be invaluable for future research focused on continuous microcellular processing of fluoropolymers.

## 1.4 Thesis Overview

To summarize, the objectives of this thesis are two-fold:

- Assess the batch foaming characteristics of DuPont FEP 4100 and PFA 440 HP
- Design and construct a scaled-up microcellular extrusion system and evaluate its microcellular processing capabilities for wire coating

The thesis begins by contrasting conventional foam processing and microcellular processing in chapter two. The manufacturing methods for conventional foams are briefly discussed followed by the historical background as well as processing issues for microcellular foams. Chapter three presents all the experimental setups and results of the batch processing investigation of fluoropolymers. Chapter four commences the analysis of extrusion processing. The prototype microcellular extrusion system is discussed and provides a basis for understanding the scaled-up microcellular extrusion system implemented in this research. The details of the scaled-up extrusion system are presented in great detail while the specific aspects of wire coating are addressed at the end of the chapter. A treatment of the some of the theoretical issues of coaxial cable performance is provided in chapter five. Chapter six delineates the extrusion procedure and the preliminary results of the extrusion experimentation. Chapter seven finally revisits the goals of the research and summarizes the key results. The thesis concludes with recommendations for future work.

# CHAPTER 2

# BACKGROUND OF POLYMER FOAM PROCESSING

## 2.0 Introduction

Microcellular plastics have the potential to revolutionize numerous fields due to their remarkable properties. Before specifically addressing the issues of wire coating, however, it is important to understand how these unique foams are processed. This chapter highlights the main differences between conventional foam processing and microcellular foam processing in greater detail. The fundamentals of batch microcellular foaming are subsequently explained. The chapter concludes with a glimpse of microcellular extrusion.

## 2.1 Conventional Foam Processing

Foams made from thermoplastics, thermosets, and elastomers are widely in use today, from picnic coolers to seat cushions to packaging material. The creation of a cellular structure can offer advantageous thermal and mechanical properties. Foams possess low thermal conductivities and serve as excellent insulation material. They can also withstand large compressive strains at nearly constant stress. This characteristic makes polymer foams an excellent choice for cushioning materials where large amounts of energy should be absorbed without generating high stresses (Gibson, 1988).

Polymer foams exist as either closed-celled or open-celled structures. The closed-cell variety contains discrete voids randomly interspersed throughout the polymer matrix. Open-celled foams, on the other hand, have interconnected passages as a result of a co-continuous network of voids. Because of these interconnected pores, open-celled foams are commonly used as filters.

Conventional polymer foams are produced using chemical or physical blowing (nucleating) agents. Chemical blowing agents are substances which decompose within a narrow high temperature band and are usually blended with the polymer. As the polymer pellets melt in an extruder, for example, the chemical agents decompose and liberate gases which foam the polymer. The decomposition products should not be corrosive and should not discolor the polymer resin. Physical blowing agents, on the other hand, are gases or volatile liquids that produce bubbles in the molten polymer as a result of undergoing a temperature increase or pressure decrease. Physical agents should ideally have a high solubility in the polymer resin and should vaporize quickly during expansion (Hensen, 1988). Chlorofluorocarbons are commonly used physical agents because they satisfy both requirements and additionally have a low price per unit weight. Since these substances are destructive to the ozone layer and will be phased out in the U.S. by 1995, alternatives to CFC-assisted foaming should be developed, especially since some CFCs are produced mainly for the foam processing industries, as shown in Figure 2.1. This graph displays the annual usage breakdown for CFC-11.

Conventional foams have cell sizes ranging from 100 μm to 2 mm and cell densities ranging from $10^3$-$10^6$ cells/cm$^3$. Because cell nucleation is dependent on the location and size of the blowing agent, the cell sizes and densities are limited to this range and can be highly nonuniform throughout the foam. Nonuniformity in cellular structure leads to degradation of mechanical performance. Figure 2.2 demonstrates the limitation on cell size while processing with a typical nucleation agent (Hensen, 1988).

## 2.2 Microcellular Foam Processing

In contrast, microcellular plastics are polymer foams having cell sizes smaller than 10 μm and cell densities ranging from $10^9$-$10^{12}$ cells/cm$^3$. Because a large amount of gas is dissolved into the polymer matrix, as high as 20% by weight, the resulting cell size distributions are very uniform. Microcellular foaming produces cell sizes two orders of magnitude smaller than conventional foams and cell densities three orders of magnitude greater than conventional foams. The use of environmentally-friendly gases makes this relatively new foaming technique an ideal alternative to conventional processing.

### 2.2.1 Historical Development

Microcellular plastics were invented in the early 1980's by researchers at the Massachusetts Institute of Technology in response to Eastman Kodak Company's desire to reduce the material usage in the manufacture of one of their mass-produced film cartridges

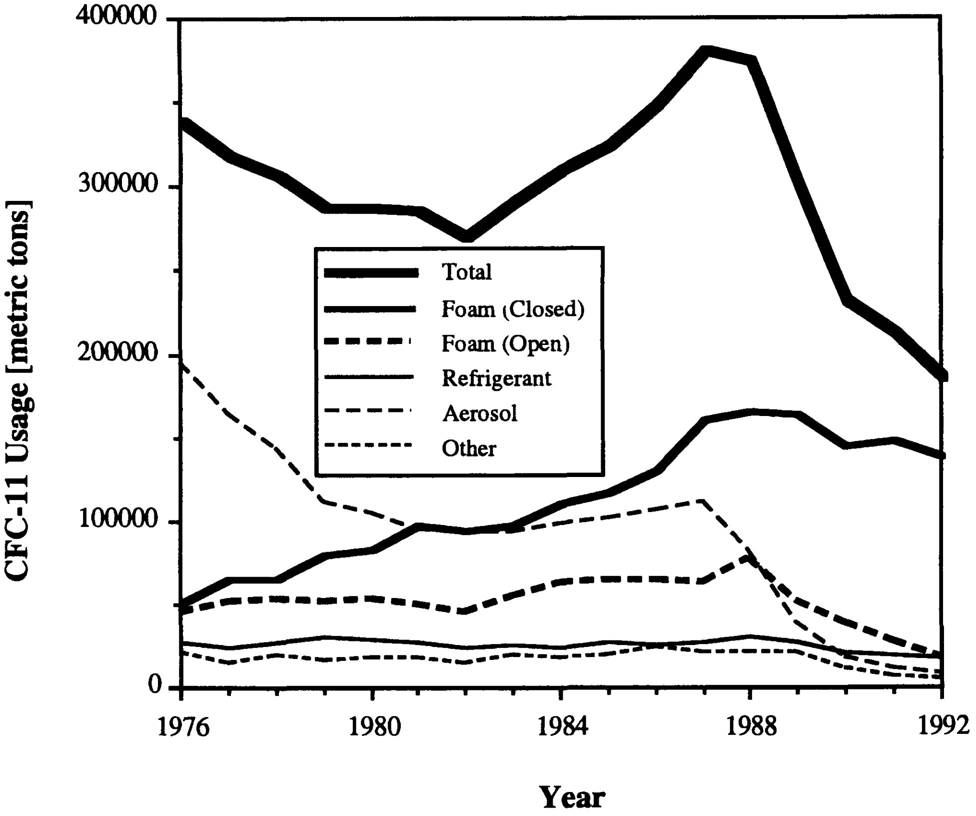

*Figure 2.1: Breakdown by usage for CFC-11.*

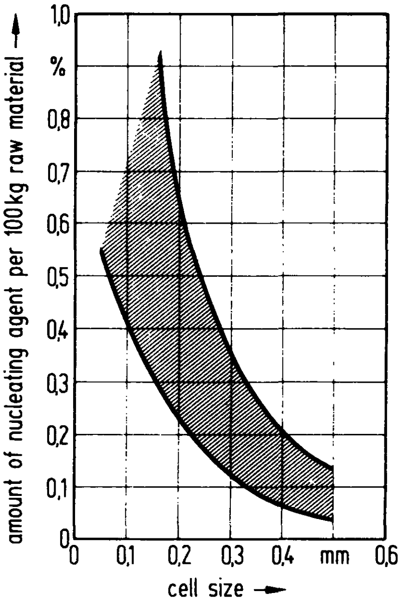

*Figure 2.2: Cell size as a function of amount of nucleating agent.*

without compromising the mechanical properties of the original material (Martini-Vvedensky et al., 1984). The processing technique has been applied successfully to many polymers including amorphous and semicrystalline thermoplastics, liquid crystal polymers, elastomers, and thermosets. Much of the early work focused on applying the foaming process to various materials and investigating the mechanical properties. Models based on classical nucleation theory were also developed (Martini, 1981; Martini et al., 1982; Colton, 1985; Colton and Suh, 1986; Colton and Suh, 1987abc; Colton, 1989). Recently, however, research at MIT's Microcellular Plastics Research Laboratory has focused on continuous extrusion processing. For a comprehensive review of microcellular plastics research and its associated process technologies, the reader is referred to Baldwin et al. (1994ab), Baldwin (1994), and Kumar (1991). Park was the first to demonstrate the feasibility of continuous microcellular processing by extruding microcellular filaments on the order of 0.010 inches in diameter using a nozzle as a rapid pressure-drop device (Park, 1993). Baldwin advanced the state of the art by addressing the cell growth phenomenon and producing thin microcellular films and tubes by implementing near-net shape nucleation (Baldwin, 1994). Despite having devised means to process microcellular polymers continuously, these extrusion systems suffer from instabilities. Since this thesis seeks to design an extrusion system to coat thin wires continuously with foamed polymer, system stability is essential. Therefore, the research will stabilize the foam extrusion process to enable processing of long lengths of wire.

### 2.2.2 Batch Processing

Microcellular plastics are produced using a three-step process. First, a single-phase gas/polymer solution is created by dissolving an inert gas such carbon dioxide or nitrogen into the polymer matrix under high pressure, the saturation pressure, for a given period of time called the saturation time. Equation (2-1) indicates that the equilibrium gas concentration in the polymer, $c_{eq}$, is a function of temperature and pressure.

$$dc_{eq} = dc_{eq}(p,T) = \left(\frac{\partial c_{eq}}{\partial p}\right)_T dp + \left(\frac{\partial c_{eq}}{\partial T}\right)_p dT \tag{2-1}$$

The weight of the polymer increases as gas is dissolved into the matrix. Weight gains ranging from 3% to 20% are typically needed for successful microcellular foaming. Once a sufficient amount of gas has diffused into the polymer matrix, the second step consists of nucleating billions of voids per cubic centimeter in the sample by using a thermodynamic instability in the form of a rapid pressure drop. This is easily understood by tracing the solubility change of the gas in the polymer during the course of the foaming procedure, as shown in Figure 2.3, a schematic representation of equation (2-1).

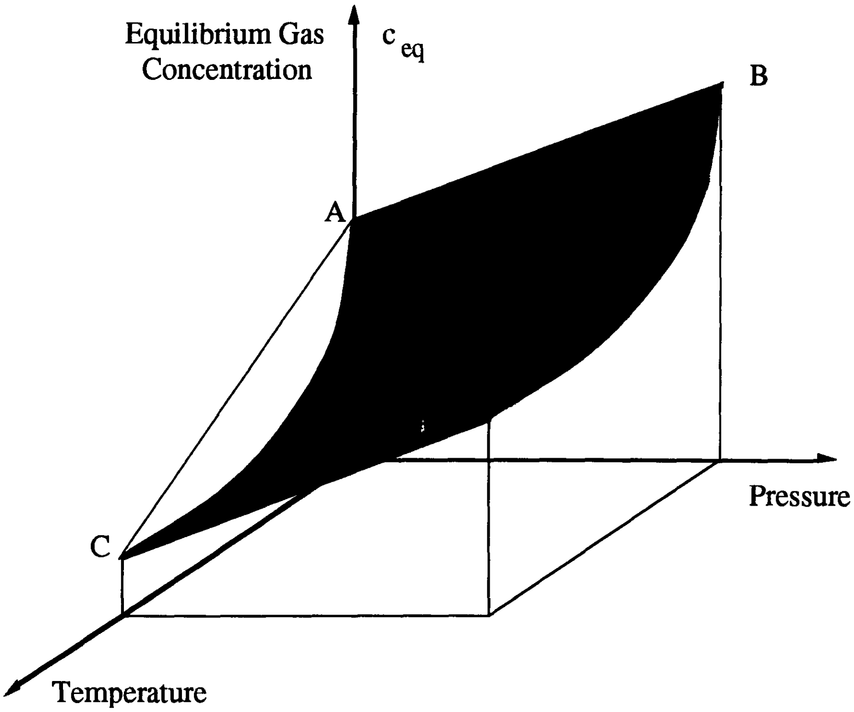

*Figure 2.3: Typical equilibrium gas concentration in polymers as a function of pressure and temperature.*

The figure indicates that gas saturation increases with pressure and decreases with temperature. Saturation increases with pressure because there is a larger driving force to dissolve the gas in the polymer. Saturation decreases with temperature because the kinetic energy acquired by every gas molecule increases the characteristic volume occupied by each molecule. Since the "volume" of each gas molecule increases, less gas molecules can fit between the polymer molecules, and, as a result, the equilibrium concentration diminishes.

The sample has an initial equilibrium gas concentration equal to $A$ as shown in Figure 2.3. During dissolution, the first step of microcellular processing, the gas concentration increases from $A$ to $B$. Billions of cells are then nucleated by quickly reducing the pressure of the chamber. This comprises the thermodynamic instability: Immediately after dropping the pressure, the equilibrium gas concentration returns to $A$. A finite time is necessary for the system's gas concentration to fall from $B$ to $A$. It is during this time that the gas comes out of solution and billions of microcells are formed. Nucleation is the process by which a single-phase solution separates into two discrete phases. Gas molecules cluster to form the voids. It is crucial to effect the thermodynamic state change as rapidly as possible. If the pressure were reduced gradually, for example, the gas in solution would preferentially diffuse to cells which have already nucleated rather than nucleating additional cells. This leads to nonuniform cell size distributions and excessively large cells. Hence, a rapid thermodynamic state change is necessary for evenly distributed, small-sized cells. The final stage of microcellular processing is cell growth in which cells are allowed to expand to their final size. This is often accomplished by increasing the temperature near the glass transition temperature of the polymer. The temperature increase serves not only to decrease the equilibrium gas concentration further to point $C$ in Figure 2.3, but also to decrease the flow strength of the polymer. The higher temperature increases the gas diffusivity and cells grow as they absorb more gas. This temperature is known as the foaming temperature and is used to control the rate of cell growth.

### 2.2.3 Continuous Processing

The following discussion is intended to provide a brief overview of microcellular extrusion. A detailed explanation of extrusion processing and its design considerations is presented in chapter 4. Extrusion of microcellular plastics embodies the same requirements as batch processing: gas dissolution, cell nucleation, and cell growth. The current prototype microcellular extrusion system is shown in Figure 2.4. Polymer pellets in the extruder hopper descend through the action of gravity into the feed section of the barrel where they are melted. Midway along the barrel, supercritical $CO_2$ is injected into the melt flow. Metering of the supercritical fluid is controlled by a porous metallic material. The large gas bubbles are entrained in the polymer flow and broken into smaller bubbles by the shearing action of the screw. It is critical to dissolve the $CO_2$ into the polymer melt as much possible to create a single-phase solution. With the aid of mixing sections on the screw as well as static mixers, a single-phase solution is created. This solution is subsequently sent through a nozzle to effect the rapid pressure drop. The result is nucleation of billions of microvoids per cubic centimeter.

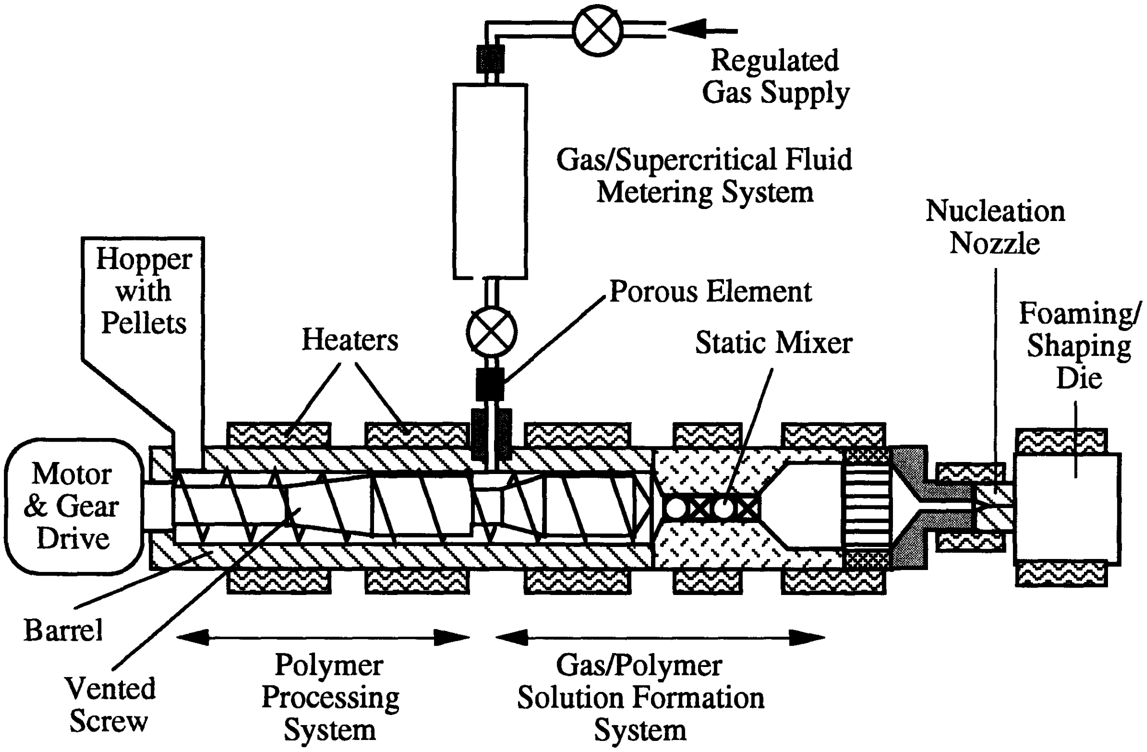

*Figure 2.4: Schematic of the prototype microcellular extrusion system.*[§]

---

[§] Adapted from Baldwin (1994).

# CHAPTER 3

# MICROCELLULAR PROCESSING CHARACTERIZATION OF FLUOROPOLYMERS

## 3.0 Introduction

Although this research is primarily concerned with continuous microcellular processing of polymers, it is crucial to have a good understanding of the discrete, or so-called batch microcellular foaming process. Since batch processing is considerably less complex than continuous processing, we typically seek to identify the foaming parameters at the batch level and then use these conditions as a starting point in the investigation of the continuous process. This chapter elaborates the results of the fluoropolymer batch processing investigation and details the different experimental procedures. It begins by providing a brief profile of the FEP and PFA fluoropolymers.

## 3.1 Fluoropolymer Materials

### 3.1.1 Fluorinated Ethylene Propylene (FEP)

FEP was first commercially produced in the early 1960's by DuPont (Rubin, 1990). The formal name for this fluoropolymer is poly(tetrafluoroethylene-*co*-hexafluoropropylene) and its basic building block is shown in Figure 3.1. FEP is a commonly used wire-coating material since it has superb electrical properties: low dielectric constant, high dielectric strength, and high resistance to arcing. These properties are stable over a wide range of temperatures and electrical frequencies. In addition, FEP cannot undergo photochemical reactions since it does not absorb electromagnetic radiation in the visible or ultraviolet range. This property gives FEP excellent weathering conditions, even under extremely harsh environments. In fact, samples have shown no detectable change after 20 years of outdoor exposure (Rubin, 1990).

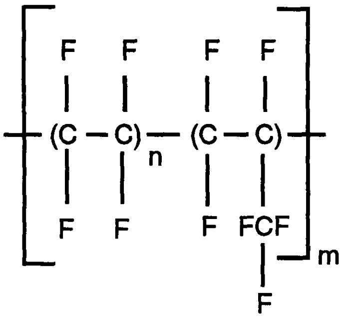

*Figure 3.1: FEP monomer unit.*

Applications for FEP include pipe linings in chemical processing equipment, roll covers, and a variety of wire/cable insulations. FEP film is used as glazing in solar energy cells (Juran, 1990). Although FEP is compatible with injection molding, extrusion, foam molding, and powder, fluidized bed coating, special care must be taken during processing. At the required elevated processing temperatures, the fluorine atoms in the polymer network become corrosive to many metals. Hence, FEP processing equipment is typically made from corrosion-resistant nickel-based alloys such as Hastelloy®, Inconel®, Monel®, or Xaloy®.† Corrosion occurs if the residence time of the polymer in the equipment is too long or if processing temperatures are too high. Resin degradation accelerates corrosion significantly (DuPont FEP 4100 Data Sheet). Aside from general processing concerns, fluoropolymer processing can present health hazards. At high temperatures, toxic fumes can be released from the polymer melt. Inhalation of these fumes has been known to cause "polymer fume fever" in humans. As a result, the Society of the Plastics Industry, Inc., has established fume hood designs for safe processing of fluoropolymers.*

The specific grade used in this research was DuPont FEP Teflon® 4100. It is designed for "super high-speed extrusion of thin coatings on small-gauge wires for twisted-pair constructions." Its high melt flow number of 20 is ideal for fast extrusion speeds. The resin has a melting temperature of 259°C, a dielectric constant of 2.02 at 1 MHz, and a tensile strength of 24 MPa (3,500 psi) (DuPont FEP 4100 Data Sheet). FEP has a nominal density of 2.15 g/cm$^3$ (Juran, 1990) and costs approximately $15 per pound.

---

† Hastelloy® is a registered trademark of Cabot Corporation; Inconel® and Monel® are registered trademarks of International Nickel Company, Inc.; Xaloy® is a registered trademark of Xaloy, Inc.

* Please refer to the *Guide to the Safe Handling of Fluoropolymer Resins* (1992, p.12) for detailed information regarding fume hood requirements.

### 3.1.2 Perfluoroalkoxy (PFA)

PFA is another commonly used wire-coating fluoropolymer. The basic structure for this polymer is shown in Figure 3.2. There are many similarities between FEP and PFA. Like FEP, PFA does not absorb electromagnetic radiation in the visible or ultraviolet range. Therefore, transparent films can be made. It also has excellent weathering resistance. The same processing techniques and safety considerations apply to PFA as well. In contrast, however, PFA has better mechanical properties than FEP at temperatures above 302°F and can be used up to 500°F.

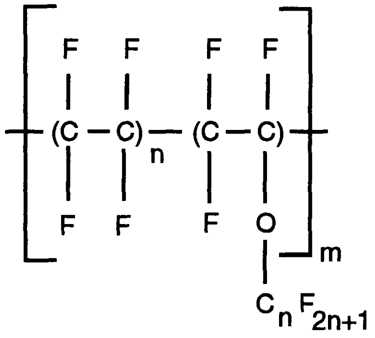

*Figure 3.2: PFA monomer unit.*

The specific grade used in this research was DuPont PFA Teflon® 440 HP. PFA 440 HP has a density of 2.12-2.17 g/cm$^3$, a melting temperature of 302-310°C, a tensile strength of 25 MPa (3,600 psi), and a dielectric constant of 2.03 at 1 MHz (DuPont PFA 440 HP Data Sheet). PFA is a comparatively expensive polymer valued at roughly $25 per pound.

## 3.2 Weight Gain Results

Before actual foaming experiments could be performed, the first step was to determine the mass uptake characteristics of FEP 4100 and PFA 440 HP. By determining the time at which the given polymer absorbs the greatest amount of $CO_2$, the optimum saturation time is revealed. $CO_2$ was used because of its higher solubility in polymers compared with $N_2$ (Durril and Griskey, 1966 and 1969; Van Krevelen, 1990). Samples of FEP and PFA were cut into squares measuring approximately 20 mm on each side and 1 mm in thickness. After the samples were weighed, they were placed in the pressure vessel shown in Figure 3.3 and pressurized to 850 psi. The samples remained at this saturation pressure for the predetermined saturation time, after which the chamber was discharged and the samples reweighed. The release time, the time between depressurization of the chamber and weighing of the samples, was approximately 3 minutes for FEP and 3:20 minutes for PFA. The entire experiment was performed at room temperature. Knowing the masses of the samples before and after pressurization, the weight gain or mass uptake percentage is readily calculated. Figures 3.4 and 3.5 present the weight gain graphs for FEP and PFA, respectively.

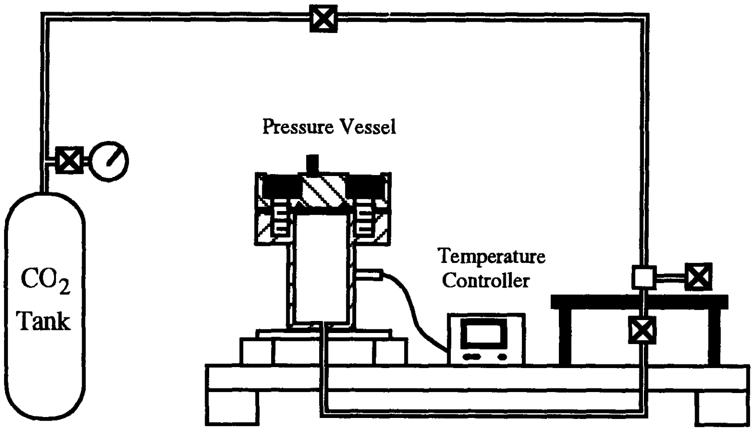

*Figure 3.3: Experimental setup for weight gain experiments.*

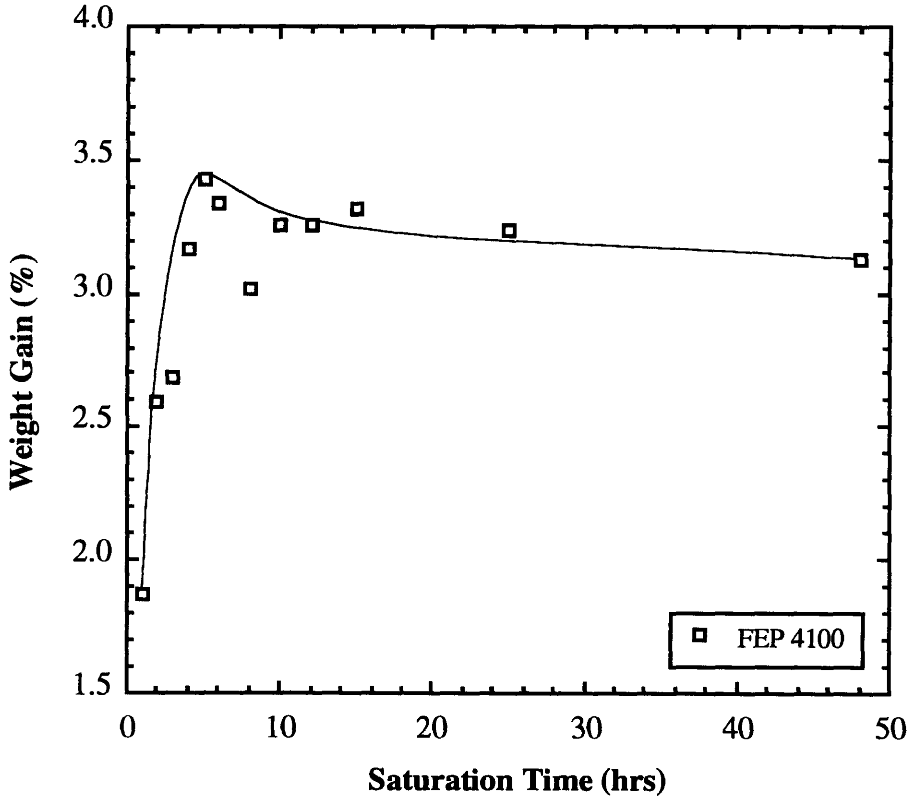

*Figure 3.4: FEP mass uptake of $CO_2$ at room temperature and 850 psi.*

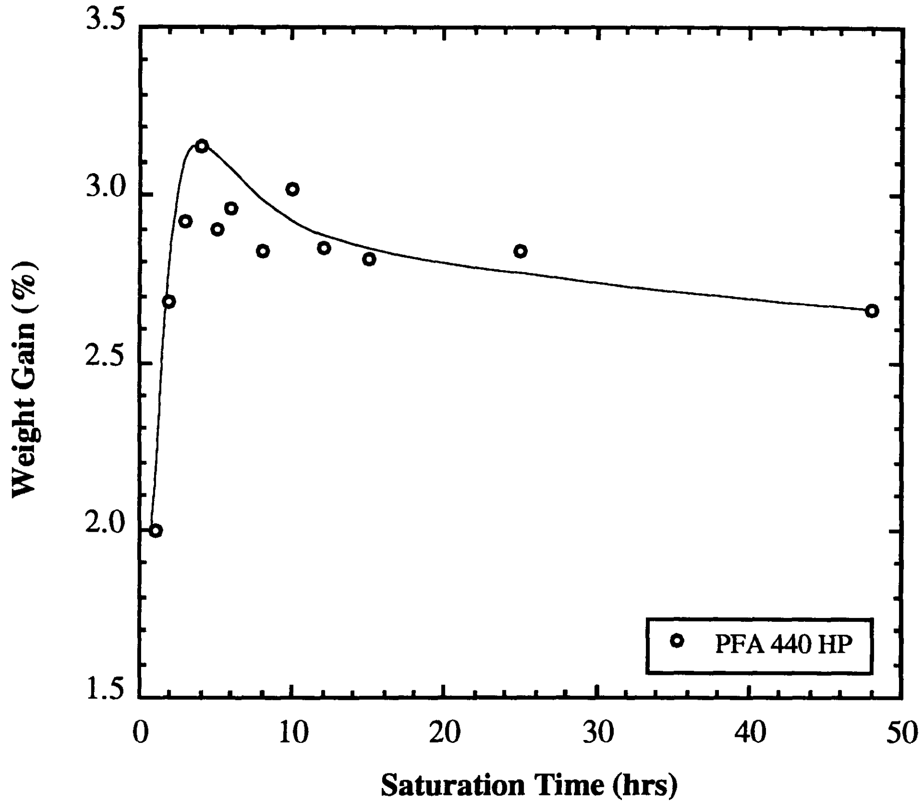

*Figure 3.5: PFA mass uptake of $CO_2$ at room temperature and 850 psi.*

As can be seen in both figures, the weight gain rises quickly to a maximum and then decreases to a steady-state value. The maximum weight gain for FEP was 3.43% after 5 hours of saturation while the maximum weight gain for PFA was 3.15% after 4 hours of saturation. These values should be used as the ideal saturation times for room temperature saturations. Although it seems intuitive that polymers should absorb gas at an exponential rate and reach a maximum at steady state, the presence of the global maximum before steady state in Figures 3.4 and 3.5 indicates that the polymer has changed its molecular orientation. Such behavior is attributed to induced crystallinity of the polymer as a result of gas sorption. Baldwin et al. (1992) discovered that the crystallinity of semicrystalline PET increased by as much as 23% when the polymer was saturated with $CO_2$ at 800 psi and 20°C (room temperature). Additional crystallinity is induced when the critical gas concentration is reached in the polymer. Crystallization occurs when the linear chain molecules fold back onto themselves. As gas is absorbed into the polymer matrix, the interatomic spacing between the molecule chains increases until a critical distance of separation is reached. Once this critical distance is reached, the molecules have more freedom to realign themselves into crystalline formations. As crystalline structures form in the polymer, the gas is forced into the remaining amorphous regions of the polymer. When the critical crystallinity level is reached, the gas has nowhere else to migrate and is expelled from the matrix. This accounts for the decrease in $CO_2$ sorption with time for both FEP and PFA.

The weight gain curves for FEP and PFA are plotted together in Figure 3.6. The relative magnitude of the humps in Figure 3.6 indicates that PFA's crystallinity increases more than FEP's. The plot also indicates that PFA accepts less gas into its matrix than FEP, suggesting that PFA is a more crystalline polymer than FEP to begin with since it is more reluctant to allow diffusion into its matrix.

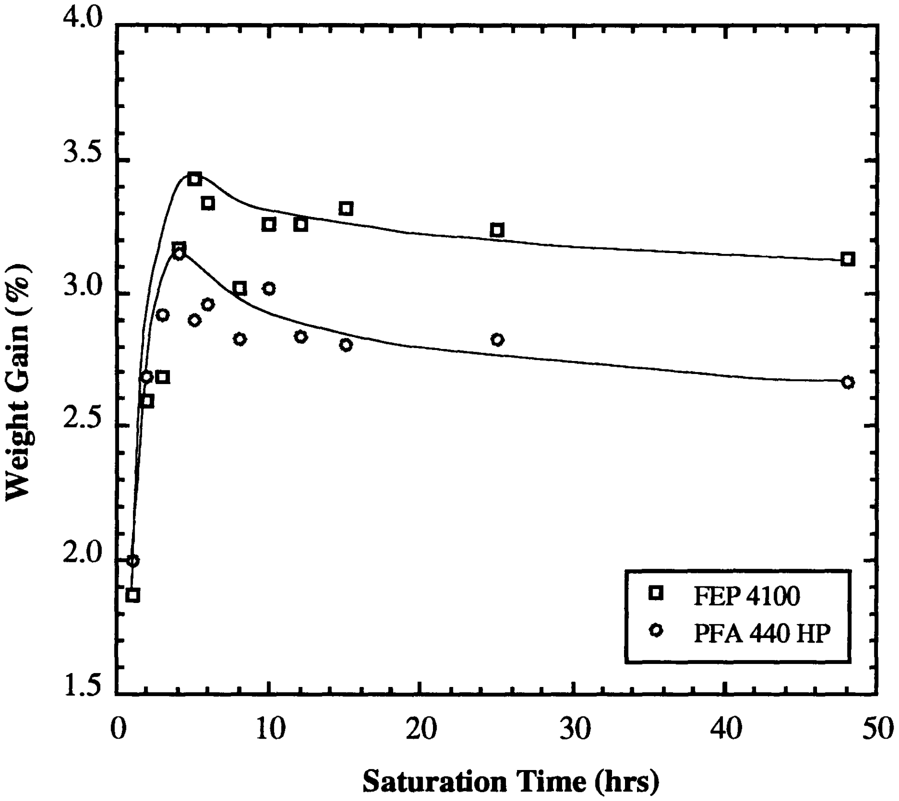

*Figure 3.6: Mass uptake comparison of FEP and PFA at room temperature and 850 psi. FEP characteristically accepted more gas into its polymer matrix than PFA.*

Weight gain characterization was also attempted at higher temperatures. In doing so, the exponential behavior of gas solubility in polymers with respect to temperature was confirmed, as seen in Figure 3.7. Gas solubility decreases with temperature. Measurements of mass uptake could not be made above 200°C for FEP and 250°C for PFA because the samples foamed in the pressure chamber during depressurization.

Nevertheless, to achieve the highest weight gain at room temperature, it was found that FEP should be saturated for 5 hours while PFA should be saturated for 4 hours. A larger weight gain provides a greater driving force for the nucleation of cells.

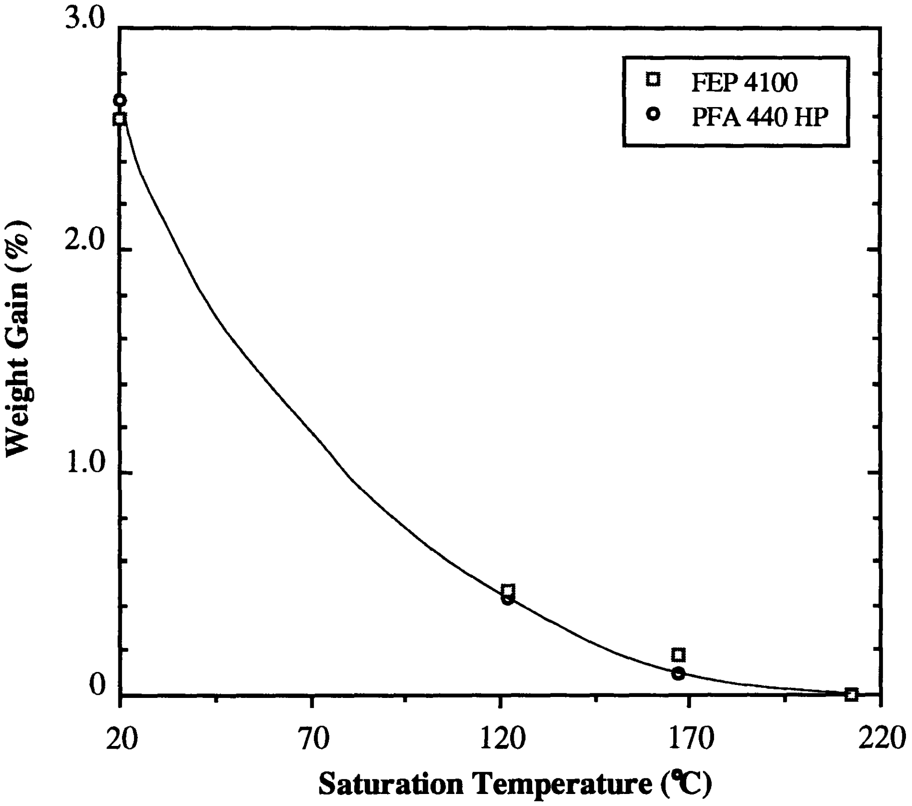

*Figure 3.7: FEP and PFA mass uptake as a function of temperature. The trend indicates that weight gain, and thus solubility, is an exponential function of saturation temperature.*

## 3.3 Batch Processing Results

After the weight gain experiments were completed, batch microcellular foaming experiments were performed. Batch processing of the fluoropolymers proceeded in two primary phases:

1) Gaseous Saturation
- Low Pressure, Room Temperature Saturation, Various Foaming Temperatures
- Moderate Pressure, High Temperature Saturation and Foaming (No Glycerin Bath)

2) Supercritical Saturation
- High Pressure, Low Temperature Saturation, Various Foaming Temperatures
- High Pressure, High Temperature Saturation and Foaming (No Glycerin Bath)

After foaming, the samples were prepared for viewing in a scanning electron microscope (SEM) since cell sizes on the micron level are invisible to the naked eye. Preparation included embrittling the samples by immersing them in a liquid nitrogen bath for half a minute. The samples were immediately removed from the bath using needle-nosed pliers and then struck with a plastic hammer, producing a clean fracture surface. The fractured samples were carefully epoxied to metal stubs compatible with the SEM sample tray. Coating the sample surfaces with a fine layer of gold and a thin stripe of colloidal graphite paint (Energy Beam Sciences #P-CG-45) comprised the final step.

The samples were typically scanned with a 10kV electron beam in a Cambridge Instruments SEM (Model #5431). A quick pass at low magnification revealed any nonuniformities in cell size distribution and provided a good view of any distortions in the sample's shape. Three photos were usually taken for each sample: The first to provide an overall view of the surface, the second at higher magnification to enable determination of the average cell density, and a third at even higher magnification to enable determination of the average cell size. The magnifications ranged from 20x to 1600x.

### 3.3.1 Gaseous Saturation

Low Pressure, Room Temperature Saturation, Various Foaming Temperatures

The fluoropolymer samples (20 mm squares, 1 mm thick) were saturated at 800-850 psi and room temperature for a specified period of time using the apparatus in Figure 3.3. After depressurization, the samples were immersed in a hot glycerin bath to instigate foaming. The foaming temperature (glycerin temperature) was varied from room temperature to the melt temperatures of the polymers. Table 3.1 lists the conditions for several experiments performed using the aforementioned method.

*Table 3.1: Saturation and foaming conditions for low pressure, room temperature $CO_2$ saturation.*

| *Material* | *Saturation time [hours]* | *Saturation pressure [psi]* | *Release time [minutes]* | *Foaming time [sec]* | *Foaming temperature [°C]* |
|---|---|---|---|---|---|
| FEP | 1 | 850 | 2:45 | 25 | 154 |
| PFA | 1 | 850 | 3:30 | 30 | 165 |
| FEP | 2 | 800 | 6:40 | 25 | 150 |
| PFA | 2 | 800 | 5:50 | 30 | 150 |
| FEP | 3 | 850 | 2:40 | 30 | 168 |
| PFA | 3 | 850 | 3:20 | 30 | 165 |
| FEP | 4 | 800 | 3:34 | 30 | 165 |
| PFA | 4 | 800 | 4:14 | 35 | 165 |
| FEP | 5 | 800 | 2:40 | 20 | 162 |
| PFA | 5 | 800 | 3:30 | 30 | 162 |
| FEP | 6 | 800 | 3:15 | 30 | 165 |
| PFA | 6 | 800 | 4:00 | 30 | 165 |
| FEP | 8 | 800 | 2:35 | 30 | 166 |
| PFA | 8 | 800 | 3:15 | 30 | 166 |

This series of experiments did not produce a microcellular structure since insufficient nucleation had taken place. Any nucleation that occurred took place near the surface of the sample, as seen in Figure 3.8a. Both FEP and PFA became opaque after they were immersed in the glycerin bath. FEP became completely white and had large, uniform, spherical surface bumps and cells. These surface cells were evenly spread out across the sample. The higher the weight gain of the sample before oil bath immersion, the smaller the size of the surface cells and the greater the number. The internal structure of FEP is shown in Figure 3.8b. The scaly appearance of the fracture surface suggests the presence of rudimentary cells. These cells are neither fully developed nor microcellular. PFA was much less active when immersed in the bath. The samples became milky white in some regions and remained translucent in others. This result was expected since the weight gain study revealed that PFA permits less diffusion of $CO_2$ into its matrix. Since PFA absorbed less gas, fewer cells were nucleated. Very few irregularly shaped surface cells were created although clustering of such large cells occasionally took place. Bubble size and density, again, was a function of saturation time. Like FEP, the fracture surface of PFA had a scale-like appearance with undeveloped cells, as shown in Figure 3.9.

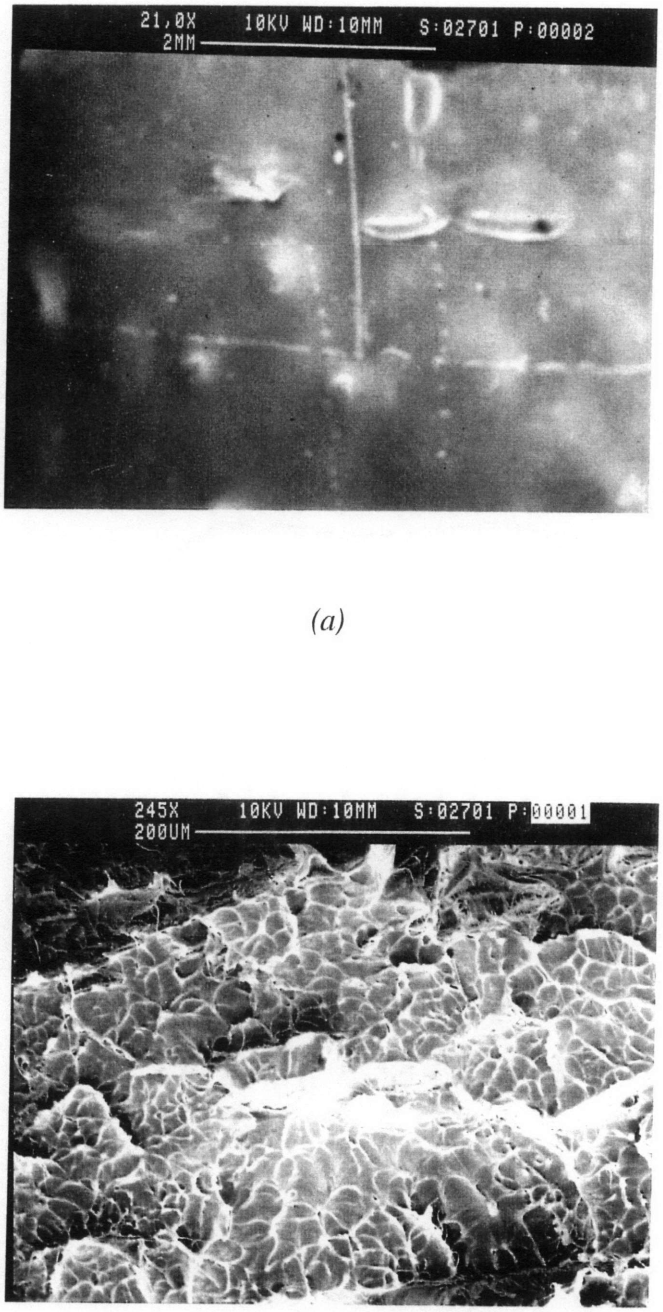

(a)

(b)

*Figure 3.8: Structure of the FEP outer surface a) and fracture plane b) saturated for 3 hours with room temperature $CO_2$ at 850 psi and foamed at 168°C.*

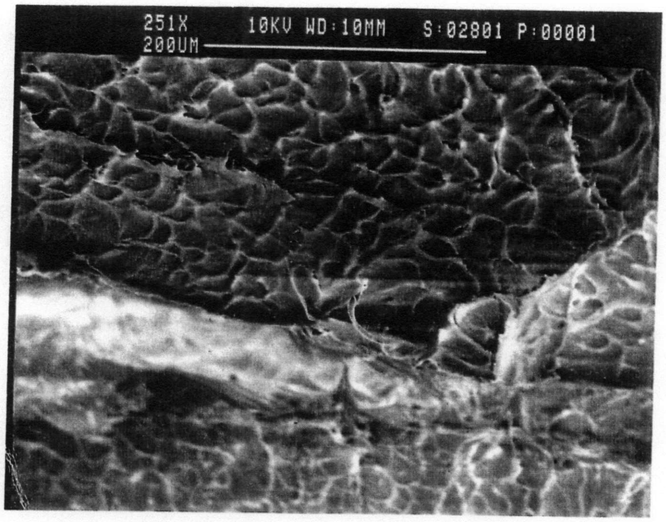

*Figure 3.9: Fracture surface of PFA saturated for 3 hours with room temperature $CO_2$ at 850 psi and foamed at 165°C. (Since the sample surface in this saturation contained one bubble which was not resolved by the SEM, a micrograph of the PFA surface was not included.)*

It is clear from this section that higher weight gains are needed to increase the number of nucleation sites. To increase the weight gain, the saturation pressure and temperature were increased, as explained in the next section.

### <u>Moderate Pressure, High Temperature Saturation and Foaming (No Glycerin Bath)</u>

Colton demonstrated that semicrystalline polypropylene (with additives) and ethylene-propylene copolymers could be microcellular batch processed if the polymers were saturated above their respective melt temperatures (Colton, 1988). Colton saturated 2 inch diameter disks (1/16 inch thick) with nitrogen gas for 30 minutes before depressurization. Typical cell densities ranged from $10^9$-$10^{10}$ cells/$cm^3$. This procedure was based on the proposition that semicrystalline polymers lose their crystallinity upon melting. Polymer chains are tightly packed in the crystalline regions, leaving very little room for gas sorption. By destroying the crystallinity, much more gas can be absorbed. Although gas solubility in a polymer decreases with temperature, the crystallinity effect is the dominating factor. Reducing crystallinity will offset the decrease in solubility with temperature.

Since the fluoropolymers in this study were saturated in a constant volume chamber, the elevated saturation temperatures also served to raise the saturation pressure. This also provides for higher weight gains. Figure 3.10 shows the results of saturating FEP and PFA at their melt temperatures with $CO_2$ for 9 hours. The corresponding saturation pressures were 1,570 psi and 1,670 psi, respectively. The sample size was the same as in the previous section. Both polymers foamed inside the chamber. This experiment provided the first encouraging result: Both samples had a uniform distribution of spherical bubbles throughout the thickness, not just the surface. The bubbles were large enough so that the sample became opaque. This was the first experiment where it was meaningful to calculate the average cell size and density for the samples. The average cell size for FEP was 0.44 mm while the cell density was only $1.6\times10^4$ cells/cm$^3$. In comparison, PFA had an average cell size of 0.84 mm and a cell density of $1.5\times10^3$ cells/cm$^3$. Both FEP and PFA experienced a slight volume change. While neither material attained a microcellular structure, the findings indicate that microcellular foaming may be possible provided higher weight gains are achieved.

FEP was also saturated for 36 hours under the same temperature and pressure conditions, but the results were similar to the 9 hour saturation with large cells and a low cell density. In order to compare with Colton's saturation above melt temperature, FEP was saturated approximately 30°C higher than its melt temperature. At this temperature, of course, the square sample lost its shape and settled into a small pool at the bottom of the chamber. The sample was destroyed in the process of removing it from the chamber. For this reason, saturation above the melt temperature was discontinued. At this point in the batch processing investigation, the main objective was still to achieve a higher mass uptake of $CO_2$ in the polymer.

### 3.3.2 Supercritical Fluid Saturation

The use of supercritical fluids have significantly advanced microcellular processing technology. A supercritical fluid is a fluid that is above both its critical temperature and critical pressure. Cha (1994) demonstrated that after saturating polymer samples under the high pressures afforded by supercritical $CO_2$ and then instigating the usual thermodynamic instability, the resulting foam can achieve submicron cell sizes and very large cell densities. These foams are termed *supermicrocellular* foams, characterized by cell sizes ranging from 0.1 to 1 μm and cell densities on the order of $10^{12}$-$10^{15}$ cells/cm$^3$. This morphology has led to density reductions as high as 90%. In addition to increasing the cell density, the use

*(a)*

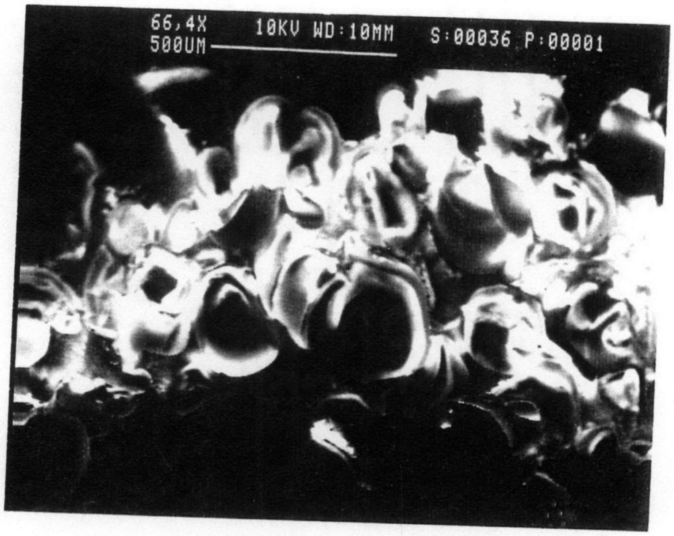

*(b)*

*Figure 3.10: Structure of FEP (a) and PFA (b) saturated for 9 hours with $CO_2$ at 270°C for FEP and 305°C for PFA.*

of supercritical fluids also reduces the saturation time. The idea for ultramicrocellular plastics has been proposed and is currently under development. Ultramicrocellular plastics are characterized by cell sizes on the order of 0.01 to 0.1 μm and cell densities ranging from $10^{15}$-$10^{18}$ cells/cm$^3$. Since these cell sizes are smaller than the wavelength of visible light, the potential for a transparent foam exists: A large percentage of the light should pass through the foam provided the cell density is not too large.

Supercritical $CO_2$ was used in the following phase of experimentation. $CO_2$ has a critical temperature of 31°C (88°F) and 7.38 MPa (1071 psi) (Vukalovich and Altunin, 1968). Figure 3.11 traces the states of the $CO_2$ during the foaming procedure.

High Pressure, Low Temperature Saturation, Various Foaming Temperatures

Carbon dioxide is commercially available at a maximum pressure of 850 psi. In order to saturate the Teflon samples at pressures much higher than 850 psi, it is first necessary to take the gas to its supercritical region. The experimental setup is shown schematically in Figure 3.12. The samples were loaded in small pressure chamber and the system was then pressurized to 850 psi. Next, the chamber was surrounded by an ice bath. As the $CO_2$ in the vessel condensed, the liquid flowed to the bottom of the chamber and the pressure in the chamber momentarily fell below 850 psi. At that instant, more $CO_2$ gas immediately entered the chamber because the gas cylinder was left open at 850 psi. The process of liquefaction continued until the entire chamber was filled with liquid $CO_2$. Half an hour was allotted for this phase of the experimental setup. After the chamber had filled with liquid $CO_2$ at 0°C, the pressure chamber was isolated from the gas cylinder and the ice bath was removed. To force the $CO_2$ into its supercritical region, the oven temperature was increased from room temperature to above 31°C, the critical temperature of $CO_2$. The initial set of experiments conducted in the supercritical regime was carried out at saturation temperatures ranging from 44°C to 148°C as shown in Table 3.2. Since the size of the pressure chamber was small for safety reasons, the sample sizes were much smaller than before, approximately 20 mm × 7 mm × 1.5 mm. The samples which did not foam in the chamber were then immersed in a glycerin bath at various temperatures. None of these trials yielded a microcellular structure. In fact, the samples resembled those attained in the room temperature saturation of section 3.3.1, marked by bumpy surfaces and large surface cells. The cell diameters, however, were visibly smaller and the cell densities larger than those of Figure 3.8a. Both polymers became opaque after the glycerin bath immersion. The internal structure of the samples was similar to those in Figures 3.8b and 3.9. There

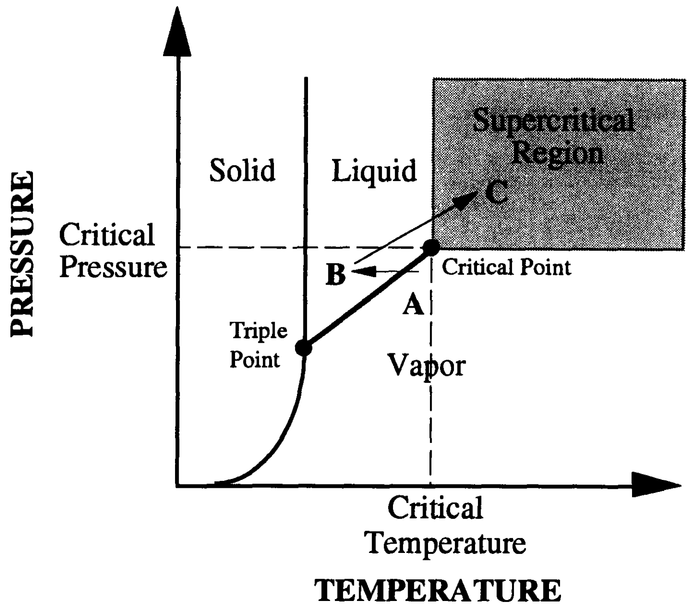

*Figure 3.11: Physical states of $CO_2$ during supercritical fluid procedure.*

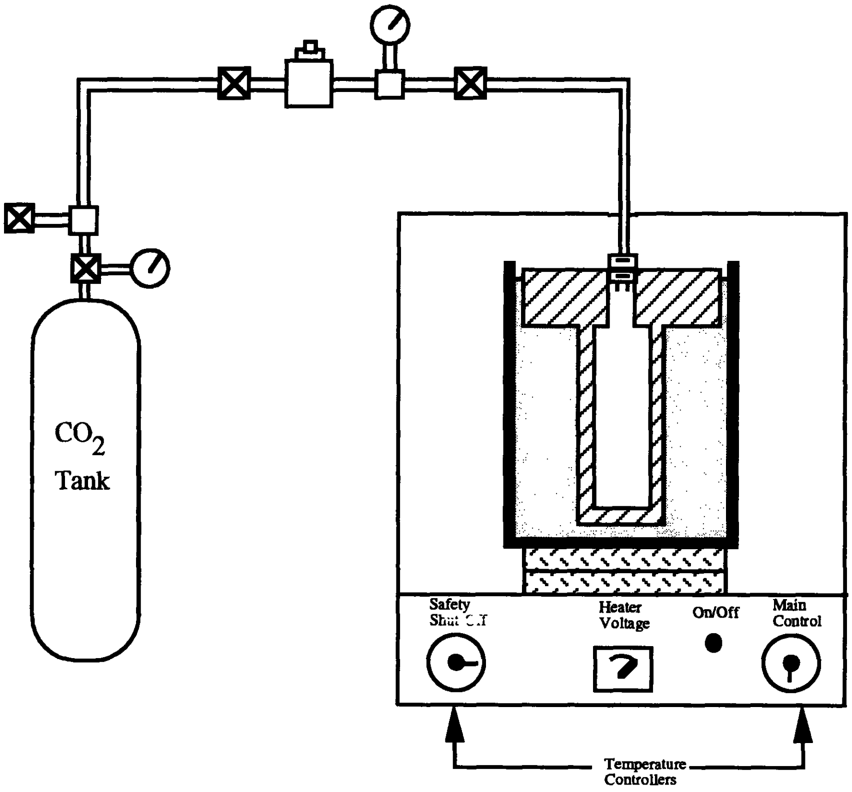

*Figure 3.12: Supercritical high pressure saturation apparatus.*

*Table 3.2: Saturation and foaming conditions for high pressure $CO_2$ saturation.*

| *Material* | *Saturation time [hrs]* | *Saturation pressure [psi]* | *Saturation temp. [°C]* | *Release time [min.]* | *Foaming time [sec]* | *Foaming temp. [°C]* |
|---|---|---|---|---|---|---|
| FEP | 24 | 4,500 | 55 | not recorded | 10 | 160 |
| FEP | 24 | 4,500 | 55 | not recorded | 10 | 190 |
| FEP | 4 | 4,400 | 67 | 3:40 | 2 | 166 |
| FEP | 5.5 | 4,000 | 82 | 2:29 | 5 | 145 |
| FEP | 4.5 | 4,400 | 148 | 2:00 | foamed in chamber | 148 |
| FEP | 5.5 | 3,900 | 60 | 2:30 | 5 | 145 |
| FEP | 2 | 3,500 | 44 | 2:00 | 2 | 164 |
| FEP | 2 | 6,000 | 125 | not recorded | foamed in chamber | 125 |
| PFA | 24 | 4,500 | 55 | not recorded | 10 | 160 |
| PFA | 24 | 4,500 | 55 | not recorded | 10 | 190 |
| PFA | 4 | 4,400 | 67 | 3:50 | 2 | 166 |
| PFA | 5.5 | 4,000 | 82 | 2:48 | 5 | 145 |
| PFA | 4.5 | 4,400 | 148 | 2:15 | foamed in chamber | 148 |
| PFA | 5.5 | 3,900 | 60 | 2:50 | 5 | 145 |
| PFA | 2 | 3,500 | 44 | 2:00 | 5 | 164 |

was often cleavage of the samples' cross section into several layers as shown in Figure 3.13.

The major conclusion drawn from these series of tests is that insufficient gas sorption is the primary obstacle to the creation of a microcellular structure, as noted by the large surface cells. Simply utilizing the high pressures afforded by supercritical $CO_2$ alone is inadequate to diffuse large amounts of gas into the polymer matrix. The saturation temperatures in this section were well below the polymers' melt temperatures; as a result, crystallinity of the matrix prevented additional gas diffusion.

The most promising result thus far took place at a very high saturation temperature (the melt temperature), as discussed in section 3.3.1. The cells, although too large, were uniformly distributed throughout the cross section of the sample. The last remaining experimental condition was to saturate at both high pressure and high temperature using supercritical $CO_2$. Such temperatures will destroy the crystalline regions in the polymer matrix while the high pressures will force even greater amounts of $CO_2$ into the polymer.

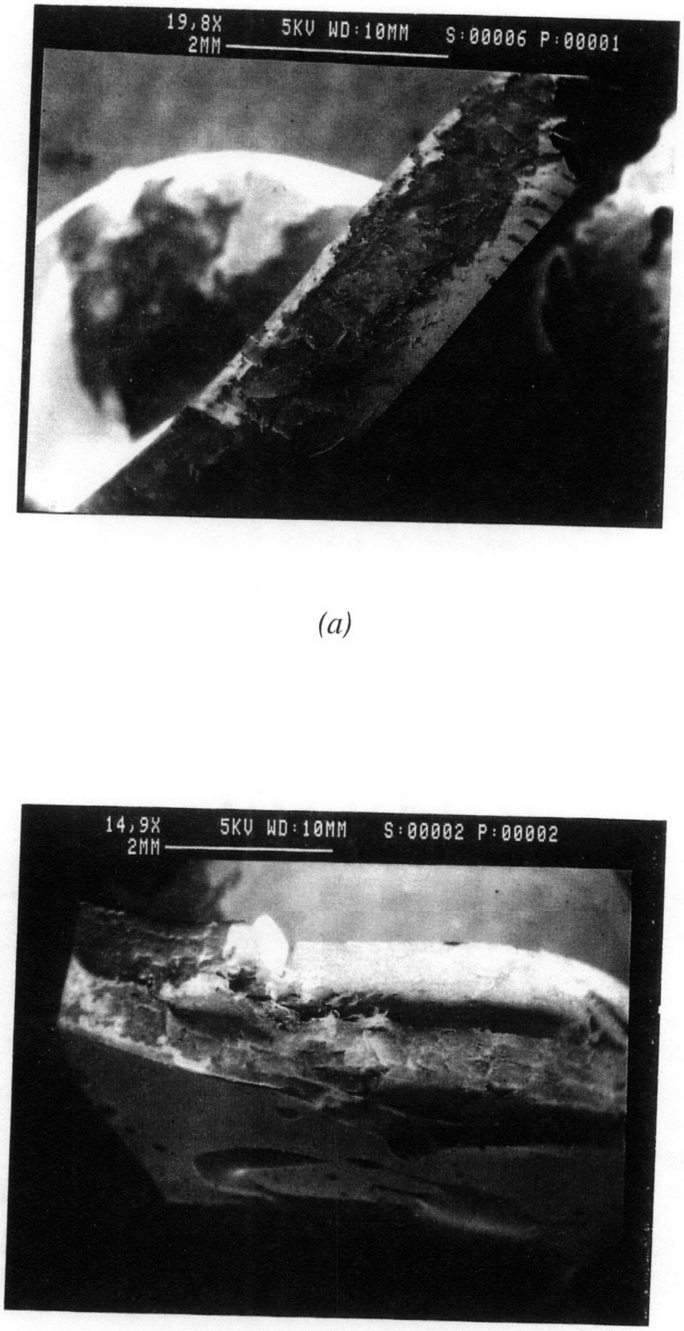

(a)

(b)

*Figure 3.13: Internal structure of FEP (a) and PFA (b) saturated for 2 hours with $CO_2$ at 6,000 psi and 125°C.*

High Pressure, High Temperature Saturation and Foaming (No Glycerin Bath)

Microcellular foams were achieved using both high pressure supercritical $CO_2$ and high temperature saturations. Table 3.3 shows the different temperature/pressure/time conditions tested for FEP. (PFA was tested for many of these conditions but the temperatures were not high enough for sufficient gas saturation. The results for PFA are discussed later.) All these samples foamed after chamber depressurization and, as a result, the glycerin bath was not needed to instigate cell nucleation.

*Table 3.3: High pressure, high temperature FEP saturation conditions.*

| *Saturation Temperature [°C]* | *Saturation Pressure [psi]* | *Saturation Time [hrs]* |
|---|---|---|
| 221 | 5,000 | 2 |
| 223 | 5,000 | 2 |
| 224 | 5,500 | 2 |
| 225 | 5,500 | 4 |
| 230 | 5,000 | 4 |
| 230 | 5,500 | 4 |
| 235 | 5,500 | 4 |
| 237 | 5,000 | 2 |
| 237 | 5,500 | 2 |
| 240 | 5,500 | 4 |
| 245 | 5,500 | 2 |
| 245 | 5,500 | 4 |
| 250 | 3,000 | 2 |
| 250 | 4,000 | 2 |
| 250 | 4,500 | 2 |
| 250 | 5,000 | 2 |
| 250 | 5,500 | 4 |
| 225-250 | 5,000-5,500 | 2 |

None of the samples processed at 221°C, 223°C, and 224°C achieved a microcellular structure. Although the samples became opaque after processing, a cellular structure was not discernible and, in fact, the sample surfaces were marked by bulges and large bumps while the cross section split into several layers, as shown in Figure 3.14.

The best microcellular foam was attained after saturating the FEP sample at 225°C at 5,500 psi for 4 hrs, as shown in Figure 3.15. These experimental conditions led to an average cell size of 6.1 μm with a cell density of $8.5 \times 10^9$ cells/$cm^3$. The sample was opaque and had a very smooth surface finish. The volume of the sample expanded by a

*Figure 3.14: Separation of the cross section of the FEP sample saturated at 221°C for 2 hours.*

factor of 2.4 and remained planar. The cell size was uniform throughout the entire sample, including the edges, as noted while scanning the sample surface with an SEM. These are all ideal characteristics of a microcellular foamed polymer. This is the first known reported case of microcellular foamed FEP.

The samples processed at 230°C also exhibited a microcellular structure. As expected, the sample saturated at 5,500 psi had a larger cell density and a smaller cell size than the sample processed at 5,000 psi. At 5,500 psi, the cell size was 9.6 μm and the cell density was $3.8\times10^9$ cells/cm$^3$ while at 5,000 psi, the cell size was 10.8 μm and the cell density was $1.1\times10^9$ cells/cm$^3$.

At saturation temperatures of 240°C and higher, an interesting phenomenon was observed: Samples had an approximate microcellular structure but were riddled with occasional large voids 200-300 μm in diameter, as shown in Figure 3.16. These samples had cell densities greater than $10^9$ cells/cm$^3$, but the typical cell size was slightly larger than 10 μm. The samples also became distorted and twisted as a result of tremendous 350% volume expansions. Figure 3.17 presents the fracture surface for the sample saturated at 4,000 psi and 250°C for 2 hours. The sample curved into a distinctive U shape. It is interesting to note that the cells are larger in the middle of the sample than at the edges. The average cell size was 123 μm.

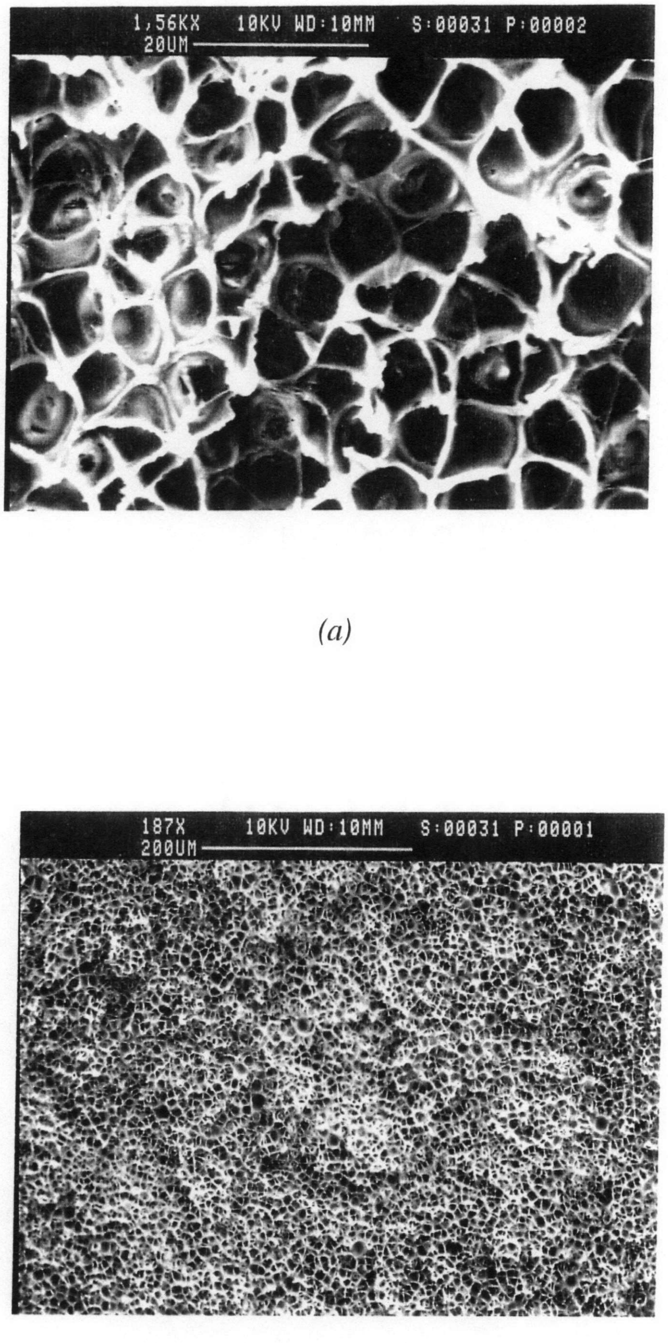

*(a)*

*(b)*

*Figure 3.15: Fracture surface of FEP microcellular foam produced at 225°C and 5,500 psi. The average cell size is under 10 μm a) with uniformity in both cell size and distribution b).*

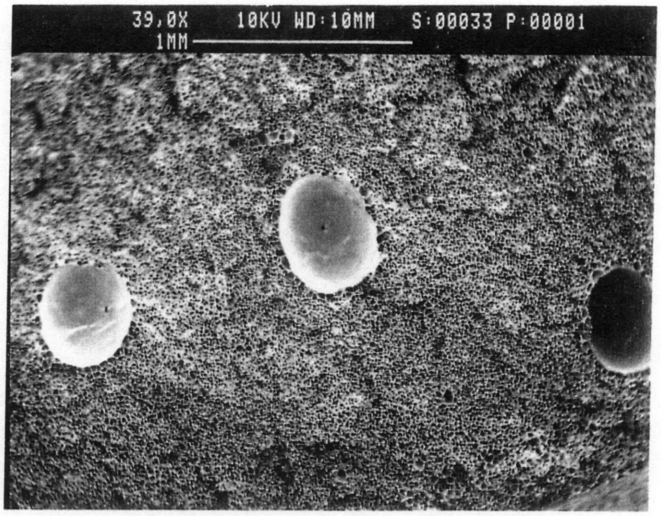

*Figure 3.16: Intermittent large cells amidst uniformly distributed smaller cells on the fracture surface of the 240°C sample .*

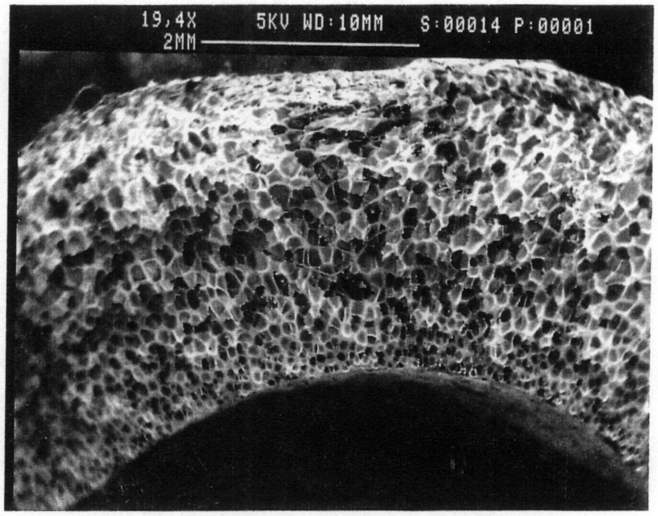

*Figure 3.17: Curvature induced by foaming.*

The primary deviation from Colton's results is that a microcellular structure was produced below the melt temperature of the material. In addition, the cell morphology of the FEP samples did not improve as the saturating temperature was increased above 225°C. From the standpoint of the both cell morphology and sample expansion, 225°C is the optimum saturation temperature. Since cells larger than 10 μm appeared at temperatures above 235°C, FEP has a small batch processing window of 10°C.

FEP coated wires were also batch processed to determine the feasibility of replacing tape winding with semicontinuous foaming: By extruding an FEP wall around the wire and then foaming an entire spool of wire, the resulting time and material savings may justify batch processing. Table 3.4 presents the various experiments performed with 10 mil diameter wire samples which were 3 inches long and had a 27 mil FEP wall. As shown in Figure 3.18, the cells are uniformly distributed around the wire. The samples became opaque after foaming and a constant outer diameter after expansion was maintained. The only exception occurred at 250°C where the outer diameter of the foamed coating was highly nonuniform. The coating at the ends of the wire curled inwards leaving the wire exposed. For the experiments listed in Table 3.4, it was surprising to note that on average, the cell sizes for the wire sample were larger than those of the rectangular sample by 77%. Figure 3.19 displays the cell structure for a rectangle and wire sample for comparison. It appears that the presence of the wire has an effect on cell morphology. Further testing is necessary to confirm this hypothesis. In any case, very long lengths of wire should be microcellular processed to determine the feasibility of replacing tape winding with batch processing of a wire spool.

*Table 3.4: Comparison of cell morphologies for different sample geometries.*

| *Sample Geometry* | *Experiment Number* | *Cell Size [μm]* | *Cell Density x $10^9$[cells/cm$^3$]* |
|---|---|---|---|
| rectangle | 21 | 19.4 | 0.33 |
| wire | 21 | 32.4 | 0.072 |
| rectangle | 22 | 11.5 | 3.3 |
| wire | 22 | 17.0 | 0.94 |
| rectangle | 29 | 10.8 | 1.1 |
| wire | 29 | 13.5 | 0.61 |
| rectangle | 30 | 9.6 | 3.8 |
| wire | 30 | 15.3 | 1.3 |
| rectangle | 32 | 8.7 | 5.5 |
| wire | 32 | 19.2 | 1.2 |
| rectangle | 33 | 13.9 | 2.3 |
| wire | 33 | 36.6 | 0.18 |
| rectangle | 35 | 13.3 | 4.7 |
| wire | 35 | 20.9 | 0.32 |

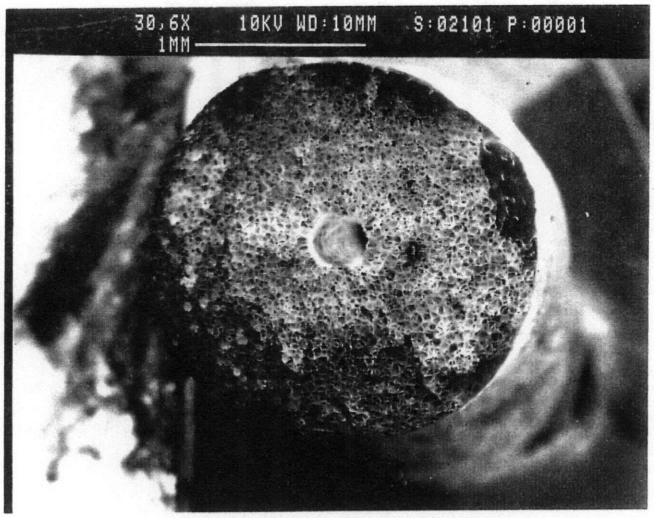

*Figure 3.18: Micrograph of a wire sample saturated at 237°C and 5,500 psi for 2 hours.*

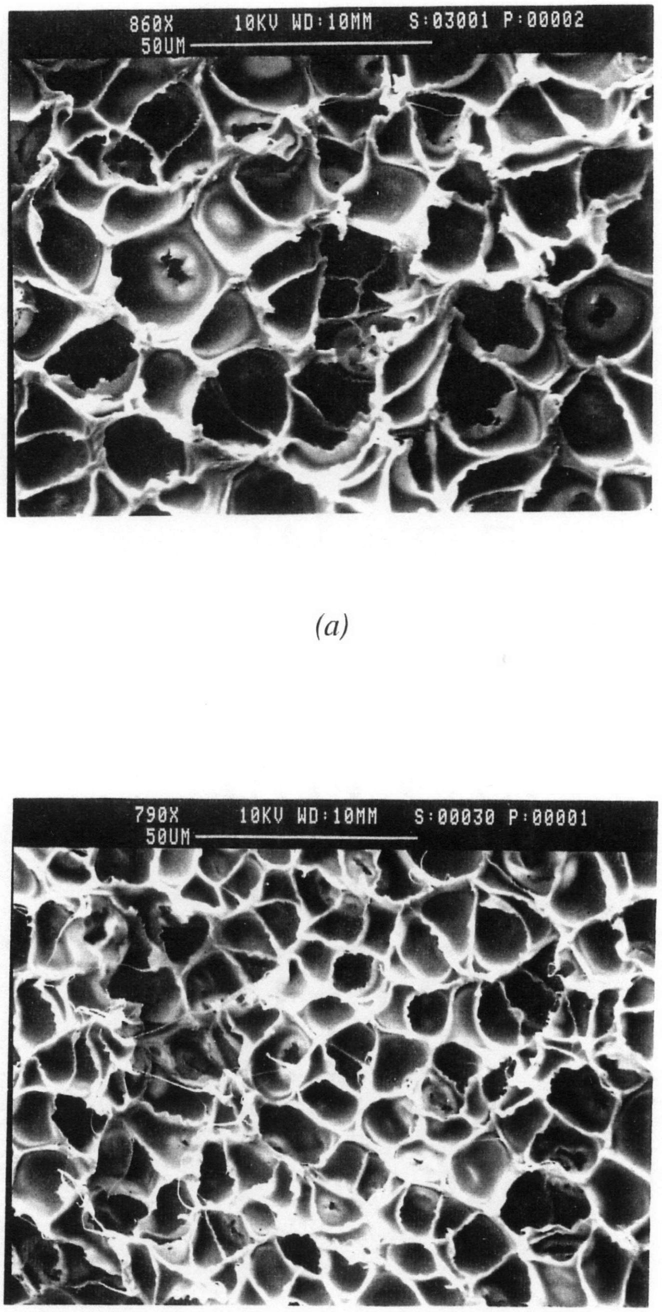

*(a)*

*(b)*

*Figure 3.19: Fracture surfaces of the rectangular sample (a) and the coated wire sample (b) produced in batch 30. The cells in the wire sample are 50% larger than those in the square sample.*

A final set of FEP batch processing experiments were performed with 10 mil wires having a 10 mil FEP wall thickness. The wires were processed at the conditions listed in Table 3.5 and then sent to Precision Interconnect for electrical analyses to determine the effects of foaming on the electrical performance of the wire. The samples were subsequently shielded with braided 42 AWG silver-plated copper wire (6 strands per carrier and 29.1 picks/inch on a 12 carrier braid). An unfoamed virgin sample was also analyzed and served as the reference point. The preliminary results presented in Table 3.5 are very encouraging. In every instance, the foamed wire samples exhibited lower dielectric constants than the virgin sample. As a result, other electrical properties such as time delay and capacitance improved. The most promising sample[†] had a measured dielectric constant of 1.37, 31% lower than the virgin sample. This decrease led to an 85.6% propagation velocity (expressed as a percentage of the speed of light). The propagation velocity is directly related to the data transmission speed that can be achieved with the wire. (Further insight into the theoretical aspects of dielectric constants and electrical performance is provided in chapter 5.) The results obtained with the foamed coated-wire samples experimentally verify the foundation of this thesis and reveal the potential of microcellular processing: Foaming a polymer reduces its dielectric constant and improves electrical performance.

All of the experiments performed thus far did not produce promising results for PFA since the material has a melting point roughly 35°C greater than that of FEP. The best foam was produced after saturating a sample at 288°C and 3,500 psi for 4 hours. The sample became opaque white after foaming and had a spongy feel given its 350% volume increase. For this reason, the sample was difficult to fracture and the micrographs shown in Figures 3.20 and 3.21 appear distorted. The corresponding morphology had a 30.4 μm cell size and a $1.0\times10^9$ cells/cm$^3$ cell density. Although higher saturation pressures were not tested because of the safety limitations associated with the pressure vessel and the fittings, the experimental results suggest that a microcellular structure is attainable with higher saturation pressures.

---

[†] Although sample G had the lowest measured dielectric constant of 1.31, the foamed coating on this sample, as well as samples F and L, had an irregular outer diameter and therefore introduced variation in the dielectric measurement.

*Table 3.5: Experimental results of the batch processed FEP coated wire.*

| *Sample* | *Saturation Temp. [C]* | *Saturation Pressure [psi]* | *Saturation Time [hrs]* | *Length [in]* | *Capacitance [pF/ft]* | *Impedance [Ω]* | *Time Delay [ns/ft]* | *Propagation Velocity [%]* | *Dielectric Constant* |
|---|---|---|---|---|---|---|---|---|---|
| Unfoamed | Not Applicable | Not Applicable | Not Applicable | 14.0 | 29.4 | 53.39 | 1.431 | 71.0 | 1.983 |
| A | 225 | 5,500 | 4 | 9.5 | 17.6 | 69.322 | 1.211 | 83.9 | 1.42 |
| B | 235 | 5,500 | 4 | 13.0 | 15.5 | 79.075 | 1.188 | 85.5 | 1.37 |
| C | 230 | 5,500 | 4 | 9.5 | 15.9 | 76.346 | 1.187 | 85.6 | 1.37 |
| D | 230 | 5,000 | 4 | 13.0 | 16.8 | 75.859 | 1.205 | 84.3 | 1.41 |
| E | 235 | 5,500 | 4 | 13.0 | 15.1 | 79.616 | 1.178 | 86.3 | 1.34 |
| F | 240 | 5,000-5,500 | 4 | 13.0 | 17.3 | 73.527 | 1.188 | 85.5 | 1.37 |
| G | 237 | 5,500 | 2 | 13.0 | 14.9 | 82.493 | 1.164 | 87.3 | 1.31 |
| H | 221 | 5,000 | 2 | 13.0 | 24.7 | 59.247 | 1.349 | 75.3 | 1.76 |
| I | 224 | 5,500 | 2 | 13.0 | 17.9 | 70.124 | 1.225 | 82.9 | 1.45 |
| J | 223 | 5,000 | 2 | 13.0 | 21.2 | 64.345 | 1.29 | 78.8 | 1.61 |
| K | 230 | 5,500 | 4 | 13.0 | 16.6 | 73.089 | 1.202 | 84.5 | 1.4 |
| L | 240 | 5,500 | 4 | 13.0 | 18.3 | 69.711 | 1.203 | 84.5 | 1.4 |
| M | 225 | 5,500 | 4 | 14.0 | 18.9 | 68.645 | 1.239 | 82.0 | 1.49 |

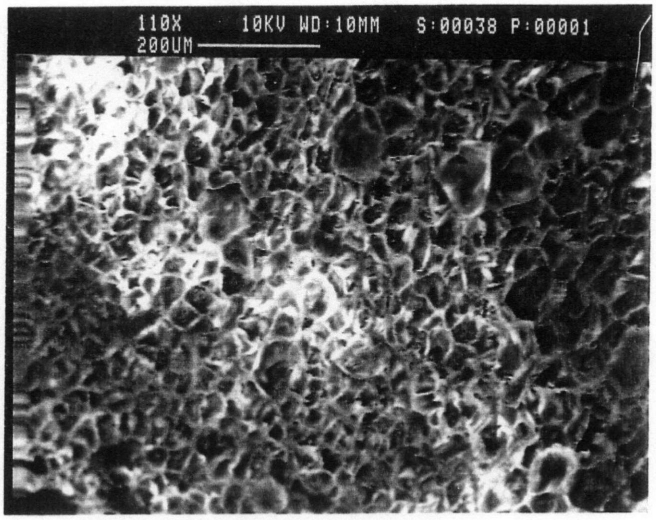

*Figure 3.20: PFA foam produced at 288°C and 3,500 psi. The cell density is on the order of $10^9$ cells/cm$^3$.*

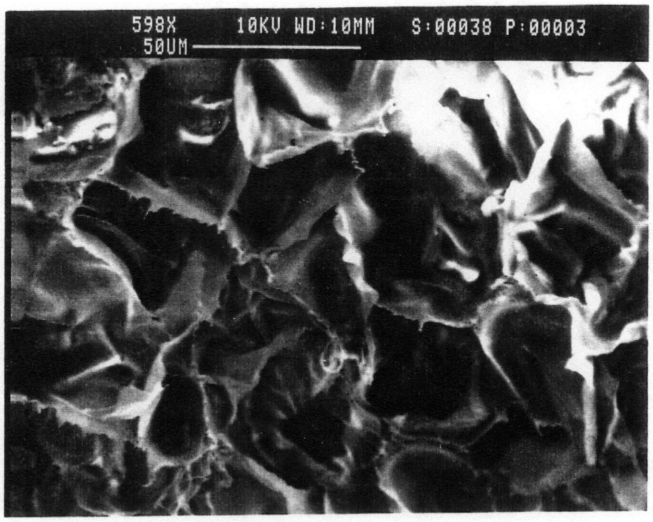

*Figure 3.21: Higher magnification of the PFA sample foamed at 288°C and 3,500 psi.*

## 3.4 Conclusions

The results of the batch processing investigation expanded the scope of microcellular processing technology to an important class of semicrystalline polymers known as fluoropolymers. First, the weight gain characteristics of DuPont FEP 4100 and DuPont PFA 440 HP were determined. Both polymers exhibited induced crystallinity as a result of $CO_2$ gas sorption. The maximum weight gain for FEP was 3.43% after 5 hours of saturation while the maximum weight gain for PFA was 3.15% after 4 hours of saturation.

Extensive foaming trials revealed that FEP has a narrow microcellular batch processing window of 10°C. The best cell morphology, produced using a saturation pressure of 5,500 psi, a saturation temperature of 225°C, and a saturation time of 4 hours, was comprised of an average cell size of 6.1 μm and a cell density of $8.5 \times 10^9$ cells/cm$^3$. The sample became opaque and had a smooth surface finish. Aberrations in cell morphology were observed above 235°C, with occasional large cells distributed among micron-sized cells.

FEP coated wires were also batch processed to determine the effects of microcellular processing on electrical performance. The preliminary results of these tests demonstrated decreases in dielectric constant as high as 31%. Thus, the basic motivating factor of improved electrical performance was realized, indicating that microcellular processing will have a tremendous impact on the wire coating industry. It is important to realize that although the results of batch processing are encouraging, the final implementation of such technology will occur in a continuous process. Hence, the second half of this thesis is dedicated to the design of an extrusion system to coat electrical wires continuously with foamed polymer.

Batch processing of PFA resulted in cell morphologies very close to microcellular morphologies. The full range of experimental conditions could not be tested due to safety limitations of the experimental apparatus. It appears very likely that microcellular PFA can be produced as long as the saturation pressure is greater than 3,500 psi and the saturation temperature is in the neighborhood of 288°C. The best sample produced had an average cell size of approximately 30 μm.

# *CHAPTER 4*

# *EXTRUSION OF MICROCELLULAR FOAM*

## 4.0 Introduction

Extrusion of microcellular foam has enormous potential for industrial applications. Approximately 60% of all plastics material passes through an extruder on its way to conversion to a product (Levy, 1981). In order for microcellular extrusion technology to be commercialized, however, one final hurdle must be crossed: The system must be stable enough to pump a continuous flow of foamed polymer, retaining the desired cell morphology yet having the ability to be shaped into a useful product geometry. This chapter offers a solution for these requirements by laying the groundwork for a new scaled-up microcellular extrusion system (Herrmann, 1994) and then applying it to the specific task of wire coating. To appreciate the scaled-up extrusion system fully, a brief overview of the prototype microcellular extrusion system is provided.

## 4.1 Prototype Microcellular Extrusion System

### 4.1.1 System Description

Park (1993) was the first to demonstrate the feasibility of extruding microcellular foam. His research significantly advanced microcellular processing technology by effecting the transition from batch processing to continuous processing. As mentioned in section 2.2.3, extrusion of microcellular plastics embodies the same requirements as batch processing: gas dissolution, cell nucleation, and cell growth. The prototype system shown in Figure 4.1 consisted of a 3/4 inch extruder (25:1 L/D) (Brabender Model 2523) with a vented screw. Polymer pellets in the extruder hopper descend through the action of gravity into the feed section of the barrel where they are melted. Midway along the barrel, supercritical $CO_2$ is injected into the melt flow. Metering of the supercritical fluid is controlled by a porous metallic material. The large gas bubbles are entrained in the polymer flow and broken into smaller bubbles by the shearing action of the screw. It is critical to

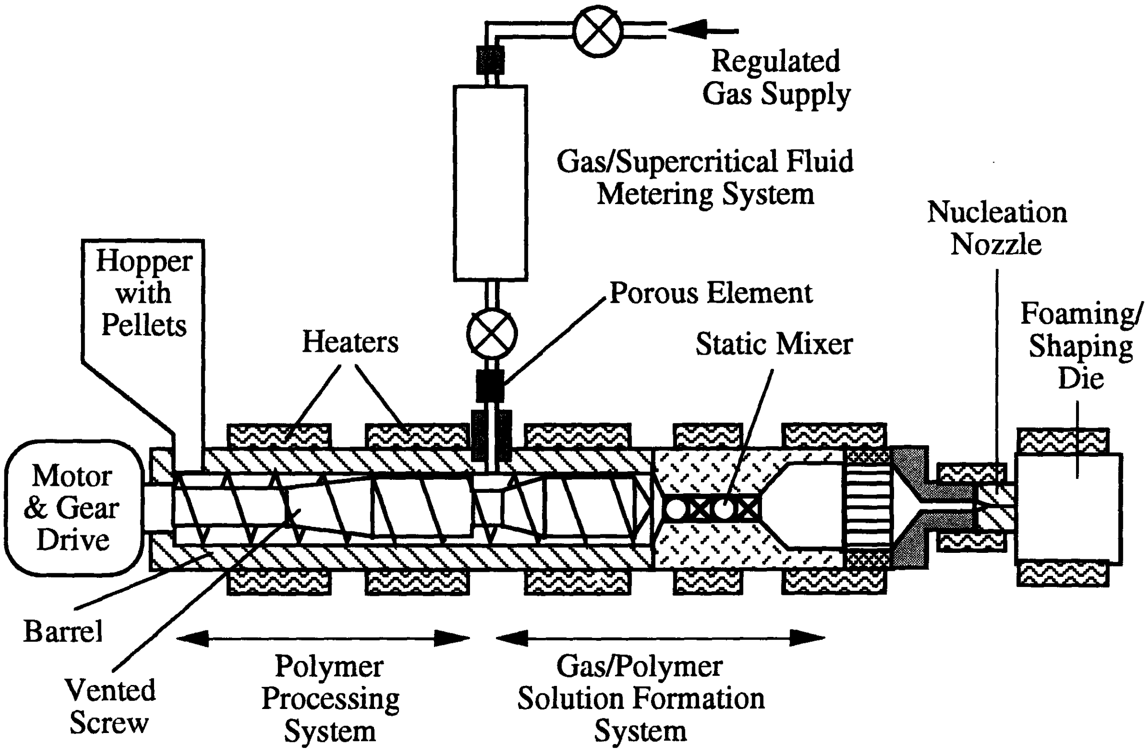

*Figure 4.1: Schematic of prototype microcellular extrusion system (Baldwin, 1994).*

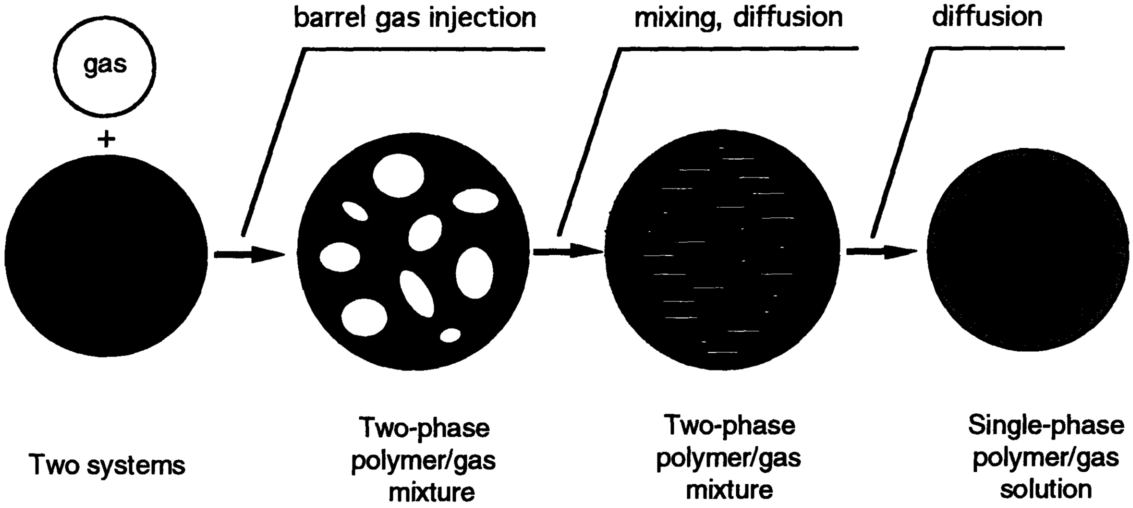

*Figure 4.2: Morphology change of a polymer melt and gas system during a continuous solution formation process (Park, 1993).*

dissolve the $CO_2$ into the polymer melt as much possible to create a single-phase solution. With the assistance of mixing sections on the screw and static mixers, a single-phase solution is created. The morphology change of the polymer/gas system is shown in Figure 4.2. After the single-phase solution is created, the melt is then sent through a nozzle to effect the rapid pressure drop. The result is nucleation of billions of microvoids per cubic centimeter.

Park (1993) produced thin filaments of microcellular high impact polystyrene and microcellular polypropylene having diameters on the order of 0.010 in. A nozzle was used to create the rapid pressure drop which nucleated the single-phase polymer/gas solution. Since thin filaments have limited applicability in manufactured products, alternatives to nozzle-nucleated flows were also investigated (Baldwin, 1994). Baldwin successfully demonstrated near-net shape nucleation, nucleation of a polymer/gas solution flow having dimensions as close as possible to the final product. Thin sheets and tubular films of microcellular polystyrene were the specific geometries manufactured.

### 4.1.2 Operational Difficulties

Experimentation with the prototype system revealed several problems which precluded system stability. Herrmann (1994) extensively analyzed the prototype system, identified the causes of these problems, and offered solutions. His thesis established a scaled-up microcellular extrusion system. This section briefly discusses some of the difficulties of the prototype extrusion system. The reader is referred to Herrmann (1994) for the detailed presentation.

Backflow of Gas Through the Hopper

The vented screw in the prototype system did not generate the ideal pressure profile for microcellular extrusion. The screw possessed a venting region at the $CO_2$ injection port which generated a positive pressure gradient from the feed section to the point of $CO_2$ metering. As gas was injected into the barrel, it sought regions of lower pressure. Since the barrel pressure decreased from the injection port to the hopper, some of the hot gas migrated against the polymer flow and evaded through the hopper. In doing so, polymer pellets in the feed section were often fused into a large clump which blocked the hopper exit and prevented the remaining polymer pellets in the hopper from entering the feed section of the extruder. This condition warranted system shutdown. In addition, gas buildup in the feed section was capable of violently expelling pellets from the hopper, thus creating a safety hazard. A new screw should be designed to eliminate the possibility of gas backflow and to create the maximum pressure at the extruder exit.

### Unreliable Metering of Carbon Dioxide

Carbon dioxide metering was controlled by a porous metallic element and a nitrogen pump. The operator manually adjusted the pressure of the nitrogen pump so that it remained sufficiently above the barrel pressure. This differential pressure forced the carbon dioxide through the porous element and into the barrel. Calibration of the porous element reveals the amount of gas metered for varying differential pressures. If the barrel pressure exceeds the nitrogen pump pressure, however, molten polymer rushes through the stainless steel tubing and clogs the porous element, forcing system shutdown. In a production setting, the clogging of the porous element coupled with the constant attention required to operate the nitrogen pump would render this type of metering system unfeasible.

### Limitation of Saturation Pressure

It was discovered that the higher the saturation pressure, the greater the cell density and the smaller the cells (Park, 1993). Higher pressures (up to the safety limit) could be generated with the prototype extrusion system, however at the expense of sacrificing flow rate. The trade-off associated with obtaining better cell morphology can lead to flow rates too low for economic production. The saturation pressure and flow rate should be decoupled.

### Variation of Nozzle Pressure

Since the prototype system relied on a nozzle as the nucleation device, the pressure drop was a function of flow rate. Therefore, every change in flow rate results in a corresponding change in nozzle pressure. These variations cause fluctuations in the cell morphology of the foamed polymer.

### Limitation of Nozzle Pressure Drop Rate

The nozzle pressure drop rate also depends on nozzle diameter and nozzle length. The smaller the diameter and length, the greater the pressure drop rate. Although higher pressure drop rates result in higher cell densities, the dimensions of the nozzle cannot be reduced indiscriminately because smaller nozzle diameters produce greater polymer shear. The polymer shear rate must remain below the polymer's critical shear rate; otherwise, the polymer can suffer microscale damage which leads to molecular reorientation and anisotropic material response.

Limitation of Product Geometry

Since the nozzle geometry dictates pressure drop and ultimately cell morphology, this geometry imposes limits on the dimensions of the extruded product. Nozzle nucleation cannot produce the full range of thick-walled tubes and sheets. Alternatives to nozzle nucleation should be found if a wide array of shapes and sizes are to be manufactured.

## 4.2 Scaled-up Microcellular Extrusion System

### 4.2.1 Ideal Scaled-up System

In response to the aforementioned difficulties of operating the prototype extrusion system, Herrmann (1994) devised a scaled-up microcellular extrusion system which consists of a single-screw extruder with a grooved feed zone†, a liquid $CO_2$ metering pump, and a gear pump which acts as a nucleation device.

The unique feature of an extruder with a grooved feed zone is that the barrel is no longer simply a cylinder, instead a cylinder with axial conical decreasing grooves. These grooves will have a major impact on microcellular extrusion. Polymer pellets descend into the barrel and fill these grooves. As the screw turns, pellets in the screw flights rub against the pellets trapped in the grooves. The rubbing of the pellets generates tremendous pressures in the feed section of extruder. The corresponding flow rate is also higher in comparison to the flow rate of a conventional extruder. The rapid pressure buildup in the grooved section is entirely dependent on keeping the pellets solid so they can rub against each other. If the pellets in the grooves were to melt, the action of friction would be substantially reduced and the pressure buildup no longer possible. For this reason, the feed section of the grooved extruder must be intensively cooled by circulating fluid through cooling ports in the extruder. The pressure gradient of the grooved extruder is negative after the feed section. Such a pressure profile eliminates gas backflow.

Grooved extruders can be operated at higher pressures than conventional extruders. Therefore, higher solubilities of $CO_2$ in the polymer can be expected as well as shorter saturation times. Because of the larger saturation pressures, higher cell densities of the foamed polymer are also possible. The pressure-flow rate characteristic of a grooved extruder provides nearly constant flow rates over a wide range of resistances. This factor is critical for shaping of the nucleated polymer flow. Shaping dies of varying resistance

---

† Herrmann (1994) suggests the use of a tandem extrusion system if the single grooved extruder does not cool the nucleated polymer sufficiently to prevent excessive cell growth and/or cell coalescence.

can be used without sacrificing flow rate. Because grooved extruders deliver higher flow rates than conventional extruders of the same size, smaller grooved extruders can be used to achieve the same flow rate. Such downsizing reduces system cost.

The difficulties associated with clogging of the porous element which metered carbon dioxide into the extruder barrel in the prototype system was quickly resolved by implementing a conventional metering pump. Liquid metering pumps are used in industry today to deliver a precise amount of fluid and do not require frequent adjustment by the operator.

Perhaps the most innovative idea for the scaled-up extrusion system is the use of a gear pump as a nucleating device. Gear pumps are commonly used in the polymer processing industry to deliver a constant flow rate of polymer and maintain a constant delivery pressure. A cutout view of the gear pump used in this research is shown in Figure 4.3 (The drive shaft and motor are not shown). The apparatus is actually a positive displacement pump consisting of two gears rotating in mesh. The gears are keyed to their respective bearing-supported shafts. The gear/shaft assembly is encased in a heated metal housing. The gear pump is operated by introducing the polymer melt from the extruder to the suction side of the gear pump. The polymer fills the volume between the gear teeth. Meanwhile, power from the pump drive motor causes the gears to rotate clockwise (facing drive end of shaft) and transport the polymer to the discharge side. As the gears mesh, high pressures are generated and the polymer trapped between the teeth is expelled. During operation the gear pump must be carefully cooled to create a seal which prevents leakage of polymer around the shaft. A stainless steel seal is mounted around the shaft but this component alone cannot prevent polymer leakage. The seal is located in a water-cooled section of the gear pump housing. As water passes through the housing, it cools the polymer, causing the polymer to create its own dynamic seal. The polymer itself comprises the primary seal while the metal seal serves as the auxiliary seal during system startup. Water temperature and flow rate should be controlled to maintain proper cooling conditions.

In the microcellular extrusion system, the gear pump will still be used to control flow rate but more importantly, it will be used to effect a very rapid pressure drop across the small length of the gears. This rapid pressure drop will nucleate a very large number of cells. The pressure drop is independent of the gear pump flow rate, thus eliminating some of the problematic issues of nozzle nucleation. Gear pumps nucleate over a large cross

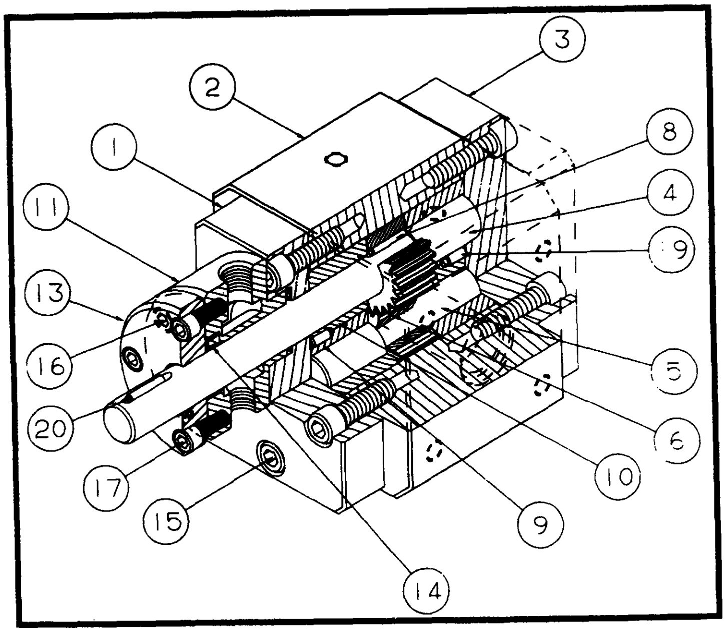

| ITEM | QTY | PART | MATERIAL |
|---|---|---|---|
| 1 | 1 | FRONT PLATE | TOOL STEEL |
| 2 | 1 | CENTER PLATE | TOOL STEEL |
| 3 | 1 | REAR PLATE | TOOL STEEL |
| 4 | 1 | DRIVE SHAFT | TOOL STEEL |
| 5 | 1 | ARBOR | TOOL STEEL |
| 6 | 2 | METERING GEAR | TOOL STEEL |
| 8 | 2 | KEY | |
| 9 | 2 | BEARING | TOOL STEEL |
| 10 | 2 | BEARING | TOOL STEEL |
| 11 | 1 | PARKOOL SEAL | STAINLESS |
| 13 | 1 | SEAL PLATE | STAINLESS |
| 14 | 1 | LIP SEAL | FILLED PTFE |
| 15 | 6 | SOCKET HEAD BOLT | ALLOY |
| 16 | 4 | SOCKET HEAD BOLT | ALLOY |
| 17 | 4 | SOCKET HEAD BOLT | ALLOY |
| 18 | 2 | METAL C-RING | |
| 19 | 2 | KEY | |
| 20 | 1 | KEY | |

**NOTE: .3 - 3 CC/REV HAVE ONLY ONE PARKOOL SEAL.**

*Figure 4.3: Cross-section of the Zenith PEP-II gear pump.*[†]

---

[†] Reproduced with permission from Parker-Hannifin. The figure originally appeared on pg. 4 of the *Zenith Installation, Care and Maintenance Manual for PEP-II Series Gear Pumps.*

section which can be shaped into useful thick-walled product geometries, not just thin sheet and tubes. During operation, the flow rate of the gear pump is fixed by the rotation of the gears. The inlet pressure to the gear pump is determined by the rotation of the extruder screw. Thus, having set the desired flow rate, the gear pump pressure controller adjusts the extruder screw rpm to achieve and maintain the desired gear pump inlet pressure.

### 4.2.2 Implemented Scaled-up System

Due to the lead times and costs associated with grooved extruders, a conventional single-screw extrusion system was implemented.[§] This implemented scaled-up system, however, retained the main essence of the ideal system: the use of a gear pump as a nucleation device. This section provides a description of the actual extrusion setup.

Figure 4.4 presents the layout of wire coating extrusion setup. In brief, after the polymer is plasticated in the extruder, the polymer flow is sent through a device called a *crosshead* which orients the flow perpendicular to the extruder. At the same time, the wire is passed through the crosshead by means of payoff and takeup devices. As a result, the wire is coated with polymer since it is continuously dipped in molten polymer. The details of the components specific to wire coating are reserved for the end of this chapter where theoretical aspects are also discussed. A description of the components in Figure 4.4 follows.

- **Royle Extruder**

A Royle Series 80 Bronfin 1 inch extruder (30:1 L/D) was used to process the polymer foams. The extruder contains 5 heating zones which are heated by cast bronze heaters with external fins. The extruder barrel is air cooled and lined with Xaloy 306, a nickel alloy, for corrosion resistance against fluoropolymers.

- **Screw**

A 1 inch (30:1 L/D) screw was specifically designed to improve the pressure characteristics of the microcellular extrusion system. The screw was manufactured by Davis-Standard from 4340 steel and had 5 sets of mixing pins at the end of the screw for enhanced mixing. The pin rings are located at 17.5D, 18.9D, 20.1D, 21.3D, and 22.5D.

---

[§] The author graciously acknowledges support from Precision Interconnect, the research sponsor, for the donation of the basic wire coating extrusion equipment.

Each ring consists of nine pins spaced on a twelve hole index. The screw was flame hardened as well as chrome plated. Typical screw rpms for wire coating range from 10-30 rpm.

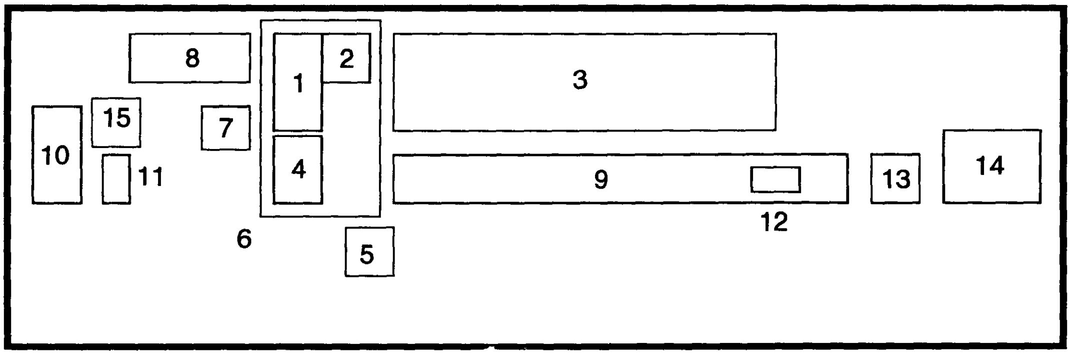

1. Royle Extruder
2. Extruder Drive Motor
3. Extrusion Control Panel
4. Gear Pump/Flange/Crosshead System
5. Gear Pump Control Panel
6. Safety Containment System
7. Carbon Dioxide Metering System
8. Chiller
9. Cooling Trough
10. Wire Payoff
11. Wire Preheater
12. Zumbach Capacitance Meter
13. Wire Coating Thickness Sensor
14. Wire Takeup
15. Power Supply for Wire Preheater and Zumbach Controls

*Figure 4.4: Layout of the microcellular wire coating extrusion system.*

- <u>**Gear Pump/Flange/Crosshead System**</u>

Several flanges were machined to allow connection of the extruder to the gear pump and other flow shaping dies as well space for thermocouples and pressure transducers. Figure 4.5 presents an assembly diagram for the various flanges. (This figure contains wire coating components such as the crosshead adapter and the crosshead itself. These items are discussed in section 4.3.) Both the Gear Pump Inlet Flange and the Gear Pump Outlet Flange were machined from 4140 Steel and subsequently heat treated to a minimum of 41 HRC (certified between 45-47 HRC). The flanges were quenched in sodium nitrate and processed per MIL-H-6875H. The drawings of the inlet and outlet flanges are presented in Figures 4.6 and 4.7. The adapter disks shown in Figure 4.5 were necessary to provide a proper sealing surface for the polymer flow. These disks were also machined from 4140 steel and heat treated to 41 HRC minimum. Their drawings are shown in

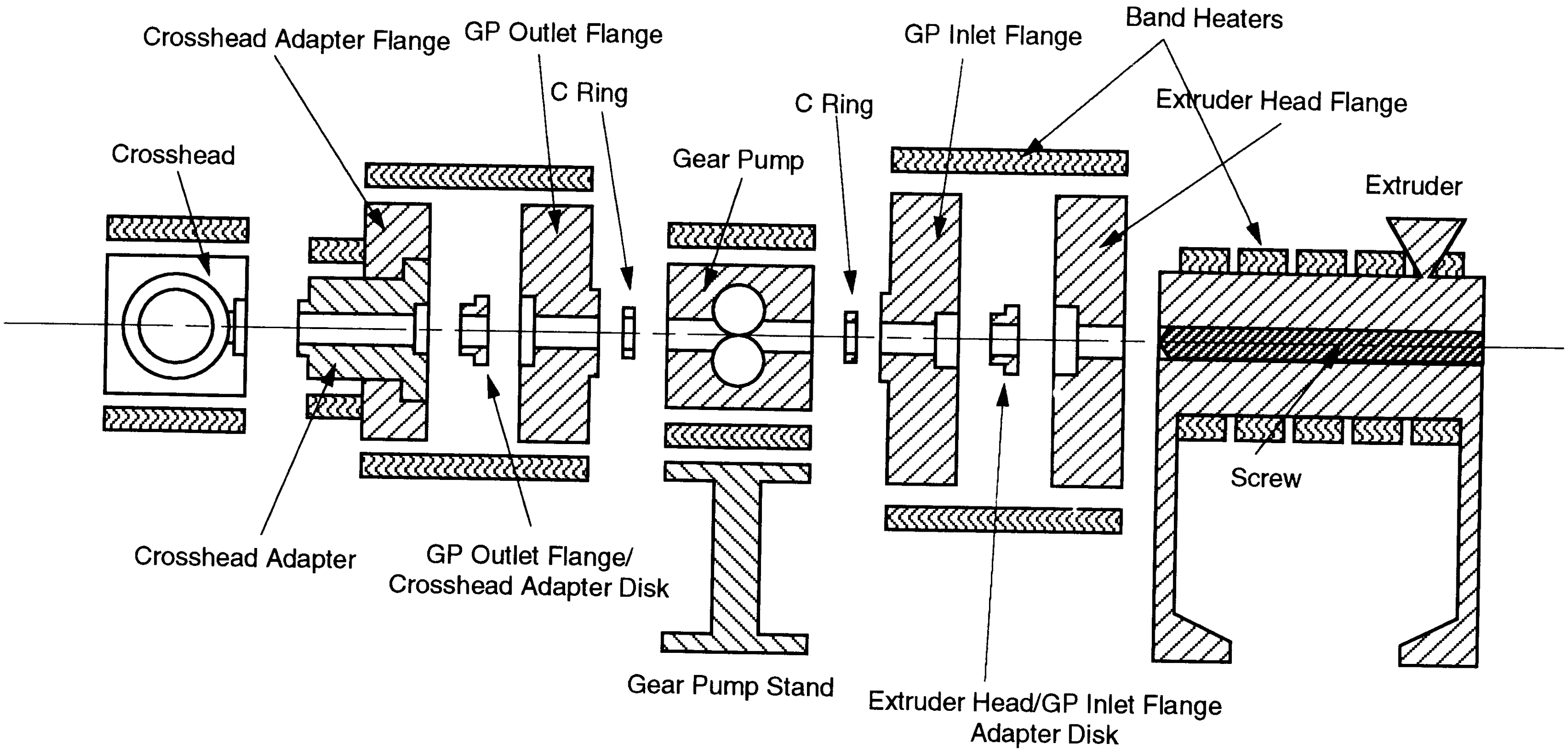

*Figure 4.5: Assembly drawing for extruder, flanges, and gear pump.*

Figures 4.8 and 4.9. The bolt tightening torques for the various flanges are shown in the drawings, as well. All the bolts were lubricated with a copper paste to prevent thread seizing as a result of thermal cycling. Both the inlet and outlet gear pump flanges were fitted with pressure transducers (Industrial Sensors, Inc., #0121-10.0T-6-M259 and #0121-5.0T-6/18-M259). These sensors provided the feedback needed for the gear pump to control the extruder screw rpm.

### Gear Pump

A Zenith PEP-II Series Gear Pump was implemented in the extrusion system, as shown in Figure 4.3. The pump has a maximum capacity of 3 cc/rev and meters 4-24 lbs/hr. It can operate at a maximum pressure of 10,000 psi, a maximum differential pressure of 4,000 psi, and a maximum temperature of 950°F (510°C). The gear pump provides a 600 in-lb maximum torque which is supplied by a 1/2 HP DC drive motor (1750 rpm/4.7 A/90 V). Since it is crucial to obtain precise alignment of the gear pump with the extruder barrel, a leveling stand was designed to allow height adjustment of the gear pump. The gear pump leveling stand is presented in Appendix B.4. In essence, the gear pump base is bolted down to an aluminum base by three 1/2-13 bolts while three additional 1/2-13 bolts come from underneath the aluminum base and contact the underside surface of the gear pump base. Adjustment of the latter bolts varies both the height and the angular orientation of the gear pump.

### Rupture Disks

Custom-designed rupture disk assemblies were obtained from Anderson, Greenwood Rupture Disks, Inc., to offer a measure of safety to both the operator and the equipment in the event of an over-pressurization. The assembly actually consists of a 3/16 inch diameter curved metallic disk soldered to a threaded 316 stainless steel rod, as shown in Figure 4.10. A rupture disk assembly was placed in each of the gear pump flanges. The gear pump inlet rupture assembly was rated to 9,000 psi at 800°F while the outlet rupture assembly was rated to 5,000 psi at 800°F. The soldered disk portion of the assembly contacts the polymer melt flow.

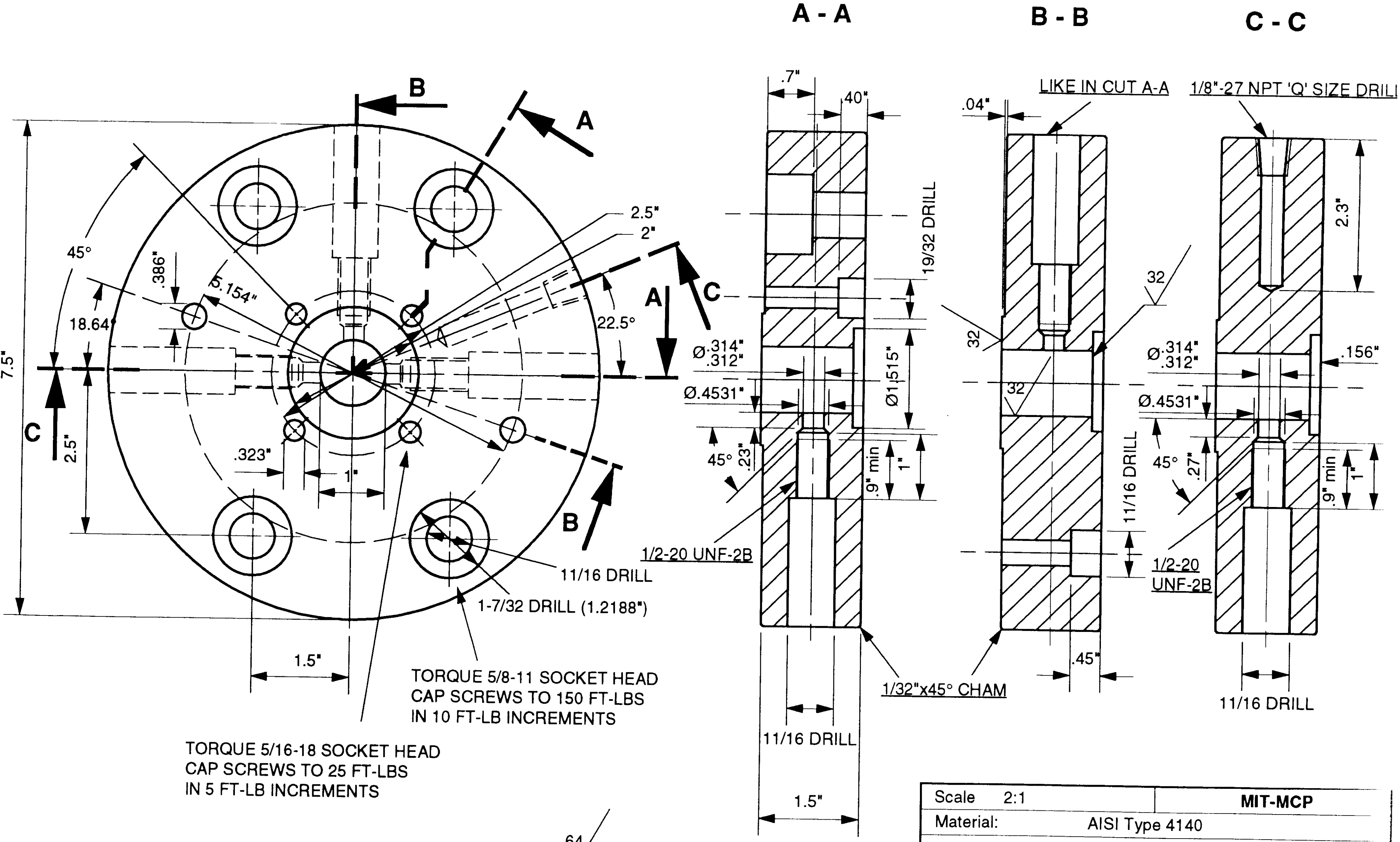

64

general tolerances ± 0.003"

Heat Treat to HRC 41

| | |
|---|---|
| Scale 2:1 | MIT-MCP |
| Material: AISI Type 4140 | |
| GEAR PUMP INLET<br>FLANGE | |
| Date: 09/21/94 | Name: Herrmann/Patil<br>Sheet 1/1 |

*Figure 4.6: Gear Pump Inlet Flange.*

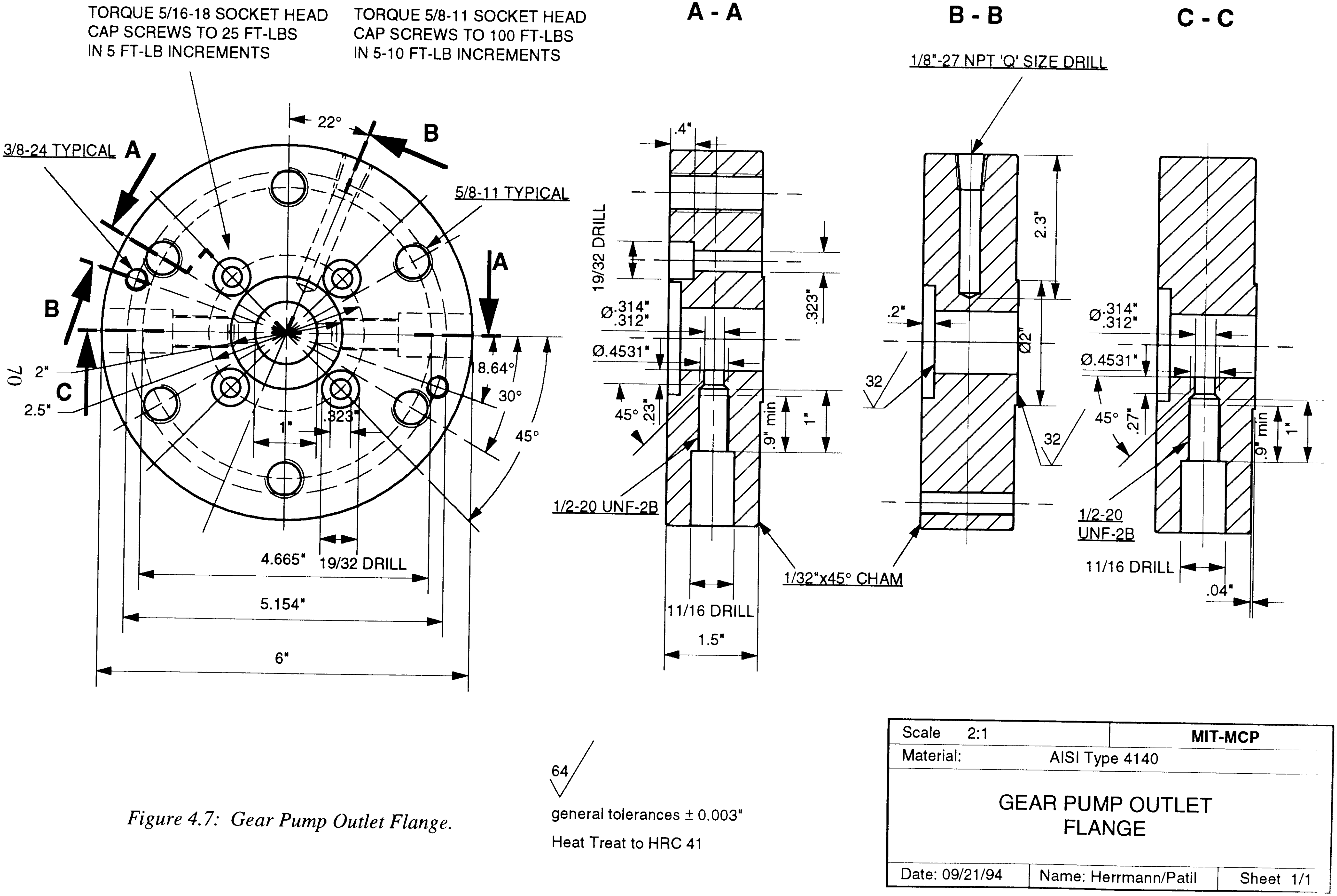

*Figure 4.7: Gear Pump Outlet Flange.*

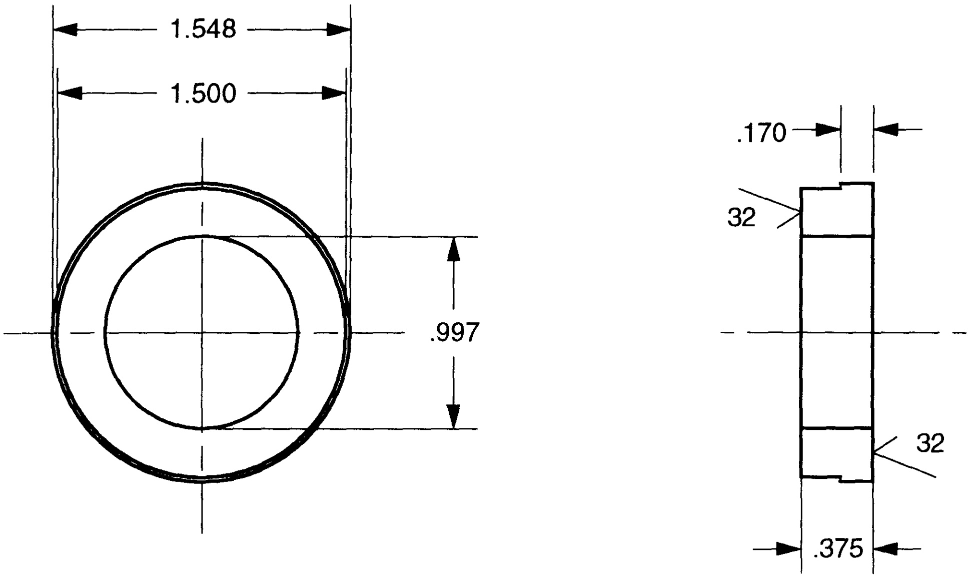

*Figure 4.8: Extruder Head/Gear Pump Inlet Flange Adapter Disk.*

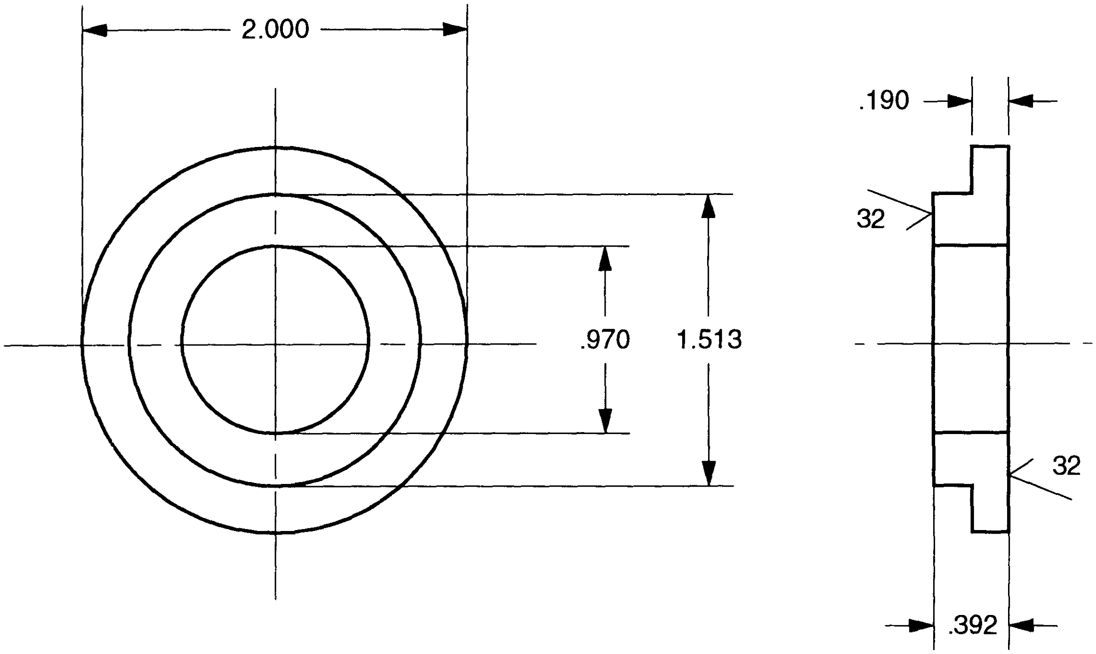

*Figure 4.9: Gear Pump Outlet Flange/Crosshead Adapter Disk.*

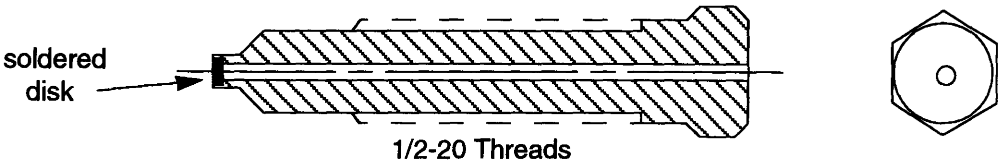

*Figure 4.10: Schematic of the rupture disks installed in the flanges.*

**Band Heaters**

Due to the presence of thermocouples, pressure transducers, and rupture disks in the various flanges, the flange band heaters were custom-manufactured by Watlow, Inc. with the appropriate holes. The band heaters, shown as flat views in Figures 4.11 and 4.12, are comprised of a heating wire sandwiched between layers of mineral insulation and a stainless steel sheath. Mineral insulation has a higher thermal conductivity than both the mica and ceramic used in conventional band heaters.

- **Safety Containment System**

Polycarbonate sheets obtained from General Electric Plastics were used to fabricate a safety containment system to protect the operator in the event of an extruder or metering system explosion. The different views of the containment device are shown in Appendix B.3. Many bolt holes and valve/tubing openings not pictured in these drawings were also drilled into these sheets. The polycarbonate sheets were 3/8 inch thick and fastened with 14 gauge steel angles (McMaster-Carr #4664T33), 14 gauge galvanized steel gusset plates (McMaster-Carr #4664T22), and 3/8-16 inch nuts and bolts. The steel angles measured 2-1/4 inches by 1-1/2 inches by 10 feet.

- **Carbon Dioxide Metering System**

Instead of using a porous metallic element to meter the carbon dioxide into the barrel, the scaled-up extrusion system implemented a diaphragm metering pump (Lewa FCM-08). The entire metering system is shown in Figure 4.13 and the corresponding bill of materials is presented in Appendix B.2. The metering system was operated by feeding 850 psi $CO_2$ gas (Bone-Dry Grade 2.8, 99.8% pure) from a pressurized cylinder to the liquefaction chamber. The liquefaction chamber simply consisted of a thick-walled

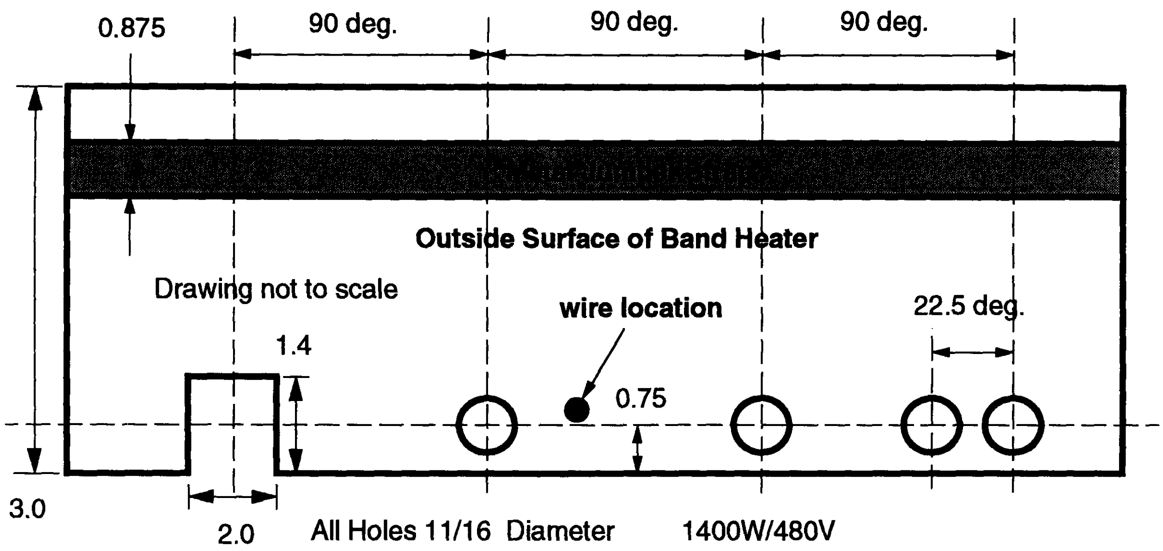

*Figure 4.11: Extruder Head/Gear Pump Inlet Flange Band Heater.*

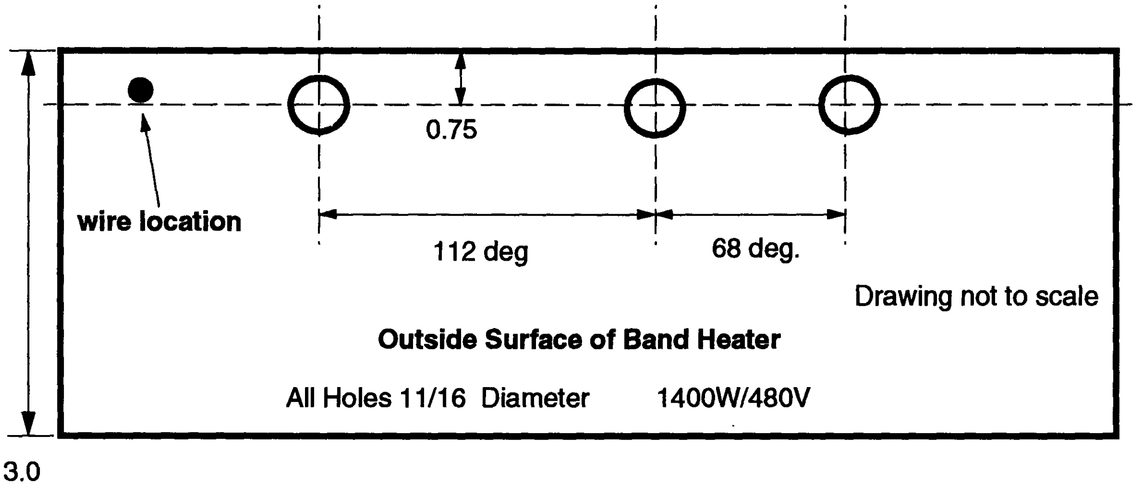

*Figure 4.12: Gear Pump Outlet Flange/Crosshead Adapter Flange Band Heater.*

stainless steel cylinder which was placed in a 4.6 $ft^3$ freezer (General Electric Compact Freezer CB5DM) to liquefy the $CO_2$. The freezer operated at 117 VAC/ 1.7 A/ 60 Hz and was capable of cooling its interior to -8°F when operated at ambient conditions. The liquid $CO_2$ was then fed into the suction valve of the metering pump. The metering pump was also mounted inside the freezer. The pump precisely regulated the flow leaving through its discharge valve. Upon exiting the metering pump, the liquid $CO_2$ was conveyed through a check valve. The "metering pressure" was recorded at this point. Before passing the liquid through a filter which prevented large particles from ultimately entering the gear pump and destroying the gears, the liquid $CO_2$ passed by one manual relief valve as well as an automatic relief valve set to discharge at 5,000 psi. Upon filtration, the metered fluid was passed through a high temperature valve and finally, the injection stem which transported the fluid into the extruder barrel. The injection port on the barrel is located at 16.5D. To prevent molten polymer from climbing up the injection stem and solidifying in the metal tubing, the high temperature valve and the injection stem were heated by a double-braided flexible fiberglass heating tape (Briskheat BWH 102-060) as shown in Figure 4.13. Clogging in the tubing immediately results in metering system failure. The pressure at the injection stem/barrel was measured by a pressure transducer (Dynisco PT460EH-10M-6) as well.

The metering pump head had two cooling ports for hydraulic fluids. If the carbon dioxide inadvertently vaporizes before the metering pump or in the pump head itself, the pump experiences vapor lock and control of the fluid metering is completely lost. It is, therefore, necessary to cool the pump head continuously. The pump head is warmed by the ambient surroundings, the heat generated by the pump drive motor, and the heat generated by the compression of the carbon dioxide in the pump head. To avert vapor lock, water chilled at 8°C was circulated through the pump head and the stainless steel tubing leading to the metering pump was placed in an ice bath. This cooling method did not prove effective because the metering pump only achieved a maximum pumping pressure of 3,000 psi rather than 5,000 psi. As a result, the water lines to the pump head were disconnected and instead, the entire metering pump itself was placed in a freezer, as mentioned earlier.

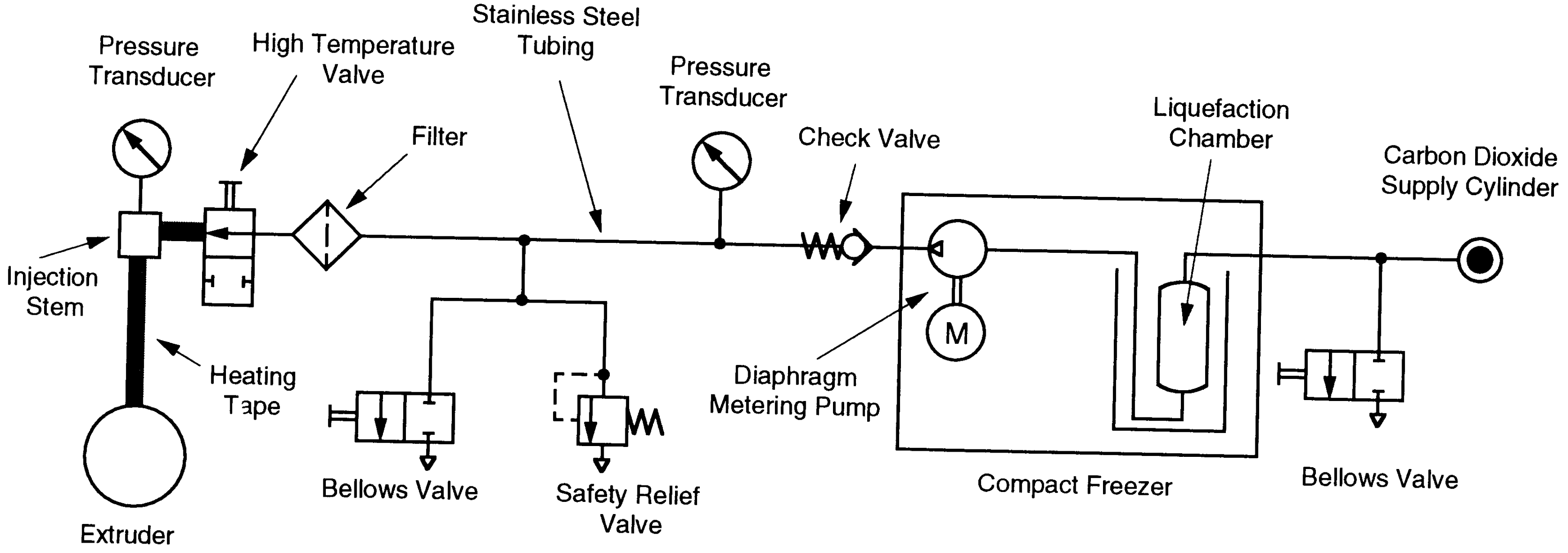

Figure 4.13: Schematic of carbon dioxide metering system.

A description of some of the individual components shown in Figure 4.13 follows. The metering pump drive unit consists of a cam and return spring arrangement. A 1/2 HP DC motor drives an eccentric shaft via a worm gear, initiating the delivery stroke of the plunger rod. This motion deflects a 316 stainless steel diaphragm and compresses the return spring. The suction stroke which retracts the diaphragm is created by the extension of the return spring. This section of metering pump is lubricated with a gear oil having an approximate kinematic viscosity of 220 $mm^2/s$ at 40°C and a lower operating temperature limit of -20°C. The pump's relief valve was manually calibrated to a 6,000 psi cracking pressure. For efficient fluid delivery, the pump was operated at its maximum stroke length while the rpm was manually adjusted.

The metering pump suction and delivery valves were both double-balled check valves rated to 10,000 psi. The valve housing was constructed from 316 stainless steel and the balls were made from Hastelloy. Two balls were used in this situation to assure proper sealing and precise metering. The valves were threaded into the pump head and torqued to 12-14 ft-lbs. (Subsequent reassembly called for torques up to 25 ft-lbs to regain proper sealing.) The valve threads were coated with Permatex Antiseize Lubricant (Loctite Corp. Part #133K) to prevent galling and seizing. This paste operates between -65°F and 2000°F.

The metering pump was originally supplied with glycerin hydraulic oil (G-80). This organic substance degrades over time and promotes algae growth. Furthermore, when cooled to the temperatures needed to maintain liquid carbon dioxide, glycerin becomes highly viscous and impairs pump operation. This oil was flushed out with denatured alcohol (Lynsol) and replaced with mineral oil (M-10) having a lower operating temperature limit of -10°C.

The soft seat check valve located after the metering pump was manufactured from high tensile 316 stainless steel rated to 10,000 psi. The check valve ensures flow in one direction only and can be mounted in any direction. It was installed in the system to prevent metered carbon dioxide from re-entering the metering pump in the event of a pressure imbalance.

The line filter was also rated to 10,000 psi. Its primary function was to prevent any particles and impurities from entering the extruder barrel and ultimately destroying the gear pump. The filter consists of four sintered stainless steel disks with 65 μm filtration capability. The filter body was constructed from high tensile 316 stainless steel.

The high temperature valve had a 30,000 psi pressure rating. It was fitted with a special high temperature extension which removed the valve packing area from the hot zone of the valve. The extension had fins around the packing area which dissipated heat. If the packing area is cooled properly, the valve can be operated at temperatures as high as 1000°F (538°C).

The injection stem assembly consisted of three stainless steel pieces. The top housing piece had a flow inlet for the carbon dioxide as well as a female port for a pressure transducer. The bottom housing piece enclosed a narrow injection stem which sealed against the top housing piece via a 110 PTFE O-ring. The bottom of the injection stem threaded directly into the extruder barrel. The top and bottom housing pieces threaded into each other. As mentioned previously, the injection stem assembly was wrapped with electrical heating tape to prevent solidification of any entrapped polymer.

- **Water Cooling System**

The cooling system is integral to the proper operation of the microcellular extrusion system. The general flow diagram is shown in Figure 4.14 while the detailed assembly drawing is presented in Appendix B.1. A cooling system is necessary to cool the extruder gearbox and to cool the gear pump in order to prevent leakage of polymer around the drive shaft, as explained earlier.

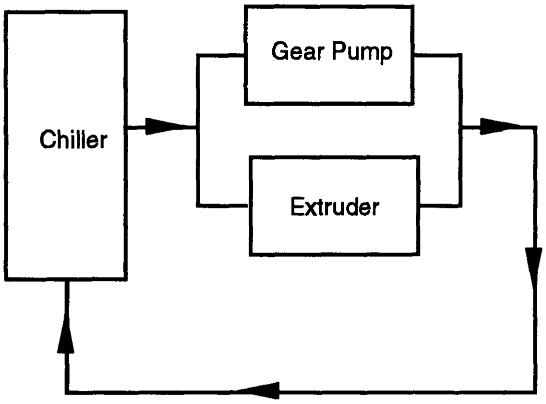

*Figure 4.14: Cooling system schematic.*

The cooling system employed a Thermocool Conair-Churchill chiller (Model #TCA9) to maintain a constant temperature water flow. The chiller consists of two separate systems coupled by a heat exchanger: the refrigeration circuit and the water circuit. The refrigeration circuit operates by alternately evaporating a low boiling point liquid at low pressure and condensing it at high pressure. The high pressure liquid is then passed through a heat exchanger where it absorbs a significant amount of heat energy and vaporizes again. In the water circuit, the water is cooled by passing it through the aforementioned heat exchanger and then pumped throughout the system. The Conair chiller had a net cooling capacity of 9.2 kW at 15°C and operated with a 31 L/min flow rate at 1.9 bar (27.5 psi). The chiller tank had a total volume of 40 L. The chiller was operated at 8°C.

## 4.3 Principles of Wire Coating

### 4.3.1 Wire Coating System Layout

This chapter has primarily discussed the design of the scaled-up microcellular extrusion system. An explanation of the wire coating components will complete the discussion. The simplified frontal view of the microcellular wire coating line without the cooling and metering systems is shown in Figure 4.15. (The plan view was presented in Figure 4.4). The payoff continuously unwinds the wire from the spool and feeds it through the wire preheater and the crosshead. It is necessary to preheat the wire so that the wire does not cool down the crosshead components and create flow instabilities. Meanwhile, as shown in Figure 4.5, the nucleated polymer flow proceeds from the gear pump through the crosshead adapter and adapter flange (Figure 4.16) and enters the crosshead where it is oriented parallel to the moving wire. The wire is coated with polymer and exits into the cooling trough where a capacitance measurement is taken. Before being wound onto the takeup spool, a coating thickness measurement is taken. The payoff and takeup floating dancer arms convey the wire at constant tension over a wide range of winding velocities.

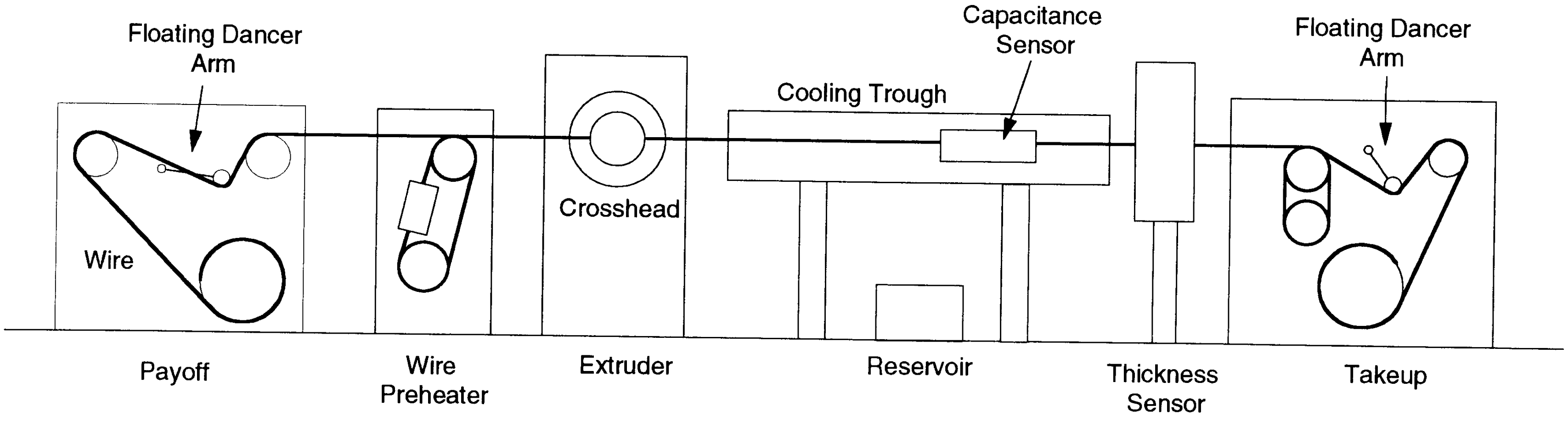

*Figure 4.15: Simplified frontal view of the microcellular wire coating line.*

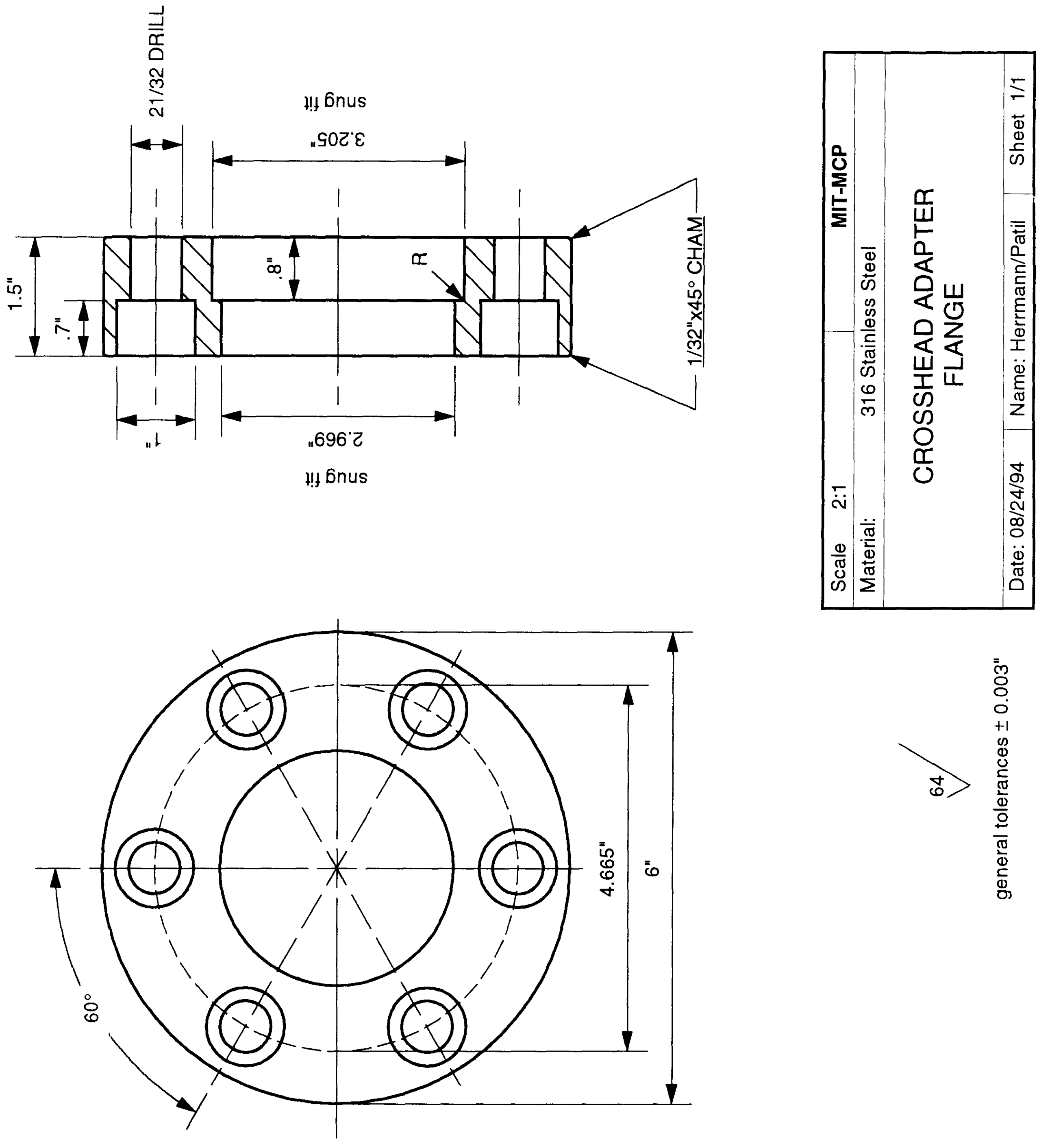

*Figure 4.16: Crosshead adapter flange.*

### 4.3.2 Crosshead System

An exploded view of the crosshead system is provided in Figure 4.17 (next page). A typical crosshead assembly view is shown below in Figure 4.18. The guides (also referred to as *guider tips* or *tips*) and dies can be interchanged to accommodate different gauge wires and coating thicknesses. The internal flow channel of the crosshead must produce streamlined flow without having stagnation points. These areas lead to resin degradation. There are two basic wire coating methods, tube extrusion and pressure extrusion, which depend upon the specific arrangement of the die and guide.

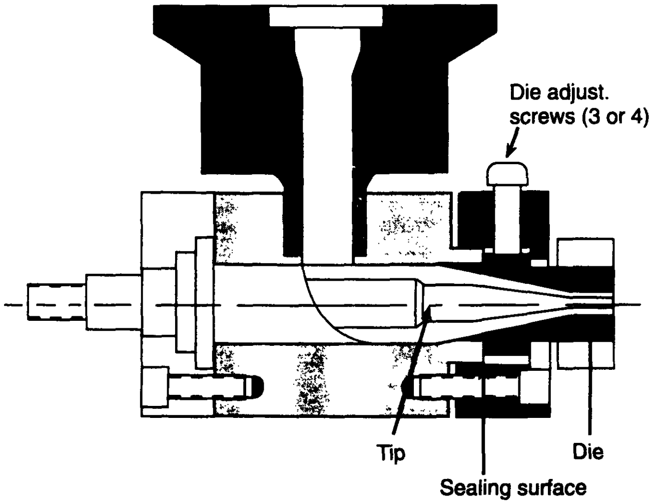

*Figure 4.18: Typical assembly view of the crosshead.*[†]

---

[†] Reproduced from DuPont *Extrusion Guide for Melt-Processible Fluoropolymers*, p. 24.

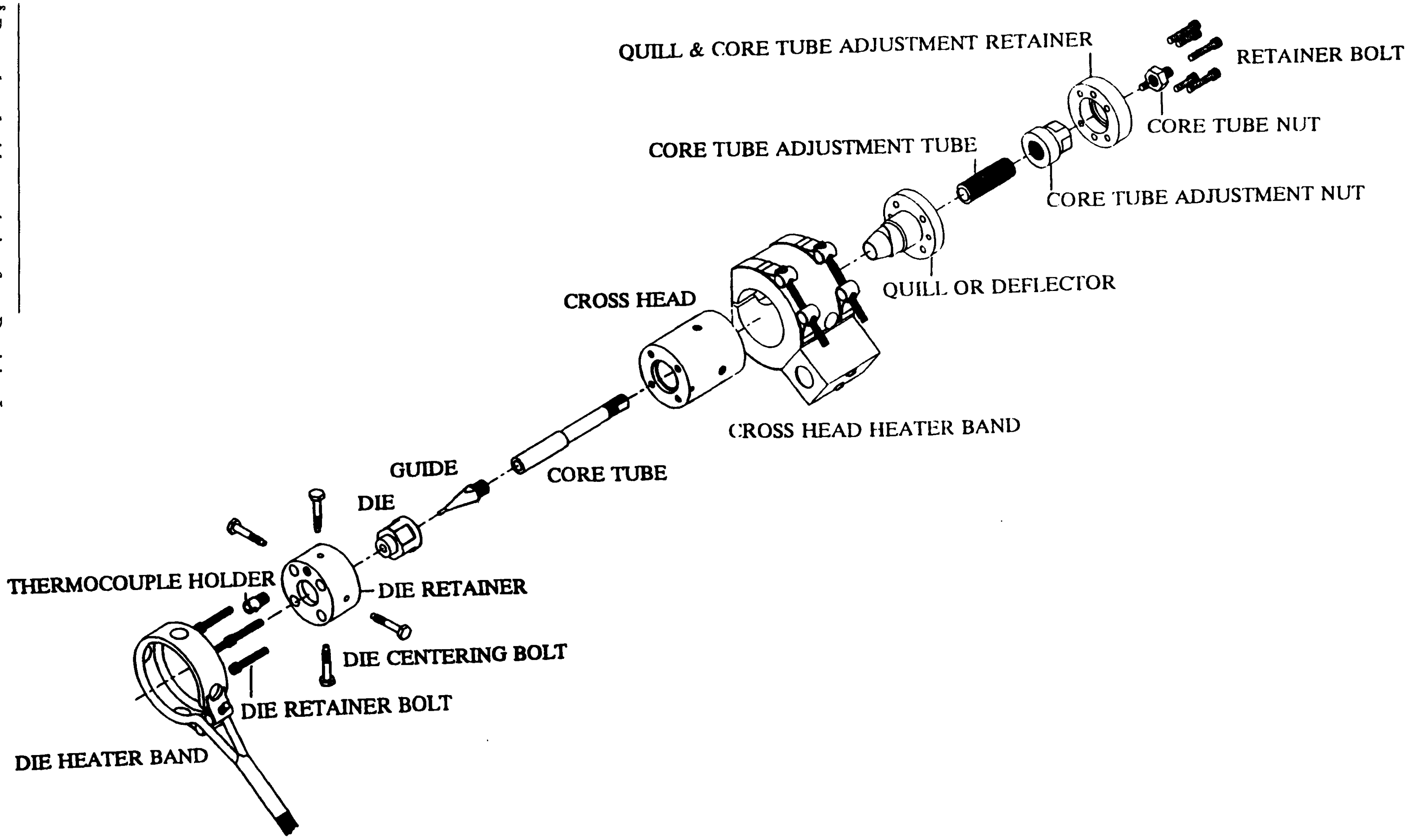

*Figure 4.17: Exploded view of the crosshead system.*

---

§ Reproduced with permission from Precision Interconnect.

## Tube Extrusion

The first method is termed *tube extrusion* because if the wire were removed, the resulting product would be an extruded tube. Figure 4.19 depicts the die-guide arrangement for tube extrusion (DuPont #H-28461-2),

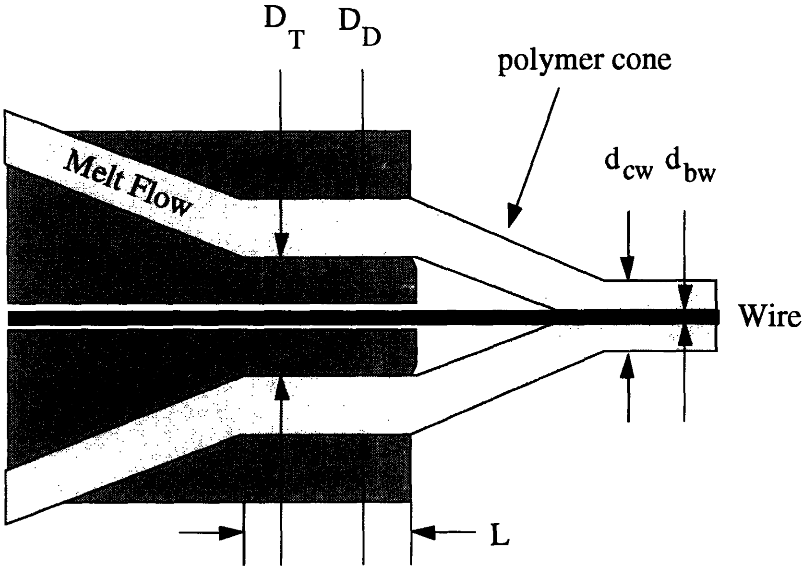

*Figure 4.19: Geometry of the tube wire coating process.*

where

$D_T$ = outer diameter of the guider tip [in]
$D_D$ = inner diameter of the die opening [in]
$d_{cw}$ = outer diameter of the coated wire [in]
$d_{bw}$ = diameter of the bare wire [in]
$L$ = die land length [in]

The polymer melt forms a cone around the wire which is drawn down by the wire's motion.

Two dimensionless parameters have been developed to characterize tube wire coating geometries. The draw down ratio (*DDR*) is the ratio of cross-sectional area of the annular die opening to the cross-sectional area of the finished insulation. *DDR* is limited by the maximum die size the crosshead can accept.

$$DDR = \frac{D_D^2 - D_T^2}{d_{cw}^2 - d_{bw}^2}. \tag{4-1}$$

The draw ratio balance (*DRB*) compares the degree to which the inner and outer polymer melt flow surfaces are drawn. Typically, to obtain uniform diameter and concentricity, the inside of the extruded resin should be drawn the same amount as the outside. If this condition is satisfied, the draw is balanced (*DRB* = 1). Materials with lower melt strengths are more sensitive to *DRB*. *DRB* generally ranges from 0.9 to 1.1. In some materials, if *DRB* is less than 0.9, the insulation can become oval. If *DRB* is above 1.1, pinholes and breaks in the insulation can occur.

$$DRB = \frac{D_D / d_{cw}}{D_T / d_{bw}}. \tag{4-2}$$

To obtain tight insulation around the wire, a vacuum is sometimes applied in the crosshead cavity so that the suction pulls the polymer cone closer to the wire (DuPont #H-28461-2).

The tooling sizing procedure for tube wire coating is aided by these dimensionless parameters. Based on experience with the given polymer, *DDR* and *DRB* are typically known. From the definitions of *DDR* and *DRB*, the relevant die-guide dimensions are readily calculated.

$$D_T = \sqrt{\frac{DDR(d_{cw}^2 - d_{bw}^2)}{DRB^2\left(\frac{d_{cw}}{d_{bw}}\right)^2 - 1}}. \tag{4-3}$$

$$D_D = D_T DRB\left(\frac{d_{cw}}{d_{bw}}\right). \tag{4-4}$$

If *DRB* is unknown, a starting value of unity is typically assumed; equations (4-3) and (4-4) then reduce to the following equations:

$$D_T = d_{bw}\sqrt{DDR}. \tag{4-5}$$

$$D_D = d_{cw}\sqrt{DDR}. \tag{4-6}$$

It is important to keep the shear rate in the die region below $\dot{\gamma}_{cr}$, the critical shear rate of the polymer; otherwise, melt fracture occurs, leaving a rough surface finish. Melt fracture is actually tearing of the polymer melt and is unacceptable in the finished product. It is typically alleviated by increasing the temperature of the polymer.

The estimated shear stress at the die wall, τ, is

$$\tau_w = \frac{PH}{2L} \quad \text{[psi]}, \tag{4-7}$$

where $P$ is the pressure drop across the die land [psi],

while $\dot{\gamma}_w$, the estimated shear rate at the die wall, is

$$\dot{\gamma}_w = \frac{6q}{WH^2} \quad [\text{sec}^{-1}], \tag{4-8}$$

where $q$ is the volumetric flow rate [in$^3$/sec];

$W$ is the average die circumference

$$W = \pi\left(\frac{D_D + D_T}{2}\right) \quad \text{[in]}; \tag{4-9}$$

$H$ is the annular die opening

$$H = \frac{D_D - D_T}{2} \quad \text{[in]}. \tag{4-10}$$

Setting equation (4-8) equal to the critical shear rate, the maximum extrusion rate is found to be

$$Q_{\max} = 600\dot{\gamma}_{cr}\rho WH^2 \quad \text{[lbs/hr]}, \tag{4-11}$$

where ρ is the polymer melt density [lbs/in$^3$] (DuPont #H-28461-2). Therefore, the maximum wire coating rate is

$$V_{\max}^{wire} = \frac{15}{2700\pi} \frac{Q_{\max}}{\rho} \frac{1}{\left(d_{cw}^2 - d_{bw}^2\right)} \quad \text{[ft/min]}. \tag{4-12}$$

Pressure Extrusion

In contrast to tube extrusion, pressure extrusion does not involve drawdown of the polymer. As shown in Figure 4.20, the die opening is equal to the desired coating diameter. If the insulation material undergoes excessive shrinkage during cooling, then the die opening is made larger to compensate for the contraction. Pressure extrusion has been known to run with fewer melt breaks and the insulation is tighter around the wire. The primary use of pressure extrusion is to coat stranded or helical wound wires with a constant outer diameter insulation coating. For the case of helical wound wires, if tube extrusion had been used, the insulation geometry would have matched the profile of the curving wire surface and hence, a circular outer profile could not have been obtained.

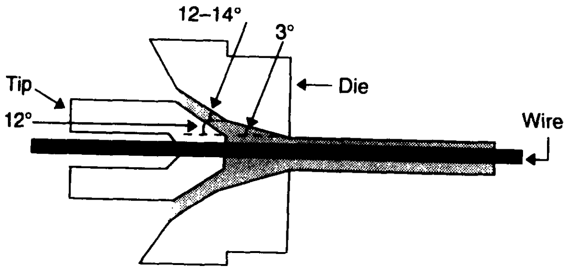

*Figure 4.20: Geometry of the pressure wire coating process.*†

## 4.4 Conclusions

Based on the experience of the prototype microcellular extrusion system, a scaled-up system was proposed (Herrmann, 1994). The hallmark of this improved design is the use of a gear pump as a nucleating device. The gear pump will meter a precise flow rate of nucleated polymer which will then be passed through a crosshead for the purpose of coating wires. Having obtained an understanding of wire coating extrusion process, the next chapter switches focus to the electrical performance of the coaxial cable.

---

† Reproduced from DuPont *Extrusion Guide for Melt-Processible Fluoropolymers*, p. 23.

# CHAPTER 5

# ANALYSIS OF COAXIAL CABLE PERFORMANCE

## 5.0 Introduction

Having devised a manufacturing process to coat electrical wires continuously with a microcellular foamed polymer, it is important to revisit the motivations for creating such a system in the first place before proceeding with the experimental results of the extrusion system. As discussed in chapter 1, extrusion of dielectric insulation around the wire is a much faster process than the conventional tape winding process. It was also shown that handsome cost savings could be achieved due to the low-density materials that are created with microcellular processing. Furthermore, microcellular processing involves relatively environmentally-friendly gases such as a carbon dioxide and nitrogen compared with the chlorofluorocarbons and hydrocarbons of conventional foam processing. This chapter, however, discusses the final primary advantage of a microcellular foam wire coating process, the improvement in electrical performance. The chapter begins with a discussion of the dielectric constant and capacitance of various geometric arrangements and explains how foamed insulation lowers the effective dielectric constant of the system. The final section draws upon the experience of the wire coating industry by presenting various empirically determined equations which describe the electrical performance of coaxial cables.

## 5.1 Dielectric Constant Reduction

In order to justify the claim that a foamed dielectric wire insulation reduces the dielectric constant of the system and improves electrical properties, the analogy between coaxial cables and parallel plate capacitors will be made. Discussion of dielectric performance is often made in the context of capacitance, the property of an electrical system which allows storage of electrostatic energy (Ohanian, 1989). Capacitance is measured in units of farads [F]. A common capacitor consists of two parallel metallic conductors each carrying amounts of electric charge $\pm Q$ and separated by a distance $d$, as depicted in

Figure 5.1. The charges on the capacitor plates are free to move about and redistribute themselves.

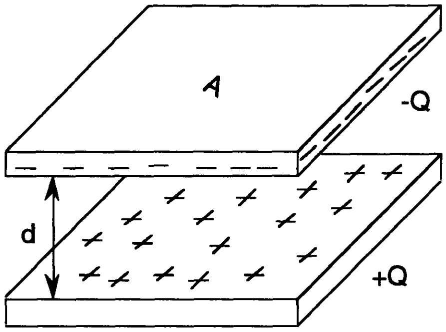

*Figure 5.1: Parallel plate capacitor.*

The capacitance of this arrangement is given by

$$Q = C\Delta V, \tag{5-1}$$

where $C$ is the capacitance [F] and $\Delta V$ is the potential difference [V]. $Q$ is the magnitude of charge on each plate in units of coulombs [C]. (Note that the net charge of the capacitor is zero.) Neglecting edge effects, the electric field in the space between the plates is

$$E = \frac{Q}{\varepsilon_o A}, \tag{5-2}$$

where $\varepsilon_o$ is the permittivity constant ($8.85\text{x}10^{-12}$ $C^2/N\text{-}m^2$) and the potential difference is

$$\Delta V = Ed = \frac{Qd}{\varepsilon_o A}. \tag{5-3}$$

Hence, the capacitance is found to be

$$C = \frac{Q}{\Delta V} = \frac{\varepsilon_o A}{d}. \tag{5-4}$$

The equations above assume that a vacuum exists in the space between the conductors. However, in reality, the electric field is reduced slightly due to air and can be reduced even further in the presence of insulating materials such as dielectrics. The construction of a coaxial cable is similar to that of the parallel plate capacitor insulated with a dielectric medium shown in Figure 5.2. Like the parallel plate capacitor in Figure 5.2, the coaxial cable pictured in Figure 1.1 consists of 2 conducting regions separated by a dielectric medium.

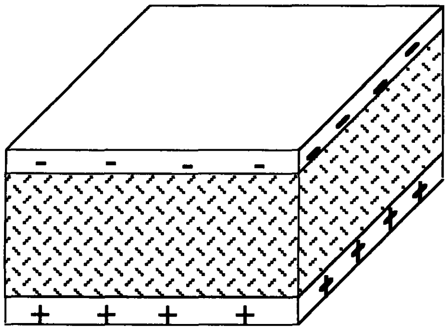

*Figure 5.2: Parallel plate capacitor completely insulated with dielectric.*

The presence of the dielectric medium alters the electric field in the region between the conducting plates because of the polarization phenomenon. Since dielectrics are insulating materials, they are electrically neutral and have bound charges. The electrons are confined within their atoms or molecules and are not free to wander into the orbits of the neighboring atoms. However, when exposed to an external electric field, the bound charges can be displaced a small distance. Electric dipoles are created within the dielectric as the positive and negative charges are pulled in opposite directions. As seen in Figure 5.3, since the distributions of positive and negative charges do not overlap exactly, charge separations on the microscopic scale lead to an overall macroscopic distribution of charged particles.

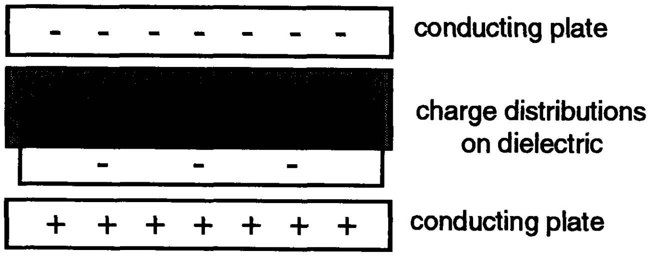

*Figure 5.3: Surface charge buildup on dielectric due to an applied electric field.*

Because a net positive charge develops on the top face of the dielectric and a net negative charge develops on the bottom face, the dielectric is said to be polarized. Surface charges on the dielectric behave like parallel plates themselves, generating an electric field *opposite* to the applied electric field. Since the total electric field is the sum of the electric field of the free charges on the conducting plates and the electric field of the bound charges of the dielectric, the total electric field is smaller than the field created by the conducting plates alone. The electric field reduction in the presence of a dielectric is shown schematically in Figure 5.4.

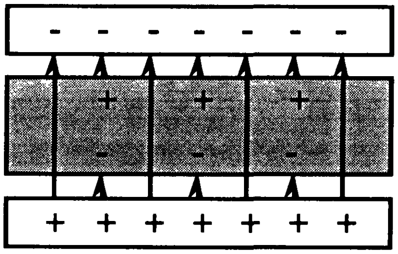

*Figure 5.4: Electric field reduction due to dielectric.*

For a linear dielectric material, the attenuation of the total electric field, $\vec{E}$, is given by

$$\vec{E} = \frac{1}{\kappa}\vec{E}_{free}. \qquad (5\text{-}5)$$

where $\kappa$ is the dielectric constant of the insulation, a dimensionless number, and $\vec{E}_{free}$ is the electric field of the parallel plates in the absence of dielectric insulation. Dielectric constants are always greater than or equal to one. The limiting values are $\kappa = 1$ for a vacuum and $\kappa = \infty$ for a metal. Table 5.1 lists the dielectric constants of several polymers (Tensolite, 1974; Union Carbide DFD-6005 Natural Data Sheet; DuPont FEP 4100 Data Sheet; DuPont PFA 40 HP Data Sheet).

*Table 5.1: Dielectric constants of various materials at 20°C and 1 atm.*

| *Material* | *Dielectric Constant* |
|---|---|
| Vacuum | 1.0 |
| Air | 1.00055 |
| DuPont FEP 4100 | 2.02 |
| DuPont PFA 440 HP | 2.03 |
| Union Carbide DFD-6005 PE-LD | 2.28 |
| Polypropylene | 2.24 |
| Polyethylene | 2.3 |
| Polycarbonate | 2.96 |
| Polyimide | 3.0-3.5 |
| Polysulfone | 3.13 |
| Polyvinyl chloride | 4.5-5.8 |
| Nylon | 4.5 |
| Polyurethane | 6.7-7.5 |

Gauss' Law for a dielectric configuration can be expressed as

$$\varepsilon_o \oint \vec{E} \cdot d\vec{S} = Q_{total} = Q_{bound} + Q_{free}, \tag{5-6}$$

where $d\vec{S}$ is the infinitesimal flux area of the electric field. This form of the equation is not immediately useful since $Q_{bound}$ depends on the degree of polarization of the dielectric and is not usually known beforehand. Therefore, Gauss' Law is traditionally rewritten so that electric field depends only upon the free charge. To enable this modification, it is assumed that the conductors, distribution of free charge on the conductors, and the dielectrics have sufficient symmetry so that Gauss' Law enables calculation of the electric field. As a starting point, assume that there is no dielectric material present. Gauss' Law for this situation is

$$\varepsilon_o \oint \vec{E}_{free} \cdot d\vec{S} = Q_{free}. \tag{5-7}$$

Next, a dielectric material is inserted, keeping the amount of free charges on the conductors constant. It is expected that the dielectric would perturb the electric field since the free charges on the conductors would interact with the bound charges on the dielectric. However, invoking the symmetry assumption, the dielectric cannot alter the distribution of free charges and the orientation of electric field lines. Substituting equation (5-5) into equation (5-7) yields Gauss' Law in dielectrics:

$$\varepsilon_o \oint \kappa \vec{E} \cdot d\vec{S} = Q_{free}. \tag{5-8}$$

A more detailed analysis will reveal that the symmetry assumption can be relaxed and equation (5-8), in fact, is valid for conductors and dielectrics of arbitrary shape. Equation (5-8) does require a linear dielectric material, however.

For the case of the parallel plate capacitor completely insulated by the dielectric in Figure 5.2, the integration in equation (5-8) becomes trivial.

$$E = \frac{Q_{free}}{\varepsilon_o \kappa A}. \tag{5-9}$$

The potential difference between the plates is found by line integration of the electric field.

$$\Delta V = \int \vec{E} \cdot d\vec{l}, \tag{5-10}$$

where $d\overset{\vee}{l}$ is the infinitesimal length along the path connecting the endpoints where the potential difference is being evaluated.

$$\Delta V = \frac{Q_{free} d}{\varepsilon_o \kappa A}. \tag{5-11}$$

Rearranging terms in the equation (5-11) reveals the capacitance.

$$C = \frac{Q}{\Delta V} = \frac{\varepsilon_o A}{d}\kappa. \tag{5-12}$$

Hence, the presence of the dielectric increases the capacitance of the system by a factor of $\kappa$ in comparison with the no dielectric parallel plate capacitor.

To understand the impact of microcellular foaming on the dielectric behavior of the coaxial cable, the simple of case of a parallel plate with dielectric insulation not completely filling the space between the plates (hereafter called *partially-filled capacitor*), as shown in Figure 5.5, will be analyzed. The results of the analysis will be used to establish a qualitative analogy between the partially-filled capacitor and the foam-coated coaxial cable.

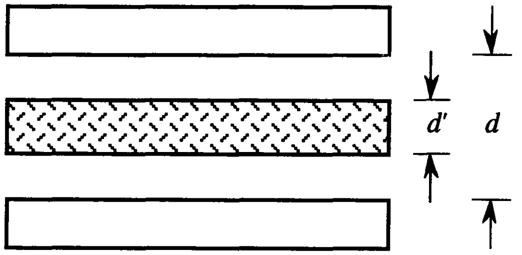

*Figure 5.5: Dielectric insulation which does not completely fill the region between the plates.*

As shown in Figure 5.5, a path of length $d - d'$ lies in the vacuum while a path of length $d'$ lies in the dielectric. Using equation (5-10), the potential difference between the plates is expressed as

$$\Delta V = E_{free}(d - d') + \frac{1}{\kappa} E_{free} d'. \tag{5-13}$$

$$\Delta V = \left[1 - \left(1 - \frac{1}{\kappa}\right)\frac{d'}{d}\right]\Delta V_o. \tag{5-14}$$

where $\Delta V_o$ is the potential difference in the absence of the dielectric insulation. Therefore, the capacitance is

$$C = \frac{C_o}{1-\left(1-\frac{1}{\kappa}\right)\frac{d'}{d}}. \tag{5-15}$$

where $C_o$ is the parallel plate capacitance in the absence of dielectric insulation. Substituting for $C_o$ yields

$$C = \frac{\varepsilon_o A/d}{1-\left(1-\frac{1}{\kappa}\right)\frac{d'}{d}}. \tag{5-16}$$

For the case $d' = d$, the arrangement resembles a completely insulated parallel plate capacitor and equation (5-16) reduces to $C = \kappa\varepsilon_o A / d$. The uninsulated parallel plate capacitor is captured by the case $d' = 0$ and equation (5-16) collapses to $C = \varepsilon_o A / d$. Both expressions are in accordance with previously derived expressions.

Equation (5-16) is presented graphically in Figure 5.6. For the sake of presentation, a dielectric constant of 2 is assumed. The graph indicates that as less dielectric material is present in the parallel plate construction, i.e., $d' / d$ diminishes, the normalized capacitance of the systems decreases. As discussed previously, the endpoints of the graph correspond to the extreme cases of a no dielectric capacitor and a completely-filled capacitor. Hence, in comparison with the completely-filled capacitor, less dielectric, and therefore, more air gap reduces capacitance. Since the capacitance has decreased, it is commonly stated that the dielectric constant has decreased. It is important to realize that the dielectric constant of the insulation material itself remains the same; however, the effective dielectric constant of the composite insulation-air system has decreased. This concept is clarified in Figure 5.7 which pictorially summarizes the comparisons being made. The foam-coated coaxial cable is likened to the partially-filled capacitor because it possesses less insulating material and more air gap than the corresponding completely-filled cases. The effective dielectric constant of the foam-coated coaxial cable system will be smaller than the measured dielectric constant of the completely-filled coaxial cable. For a given coating thickness on the wire, microcellular extrusion alters the configuration of the insulation into a cellular structure with gas voids and hence reduces the amount of polymeric material used. These factors account for the decrease in dielectric constant of the composite polymer/gas void system.

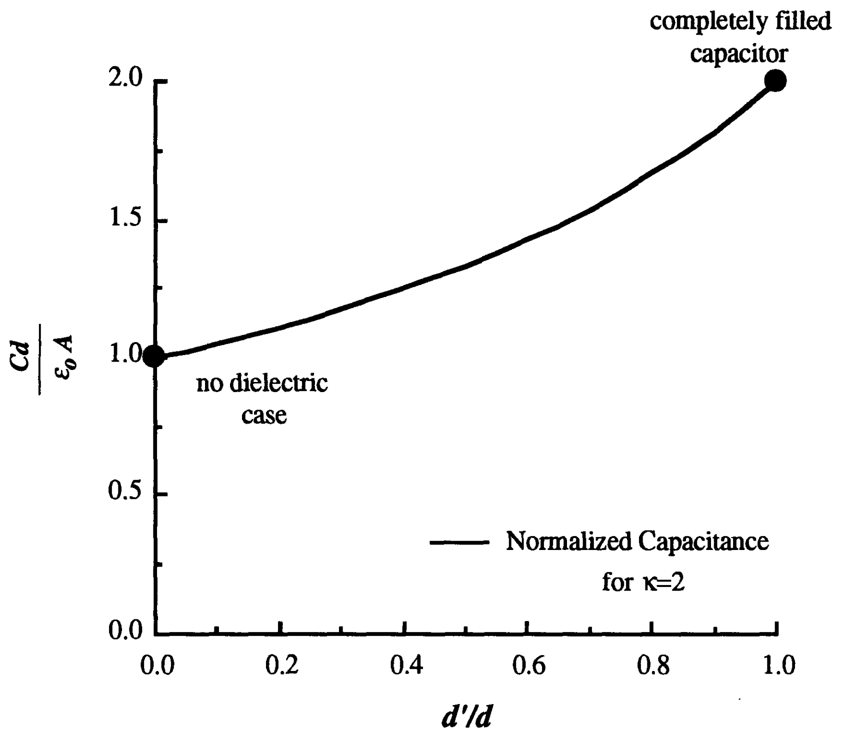

*Figure 5.6: Capacitance of a parallel plate capacitor with varying dielectric thickness.*

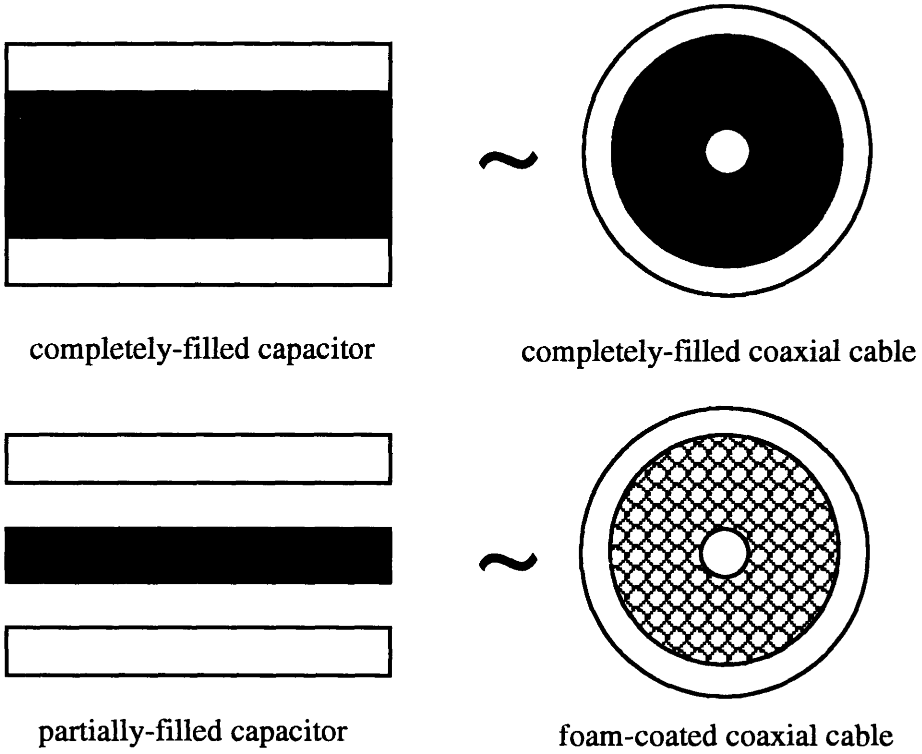

*Figure 5.7: Coaxial cable/parallel plate capacitor analogy.*

The final portion of this section analyzes the capacitance of a coaxial cable of length $L$ and dielectric construction given by Figure 5.8.

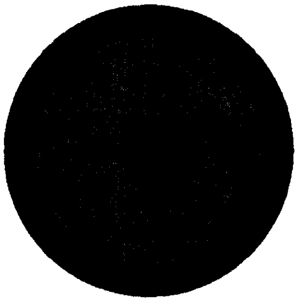

*Figure 5.8: Coaxial cable geometry used in capacitance analysis.*

Applying Gauss' Law in dielectrics to the coaxial cable geometry yields

$$E = \frac{1}{2\pi\varepsilon_o \kappa L}\frac{Q_{free}}{r}. \tag{5-17}$$

Substituting the electric field into equation (5-10), the potential difference is expressed as

$$\Delta V = \int_{r_{bw}}^{r_{cw}} \frac{1}{2\pi\varepsilon_o \kappa L}\frac{Q_{free}}{r}dr. \tag{5-18}$$

$$\Delta V = \frac{Q_{free}}{2\pi\varepsilon_o \kappa L}\ln\left(\frac{r_{cw}}{r_{bw}}\right). \tag{5-19}$$

As before, the subscripts *bw* and *cw* represent bare wire and coated wire, respectively. Hence, the capacitance per unit length is given by

$$c = \frac{C}{L} = \frac{Q}{L\Delta V} = \frac{2\pi\varepsilon_o}{\ln\left(r_{cw}/r_{bw}\right)}\kappa. \tag{5-20}$$

This theoretical result will be modified in the subsequent section based on empirical observation.

## 5.2 Coaxial Cable Performance

Based on several decades of wire coating experience, several empirical relations have been developed to characterize the electrical behavior of coaxial cables. This section briefly covers some of these key relations (Tensolite, 1974). The dielectric constant which appears in these formulas should be taken as the effective dielectric constant of the coaxial cable system.

The rate at which data can be transmitted through a coaxial cable is inversely proportional to the dielectric constant of the insulation. Expressed as a percentage of the speed of light, the propagation velocity of electrical energy in a coaxial cable compared with the velocity in air is given by

$$V_{prop}(\%) = \frac{100}{\sqrt{\kappa}}. \tag{5-21}$$

Thus, reductions in dielectric constant yield faster transmission speeds. The improved dielectric behavior afforded by microcellular processing will enable faster data transfer.

Capacitance is the property of an electrical system which allows storage of electrostatic energy. Expressed in units of picofarads/foot [pF/ft], the capacitance has been experimentally determined to equal

$$C = \frac{7.359}{\log\left(\frac{d_{cw}+a}{fd_{bw}}\right)}\kappa, \tag{5-22}$$

where $a$ is the shield correction factor [in] which is equal to one half the single end shield wire diameter and $f$ is the stranded correction factor (refer to Table 5.2). Stranded conductors have a lower capacitance than the solid conductor.

*Table 5.2: Stranding correction factors.*

| *Stranding* | *f* |
|---|---|
| Solid | 1.00 |
| 7 Strand | 0.93 |
| 19 Strand | 0.97 |
| 37 Strand | 0.98 |

The impedance of a cable in ohms [Ω] is given by the following relation:

$$Z_o = \frac{138}{\sqrt{\kappa}}\log\left(\frac{d_{cw}+a}{fd_{bw}}\right). \tag{5-23}$$

Stranded conductors have a higher impedance than the solid conductor.

Attenuation, $\Gamma$ [decibels/ft], is the percentage loss of electrical power per unit length of the cable. It is a combination of losses in the conductor, dielectric insulation, and radiation from the cable.

$$\Gamma = 4.34\frac{R_t}{Z_o} + 2.75\lambda F\sqrt{\kappa}. \tag{5-24}$$

where $F$ is the frequency [MHz], $\lambda$ is the power factor (listed in Table 5.3 for several polymers) (Times Wire and Cable, 1972), and $R_t$ is the total line resistance [ohms/mft]. For a copper coaxial line,

$$R_t = 0.1\left(\frac{1}{d_{bw}} + \frac{1}{d_{cw}}\right)\sqrt{F}. \tag{5-25}$$

*Table 5.3: Power factors.*

| *Polymer* | $\lambda$ |
|---|---|
| Polyethylene | 0.0003 |
| Nylon | 0.030-0.040 |
| Silicone Rubber | 0.007-0.016 |
| FEP | 0.0003 |
| Polyimide | 0.002-0.003 |

The time delay, $t_d$, of a cable expressed in nanoseconds per feet [nsec/ft] is given by

$$t_d = 1.016\sqrt{\kappa}. \tag{5-26}$$

Thus, lowering the effective dielectric constant of the wire insulation reduces capacitance, time delay, and attenuation and increases the propagation velocity of electrical energy.

# CHAPTER 6

# EXTRUSION EXPERIMENTAL RESULTS

## 6.0 Introduction

Before discussing the extrusion studies, a brief overview of the polyolefins used in the experiments is provided. Experimentation encompassed tube extrusion with a conventional tube die as well as a wire coating die.

## 6.1 Polyolefins

### 6.1.1 Low Density Polyethylene (PE-LD)

Low density polyethylene is a semicrystalline thermoplastic polymer manufactured by high-pressure free radical polymerization of ethylene, a colorless hydrocarbon. An ethylene building block is shown in Figure 6.1. PE-LD has a milky white, opaque appearance and the feel of wax. It was first commercialized in the 1940's for wire coating insulation because of its clarity, chemical inertness, flexibility, sealibility, and ease of processing (Juran, 1990).

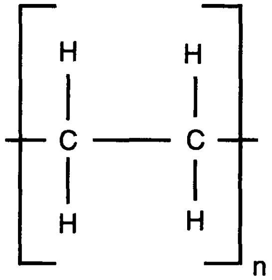

$$\left[ -CH_2-CH_2- \right]_n$$

*Figure 6.1: Ethylene monomer unit.*

Since PE-LD is produced at pressures exceeding 10,000 psi (Rubin, 1990), the polymer has a branched structure which improves its extrusion characteristics. The molecular arrangement can be tailored for different applications by varying three major parameters: molecular weight, crystallinity, and molecular weight distribution (Juran, 1990). Molecular weight refers to the average size of all the molecular chains which comprise the polymer. Industry has established a quantity called the melt flow index as a measure of the molecular weight. This index refers to the mass of polymer that is extruded through a given orifice at a certain temperature and pressure for a given time. The melt index is inversely proportional to the molecular weight. Increasing the molecular weight of PE-LD results in increased strength properties but decreased flow and drawdown ability. Increasing crystallinity increases stiffness, chemical resistance, and tensile strength but decreases impact resistance and tear strength. PE-LD normally has a crystallinity of 30-40%. Finally, the molecular weight distribution (MWD) is defined as the ratio of the weight-average molecular weight to the number-average molecular weight (Juran, 1990). Polymers with broader distributions have better flow characteristics than those with narrow distributions. The melting temperature of PE-LD ranges from 110-125°C (Whelan, 1988).

Polyethylene is the most widely used thermoplastic and is available in numerous forms. It is estimated that worldwide production will grow from 30 million tons in 1990 to 40 million tons in 1996 (Graff, 1993). The U.S. alone has a total annual capacity of approximately 6 billion pounds of PE-LD (Juran, 1990). PE-LD is compatible with blown film and cast film extrusion, extrusion coating, injection molding, and blow molding. It is commonly used in the packaging of food items as well as coatings for wire and cable and paper products.

The specific PE-LD grade used in this study was Union Carbide DFD-6005 Natural. Designed specifically for wire and cable coating, the resin contains a non-staining antioxidant. DFD-6005 Natural has a density of 0.92 g/cm$^3$ at 23°C and a melt index of 0.20 g/10 min. The dielectric constant at 1 MHz is 2.28 and the tensile strength is 2,200 psi (15.2 MPa). Union Carbide recommends extrusion temperatures ranging from 375-425°F.

### 6.1.2 Polypropylene (PP)

Polypropylene is a semicrystalline thermoplastic polymer processed by polymerizing propylene monomer units, shown in Figure 6.2. A typical polypropylene macromolecule consists of 10,000-20,000 such units and its average molecular weight ranges between 200,000-600,000 (Juran, 1990). The material has a translucent ivory white color and feels hard and waxy (Whelan and Dunning, 1988). If the methyl ($CH_3$) groups are all on the same side of an unbranched chain, the structure is known as isotactic polypropylene. If the methyl groups alternate on either side of the chain, the structure is syndiotactic. Random positioning of the methyl groups results in an atactic structure (Verein, 1979). The molecular arrangement of the methyl groups has a dramatic impact on properties such as stiffness and melting point.

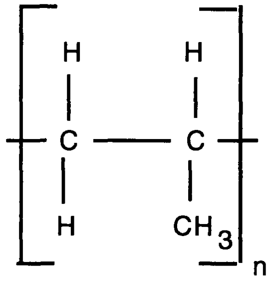

*Figure 6.2: Propylene monomer unit.*

Polypropylene was first produced commercially in 1957 and is the largest growing thermoplastic due to its compatibility with numerous processing techniques such as extrusion, blown and cast film, blow molding, injection molding, and thermoforming (Juran, 1990). More than 8.5 billion pounds of PP were produced in the U.S. in 1992, bringing the worldwide annual production total to 31 billion pounds (Graff, 1993). The breakdown of usage for domestically produced PP that year includes 3 billion pounds for extruded sheets, films, fibers, and filaments and 2.2 billion pounds for injection molded parts for appliances, medical equipment, and packaging, etc. More than a billion pounds of the remaining output was exported (Graff, 1993).

Polypropylene is relatively resistant to most organic solvents as well as easy to recycle. It differs from PE structurally by having a methyl group in each monomer rather than just a hydrogen atom. This stiffens the chain and increases its melting point to roughly 165°C (Juran, 1990). The specific resin used in this research was Petrothene 1610-PF supplied by Quantum Chemical Corporation. It was chosen for its wire coating properties. The material contains antioxidants for thermal stability and long-term aging properties. Furthermore, it contains a metal deactivator to prevent degradation. The material has a mean molecular weight of 359,100, a mean number weight of 61,200, and a polydispersity of 5.9. The resin has a density of 0.897 g/cm$^3$, a melt flow rate of 2.24 g/10 min. The dielectric constant at 1 MHz is 2.28. Mechanical properties include a 3,200 psi yield strength and a 3,600 psi tensile strength. Quantum suggests processing temperatures in the range of 310-480°F (Quantum Data Sheet).

## 6.2 Extrusion Experimental Results

### 6.2.1 Tube Extrusion With Conventional Tube Die

Before introducing the added complexity of the crosshead and the accompanying wire coating components, system startup began with a conventional metric tube die having the following die lip dimensions: 22 mm (0.866 in) ID, 25 mm (0.984 in) OD, and therefore, a wall thickness of 1.5 mm (0.059 in). The tube die assembly was directly bolted to the gear pump outlet flange. During initial processing, many important observations were made regarding the operation of the extrusion system, particularly the carbon dioxide metering system.

As mentioned in chapter 4, cooling of the metering pump head is crucial for successful operation of the pump. If the pump head is too warm during operation, the liquid $CO_2$ can flash and cause vapor lock of the pump. Initially, water chilled to 46°F (8°C) was circulated through the pump head. With the high temperature valve in Figure 4.13 closed and the metering pump operating at its maximum of 1,900 rpm, the highest pumping pressure developed was only 3,000 psi, well below the 5,000 psi limit. After cooling the pump head with slightly colder 41°F (5°C) water, a 3,600 psi maximum pumping pressure was observed. Indeed, inadequate pump head cooling was the culprit. Therefore, rather than lowering the water temperature dangerously close to its freezing point, the entire liquefaction chamber and metering pump were placed in a small freezer. When the pump was operated at -17°F (-27°C) (coldest setting of freezer), the pump gear oil became highly viscous and the pump motor could only turn at 1,000 rpm. To reduce friction, the pump motor housing was removed and the motor shaft was lubricated with silicone spray (Permatex #116DA). This lubrication reduced the squeaking of the shaft. Finally, when the metering pump was operated at a warmer temperature of -8°F (-23°C), the normal setting of freezer, the maximum pumping pressure achieved was 4,600 psi. Pump inefficiencies and $CO_2$ compressibility can explain why the 5,000 psi maximum pumping pressure could not be attained.

During the foam extrusion procedure, $CO_2$ gas[§] was injected into the barrel by opening the high temperature valve after the barrel pressure had achieved steady state. The experimental results of this chapter will be explained using qualitative amounts of gas. Although the metering pump was designed to provide a precisely metered fluid flow, it was

---

[§] Although the carbon dioxide is in its supercritical region at the point of injection, the word *gas* is used for convenience.

not possible to ascertain the exact amount of gas injected into the barrel during the experiments for the following reasons. Due to the compressibility of the carbon dioxide, the efficiency of metering pump is lower than the theoretical limit. In practice, the metering pump efficiency as function of discharge pressure is experimentally determined by the manufacturer for a relatively incompressible fluid such as water. The pump efficiency for carbon dioxide can then be calculated based on thermodynamic changes of state. These calculations should provide a reasonable estimate of the metering rate. During operation however, the pump rpm readout constantly fluctuated, in some cases by as much as 150 rpm, and never settled down to a steady-state value. This behavior was also observed during room temperature diagnostic testing of the pump. The pump controller should, therefore, be retuned and recalibrated to minimize these fluctuations as well as to determine the actual amount of gas metering.

### Low Density Polyethylene Results

The PE-LD polymer melt was saturated with carbon dioxide at a pressure of 3,350 psi. The polymer/gas solution experienced a 3,000 psi drop at the gear pump teeth and exited through the tube die with a 15 $cm^3$/min flow rate. The extruder had a screw rpm of 23 for these operating conditions. The temperature of the melt was 376°F. The trials were performed with a medium gas concentration. As the melt emerged from the die lip, the crackling sounds of undissolved gas could be heard. The tube had a rough surface finish and became white as a result of foaming. Scanning electron micrographs of a fracture surface with the bubbles in the extrusion direction are presented in Figure 6.3. The view of the tube wall in Figure 6.3a reveals several undissolved gas clusters, confirming the crackling sounds described earlier. However, upon closer investigation, the micrographs at high magnification, Figures 6.3b and 6.3c, indicate that extremely small cells were, in fact, nucleated. The average cell size of the small cells which appeared in clusters was 0.4 μm and the corresponding cell density was $6.6\times10^{11}$ cells/$cm^3$. This result marks the very first time that submicron-sized cells have been nucleated in continuous microcellular processing. Previous work by Park (1993) and Baldwin (1994) produced cells sizes on the order of 5 μm. Since the micrographs in Figure 6.3 were taken in the extrusion direction, it is interesting to note that the cells remained spherical and undeformed. This indicates that the gear pump teeth have little to no effect on very small-sized cells.

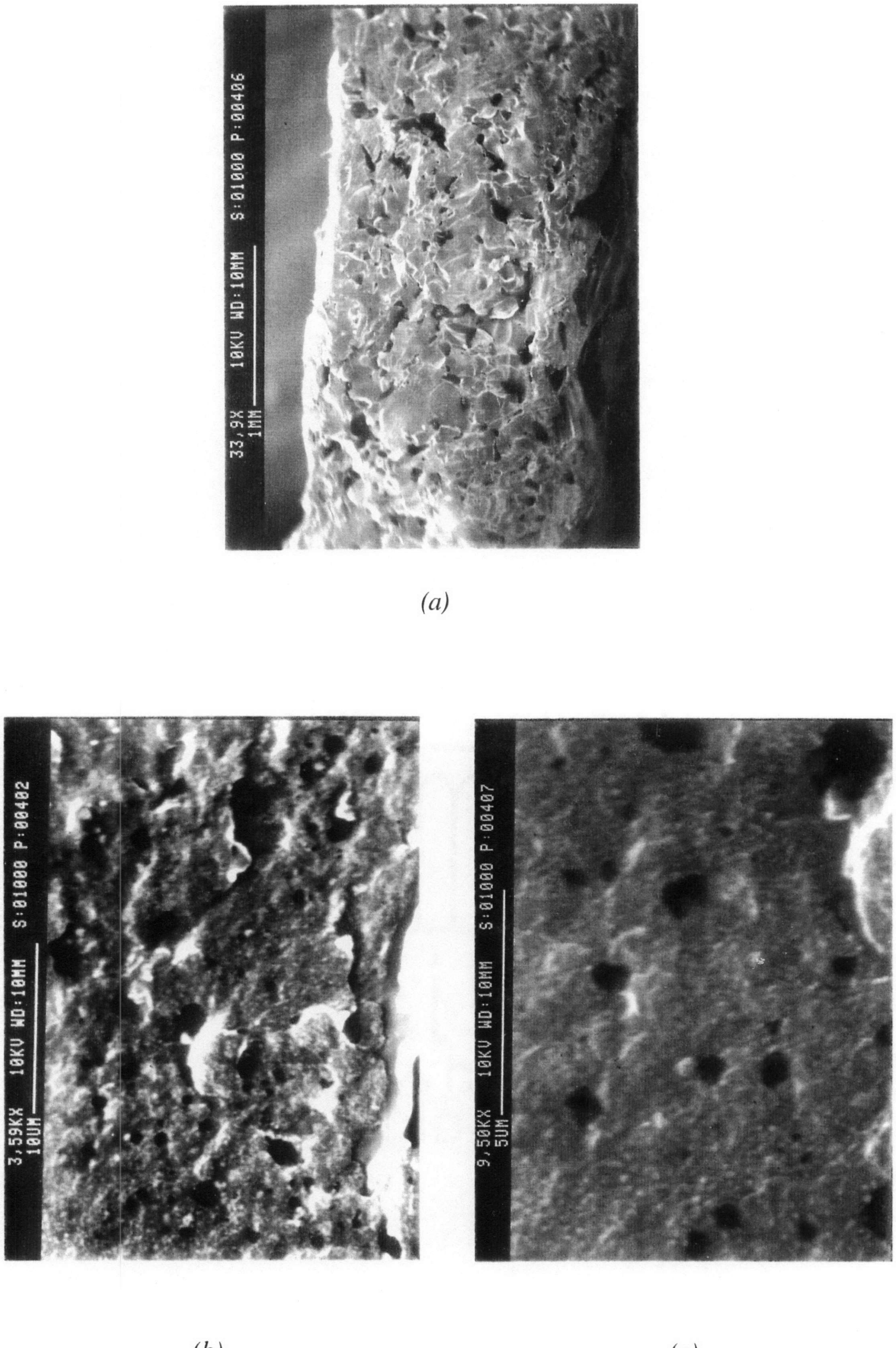

*(a)*

*(b)* *(c)*

*Figure 6.3: SEM micrographs of the PE-LD sample at various magnifications taken in the extrusion direction.*

A subsequent trial with the same conditions as the previous experiment was performed, except this time with more gas injection. The macro-view of the sample was similar to that of Figure 6.3a with clusters of undissolved gas. However, inspection at the submicron level perpendicular to the extrusion direction revealed a section of completely nucleated polymer, as shown in Figure 6.4. The average cell size in this cluster was 0.1 μm while the cell density was $1.5\times10^{14}$ cells/cm$^3$, making this region of the polymer a supermicrocellular foam.

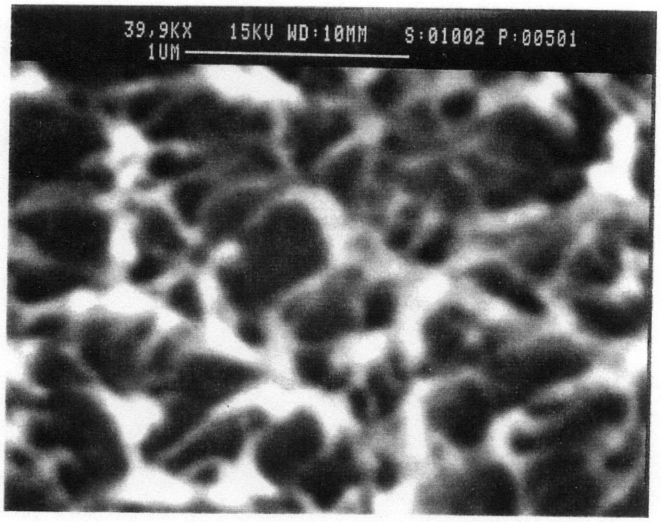

*Figure 6.4: PE-LD fracture surface perpendicular to the extrusion direction.*

Many other trials of varying pressure drop, screw speed, and flow rate were tested. Since obtaining a pure single-phase solution was not possible, due in part to the limited maximum screw rpm of 28, SEM micrographs of the samples were very similar to those above and could not be used to make conclusions about the effects of various microcellular processing parameters on cell morphology. Once the system is fitted with a new gearbox/motor that will enable higher screw rpms, the processing window can be enlarged so as to create single-phase polymer/gas solutions as well as to nucleate these flows. Higher screw rpms will enhance mixing as well as increase barrel pressures.

## Polypropylene Results

With the same tube die, foaming experiments were performed with Petrothene 1610-PF polypropylene. The propylene melt at 432°F was saturated with carbon dioxide gas at 4,000 psi and the pressure drop at the gear pump was 3,800 psi. The polymer/gas solution had a volumetric flow rate of 12 $cm^3/min$. Several magnifications of the sample fractured in the extrusion direction are presented in Figure 6.5. Much like the PE-LD samples, there are regions of large undissolved gas pockets in this sample. When magnified several thousand times, however, the micrographs in Figures 6.5b and 6.5c present surfaces having supermicrocellular cells. These small cells were distributed throughout the whole sample. Figure 6.6 provides views perpendicular to the extrusion direction. The average cell size of the small cells was 0.3 μm and the cell density was $9.5\times10^{12}$ $cells/cm^3$. Once again, the cells were not influenced by possible memory effects of the gear pump or shear in the polymer flow as it passed through the die.

### 6.2.2 Tube Extrusion With Wire Coating Die

The final phase of experimentation was performed using the crosshead set up for wire coating tube extrusion (guide 0.022 in ID, 0.065 in OD; die 0.089 in ID). The results of the wire coating die are similar to those of the metric tube die.

After the experiments in the previous section were performed, a gas leak was discovered at the injection stem assembly. The metering system was partially disassembled and the original Viton O-ring was replaced with a solid fluoropolymer PTFE O-ring. PTFE has an operating temperature rating 100°F higher than Viton, an elastomeric fluoropolymer, and also absorbs less gas. The best solution to the leakage problem, however, is to construct a gas injection stem from one piece rather than assembling three pieces which mate so as to create a seal. Another option includes modifying the current O-ring groove to accommodate a metal C-ring. Although metal C-rings can seal at temperatures as high as 1,800°F and will not suffer from gas sorption, their use is discouraged in the current setup because compression of metal seals during installation requires high torques which are difficult to achieve given the space constraints imposed by the polycarbonate safety housing around the extruder. Furthermore, rotation of the injection assembly during the torquing procedure can remove the thin silver plating of the metal seal.

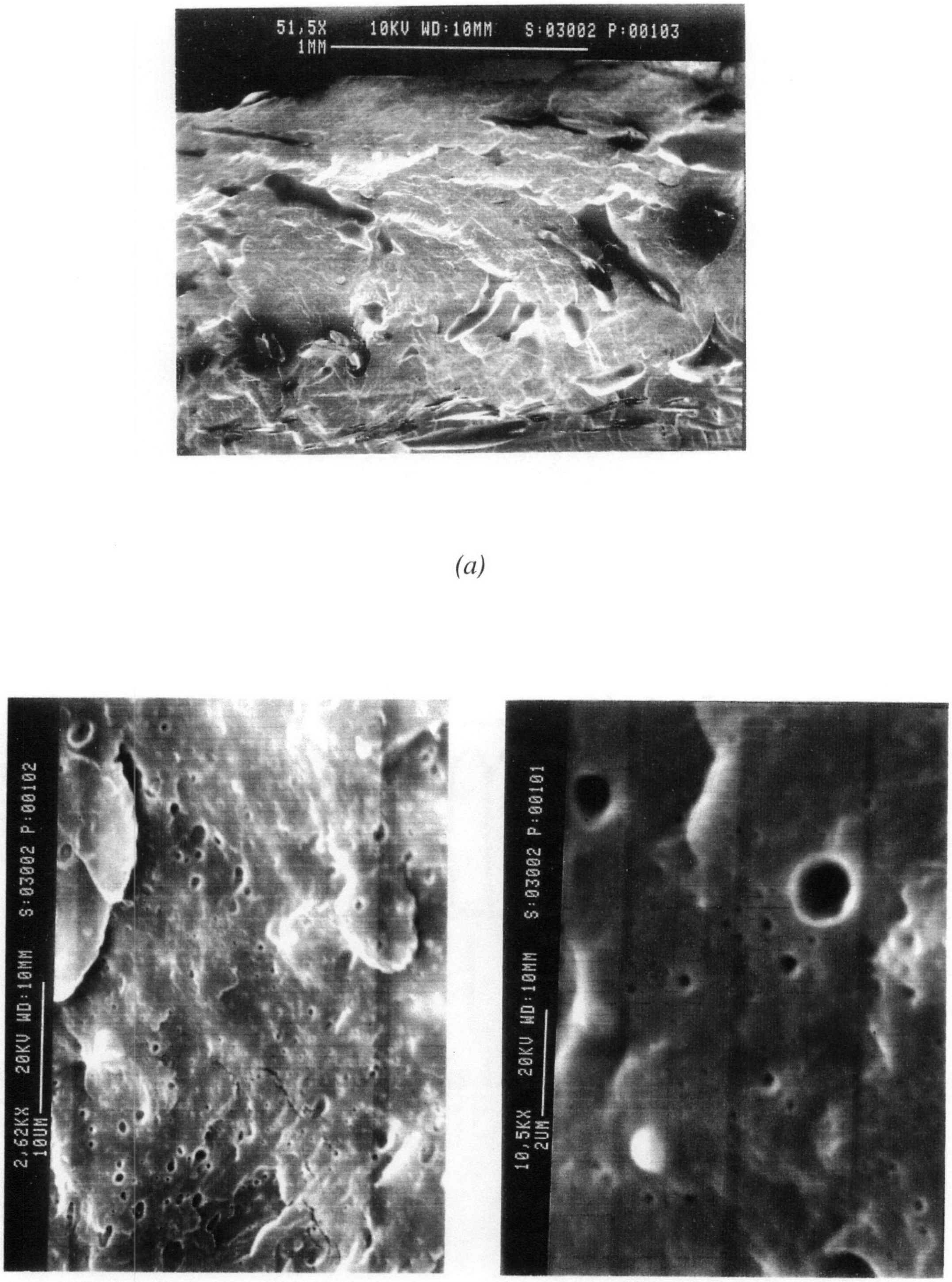

*(a)*

*(b)* *(c)*

*Figure 6.5: Various magnifications of the PP fracture surface taken in the extrusion direction.*

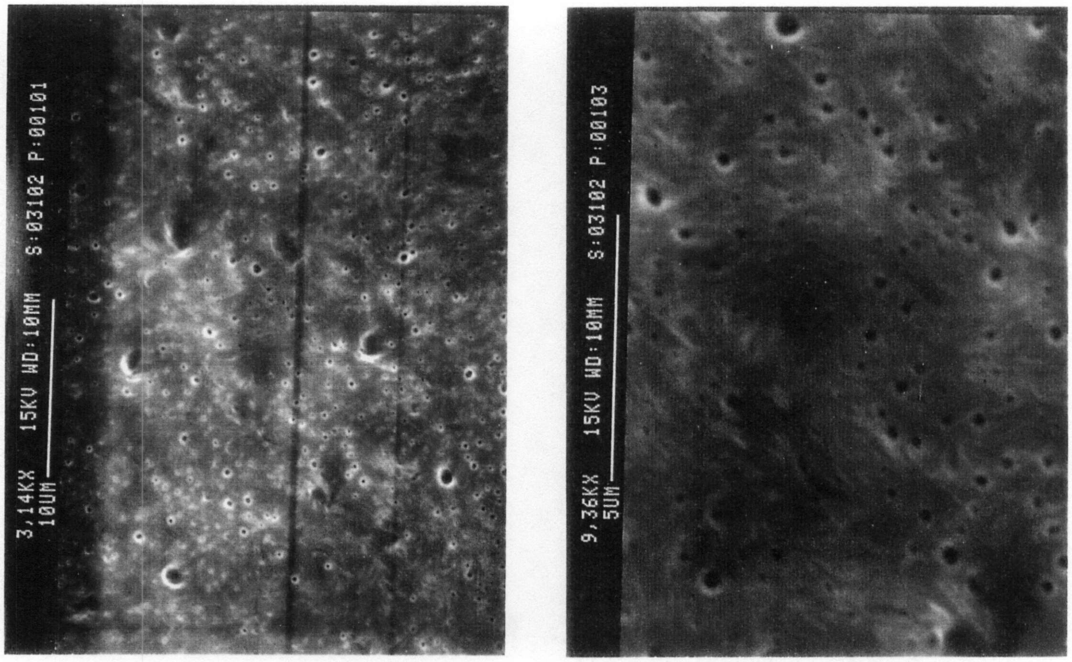

*(a)* *(b)*

*Figure 6.6: PP fracture surface perpendicular to the extrusion direction.*

Based on the encouraging results of the previous section, experimentation continued with polypropylene. The polymer melt was saturated with medium gas injection at 438°F and 4,300 psi. A pressure drop of 3,825 psi occurred at the gear pump and the nucleated solution exited the gear pump at 10 $cm^3$/min. Several views of the fracture surface perpendicular to the extrusion direction are presented in Figure 6.7. Figure 6.7a reveals undissolved gas bubbles starting at 30 $\mu$m in diameter. Higher magnification (Figure 6.7b) uncovers the multitude of submicron-sized cells. The average size of the small cells was approximately 0.2 $\mu$m and the corresponding cell density was $2.5 \times 10^{13}$ cells/$cm^3$. The fracture surfaces in the extrusion direction clearly demonstrate shear elongation of the undissolved gas. The numerous “streaks” of gas in the tube cross section seen in Figure 6.8a are more easily discernible upon higher magnification in Figure 6.8b. A variety of other combinations of pressure drop and flow rate were examined, but since obtaining a single-phase solution was the underlying obstacle in obtaining optimum processing conditions, specific conclusions about microcellular processing parameters could not be made.

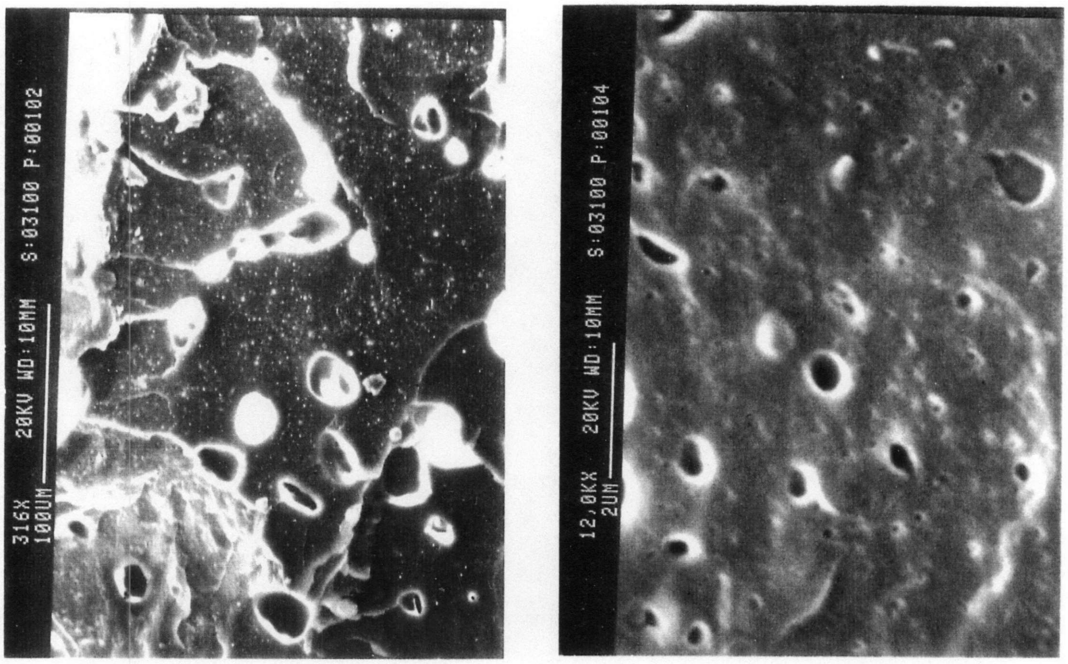

*(a)* *(b)*

*Figure 6.7: Micrographs of the PP sample extruded through the wire coating die. These surfaces were oriented perpendicular to the extrusion direction.*

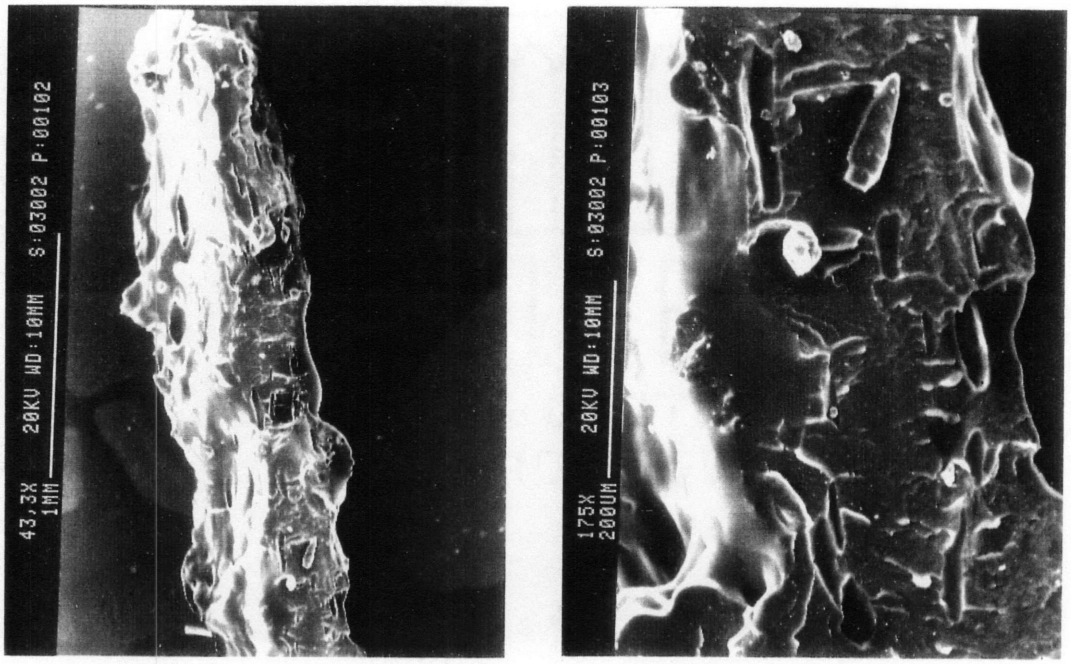

*(a)* *(b)*

*Figure 6.8: PP fracture surfaces in the extrusion direction reveal stretching of the undissolved gas bubbles.*

All of the experiments described in this chapter thus far employed gear pump nucleation. To allow more time for diffusion of gas into the polymer, an attempt was made at nucleating the flow at the crosshead die itself, rather than the gear pump. The gear pump outlet pressure is a function of the gear pump flow rate and the crosshead die/guide resistance. Given the fixed resistance of the wire coating die described earlier, the idea was to increase the gear pump flow rate high enough to generate a high gear pump outlet pressure with which to nucleate the polymer/gas solution right at the die lip. The system was operated by first setting the flow rate and observing the gear pump outlet pressure. Once steady state was reached, the gear pump inlet pressure was set roughly equal to the outlet pressure. Therefore, there was a negligible pressure drop across the gear pump. In effect, the gear pump in this mode of operation was only being used to meter a constant flow rate. Given the limitations of the screw rpm, the maximum stable condition that could be reached was a gear pump discharge pressure of only 860 psi at a flow rate of 20 $cm^3$/min, a typical polyolefin wire coating flow rate. This low discharge pressure was not sufficient for microcellular processing.

## 6.3 Conclusions

Preliminary characterization of the microcellular extrusion system confirmed the use of a gear pump to nucleate microcellular foam. In fact, for the various polyolefins tested, cell morphologies of the nucleated cell clusters lied in the supermicrocellular range, surpassing the smallest cell sizes achieved through nozzle nucleation. At such small length scales, potential memory effects of the gear pump teeth had no observed impact on the cell microstructure. Furthermore, the spherical voids remained unsheared even after passing through the narrow flow restrictions of fine wire coating dies. These observations were confirmed by scanning electron microscopy both in the extrusion direction and perpendicular to the extrusion direction. Although these findings are very encouraging, additional work, which is presented in the following chapter, is necessary to perfect the system. In the regions where gas had dissolved into the polymer, the gear pump successfully nucleated voids. Since a pure single-phase solution could not be achieved due to system limitations, large gas bubbles were also present in the samples. Obtaining a single-phase polymer/gas solution will be the primary thrust of future system modifications since it is a key requirement for microcellular extrusion.

# *CHAPTER 7*
# *CONCLUSIONS*

## 7.0 Introduction

The goals of the research are revisited:

- Assess the batch foaming characteristics of DuPont FEP 4100 and PFA 440 HP
- Design and construct a scaled-up microcellular extrusion system and evaluate its microcellular processing capabilities for wire coating

The following sections summarize the major results of the thesis and finally conclude with recommendations for future work. Comprehensive treatment of the results can, of course, be found in chapters three and six.

## 7.1 Conclusions

### 7.1.1 Batch Processing Conclusions

The major success of the batch processing experimentation was the creation of microcellular Teflon. As a starting point, the weight gain characteristics of FEP 4100 and PFA 440 HP were investigated. Both polymers exhibited induced crystallinity as a result of $CO_2$ gas sorption. The maximum weight gain for FEP was 3.43% after 5 hours of saturation while the maximum weight gain for PFA was 3.15% after 4 hours of saturation.

Extensive foaming trials revealed that FEP has a narrow microcellular batch processing window of 10°C. The optimum sample had an average cell size of 6.1 μm with a cell density of $8.5\times10^9$ cells/cm$^3$. This cell morphology was produced using a saturation pressure of 5,500 psi, a saturation temperature of 225°C, and a saturation time of 4 hours. The sample became opaque and had a smooth surface finish. The peculiar anomaly of intermittent large cells distributed among micron-sized cells was observed at saturation temperatures above 235°C.

FEP coated wires were also batch processed to determine the effects of microcellular processing on electrical performance. The preliminary results of these tests demonstrated decreases in dielectric constant as high as 31%. Thus, the basic motivating factor of improved electrical performance was realized, indicating that microcellular processing will have a tremendous impact on the wire coating industry provided that a reliable wire coating extrusion process can be developed.

Batch processing of PFA resulted in cell morphologies very close to microcellular morphologies. The full range of experimental conditions could not be tested due to safety limitations of the experimental apparatus. It appears very likely that microcellular PFA can be produced if saturation pressures greater than 3,500 psi and saturation temperatures in the neighborhood of 288°C are used. The best sample produced had an average cell size of approximately 30 μm.

### 7.1.2 Extrusion Processing Conclusions

Drawing upon lessons learned from previous prototype microcellular extrusion systems (Park, 1993; Baldwin, 1994), an improved system which incorporated a gear pump as the nucleation device was proposed (Herrmann, 1994). Based on the proposal, this research implemented the gear pump concept into a manufacturing-scale wire coating extrusion system. After modifying the system for microcellular processing, preliminary experimentation demonstrated that a gear pump can, indeed, nucleate microcellular foam. For Union Carbide DFD-6005 Natural low density polyethylene and Quantum Petrothene 1610-PF polypropylene, the specific polyolefins tested, supermicrocellular cell morphologies were obtained in regions where sufficient gas had dissolved into the polymer. This marked the first appearance of submicron-sized cells in a continuous microcellular process. As evidenced by SEM micrographs of sample fracture surfaces both in the extrusion direction and perpendicular to the extrusion direction, these extremely small cells were neither unaffected by potential memory effects of the gear pump teeth nor shear occurring in the flow passages of the conventional tube dies.

## 7.2 Recommendations for Future Work

### 7.2.1 Batch Processing Recommendations

There are a host of possible topics to pursue for future research. This work realized microcellular fluoropolymer foam by identifying the batch processing window for FEP.

Additional work is necessary to fully characterize the behavior of PFA. Due to the safety considerations associated with testing PFA at elevated temperatures, saturation pressures exceeding 3,500 psi were not tested. Higher saturation pressures result in a greater dissolution of gas into the polymer and, therefore, increase the number of nucleation sites. In fact, very high pressure testing is recommended for all polymers, not just fluoropolymers, to assess the feasibility of producing ultramicrocellular foams having cell diameters on the order of 0.01 μm. Foams with such extremely small cells may exhibit transparency and offer attractive electrical properties. Commercial pressure vessels rated to 100,000 psi are readily available (High Pressure Equipment Company) and can be custom-designed for microcellular processing requirements.

Section 3.3.2 included the results of foaming wires already coated with fluoropolymeric insulation. The results revealed that the wire samples had different morphologies compared with planar samples processed at the same conditions. Further investigation may shed light on this phenomenon. In addition, batch processing of longer wire lengths can be investigated to assess the possibility of foaming entire spools of wire.

Theoretical work should complement the aforementioned experimental work. An analytical model which predicts the effective dielectric constant of a polymer foam given a specific cell morphology would be very useful. Once the extrusion process has been developed to process microcellular foam-coated wires which can be tested on-line for dielectric constant, capacitance, etc., the predictive power of the model can be verified.

### 7.2.2 Extrusion Processing Recommendations

Despite the successes of gear pump nucleation, additional work is required before electrical wires can be reliably coated with microcellular foam. The primary obstacle in creating a honeycomb structure in the extruded samples was the inability to create a single-phase solution of polymer and gas. Since the gas had not fully dissolved into the polymer, the number of nucleation sites was very small. Once a fully saturated single-phase solution is nucleated, however, cell morphologies consisting of very small cell sizes and very large cell densities can be achieved. The maximum screw rpm of 28 in the current setup was not sufficient for shearing the injected gas into smaller bubbles and mixing them into solution. Higher screw rpms not only improve mixing but also increase pressures in the barrel, which would make for better saturation conditions and faster diffusion rates. The high flow rates needed to produce thick-walled shapes will definitely require much faster screw rpms in order to generate high gear pump inlet pressures. To ensure a single-phase solution, static mixers and diffusion chambers can be added to the system.

Although the gas metering system injected carbon dioxide into the extruder barrel, several issues should be resolved before continuing with experimentation. The metering pump controller should be retuned to minimize fluctuations of the pump rpm readout. The pump should also be experimentally calibrated to determine the actual amount of gas being injected into the extruder. It is extremely important to know the level saturation taking place if microcellular processing conclusions are to be drawn from experimentation. Finally, the gas injection stem should be redesigned from one piece rather than three to reduce the possibility of carbon dioxide leaks in the system.

It appears very likely that conventional polymer processing dies can be used to shape gear pump nucleated polymer flows because even the shear rates induced by the particular conventional tube dies and wire coating dies tested did not alter the shape of the nucleated voids. This hypothesis will be confirmed when future researchers nucleate a single-phase polymer/gas solution to create a polymer flow having very high cell densities and very small cell sizes and then attempt to shape the flow into useful product geometries. The penetration of microcellular extrusion technology into commercial markets will be extremely rapid if conventional dies can be used and no new dies designed specifically for microcellular processing are required.

Currently, little work has been done to characterize the rheology of polymer/gas solutions. The viscosity functions of gas-saturated polymers are indispensable in designing microcellular processing *systems*, from extruder sizing and screw design, to the details of the die profile. Herrmann (1995) suggests the concept of polymer/gas solution rheometer (PGSR) for obtaining this urgently needed rheological data. Work should be done to gain more insight polymer/gas solution flow behavior.

Once sufficient experience has been obtained with coating wires with polyolefins, the entire system can be upgraded with nickel-based gear pumps and flanges for fluoropolymer extrusion. Fluoropolymer processing introduces several material handling concerns that should be addressed once polyolefin extrusion has been understood. Microcellular fluoropolymer extrusion is, nevertheless, very important. Tremendous savings in material costs as well as improvements in product quality are possible with microcellular processing technology.

# *REFERENCES*

Alternative Fluorocarbons Environmental Acceptability Study (AFEAS), 1993, "Production, Sales, and Atmospheric Release of Fluorocarbons through 1992," SPA-AFEAS, Inc., The West Tower Suite 400, 1333 H Street NW, Washington, DC 20005.

Baldwin, D.F., Suh, N.P., and Shimbo, M., 1992, "Gas Dissolution and Crystallization in Microcellular Thermoplastic Polyesters," *Cellular Polymers*, MD-Vol. 38, ASME, pp. 109-127.

Baldwin, D.F., Tate, D.E., Park, C.B., Cha S.W., and Suh N.P., 1994a, "Microcellular Plastics Processing Technology (1)," *Seikei Kakou (Journal of the Japan Society of Polymer Processing)*, Vol 6., No. 3, pp. 187-194.

Baldwin, D.F., Tate, D.E., Park, C.B., Cha S.W., and Suh N.P., 1994b, "Microcellular Plastics Processing Technology (2)," *Seikei Kakou (Journal of the Japan Society of Polymer Processing)*, Vol 6., No. 4, pp. 245-256.

Baldwin, D.F., Jan. 1994, *Microcellular Processing and the Design of a Continuous Sheet Processing System*, Ph.D. Thesis, Department of Mechanical Engineering, Massachusetts Institute of Technology, Cambridge, MA.

Bird R.B, Armstrong, R.C., Hassager, O., 1977, *Dynamics of Polymeric Liquids, Vol. 1. Fluid Mechanics*. John Wiley and Sons, New York.

Cha, S.W., April 1994, *A Microcellular Foaming/Forming Process Performed at Ambient Temperature and a Super-Microcellular Foaming Process*, Ph.D. Thesis, Department of Mechanical Engineering, Massachusetts Institute of Technology, Cambridge, MA.

Collias, D.I. and Baird, D.G., 1992, "Does a Microcellular Structure Improve the Modulus of Toughness of a Polymer Matrix," *Society of Plastics Engineers Technical Papers*, Vol. 38, pp. 1532-1535.

Colton, J.S., 1985, *The Nucleation of Microcellular Thermoplastic Foam*, Ph.D. Thesis, Department of Mechanical Engineering, Massachusetts Institute of Technology, Cambridge, MA.

Colton, J.S. and Suh, N.P., 1986, "The Nucleation of Microcellular Thermoplastic Foam: Process Model and Experimental Results," *Advanced Manufacturing Processes*, Vol. 1, No. 3/4, pp. 341-364.

Colton, J.S. and Suh, N.P., 1987a, "The Nucleation of Microcellular Thermoplastic Foam with Additives: Part I: Theoretical Considerations," *Polymer Engineering and Science*, Vol. 27, No. 7, pp. 485-492.

Colton, J.S. and Suh, N.P., 1987b, "The Nucleation of Microcellular Thermoplastic Foam with Additives: Part II: Experimental Results and Discussion," *Polymer Engineering and Science*, Vol. 27, No. 7, pp. 493-499.

Colton, J.S. and Suh, N.P., 1987c, "Nucleation of Microcellular Foam with Additives: Theory and Practice," *Polymer Engineering and Science*, Vol. 27, No. 7, pp. 500-503.

Colton, J.S., August 1988, "Making Microcellular Foams From Crystalline Polymers," *Plastics Engineering*, pg. 53-55.

Colton, J.S., 1989, "The Nucleation of Microcellular Foams in Semi-crystalline Thermoplastics," *Material and Manufacturing Processes*, Vol. 4, pp. 253-262.

DuPont FEP 4100 Material Data Sheet.

DuPont *Extrusion Guide for Melt-Processible Fluoropolymers*, #H-28461-2, pp. 1-41.

DuPont PFA 440 HP Material Data Sheet.

Durril, P.L. and Griskey, R.G., 1969, "Diffusion and Solution of Gases in Thermally Softened or Molten Polymers: Part I," *A.I.Ch.E. Journal*, Vol. 12, No. 6, pp. 1147-1151.

Durril, P.L. and Griskey, R.G., 1969, "Diffusion and Solution of Gases in Thermally Softened or Molten Polymers: Part II," *A.I.Ch.E. Journal*, Vol. 15, No. 1, pp. 106-110.

French, H.F., December 1994, "Making Environmental Treaties Work," *Scientific American*, pp. 94-97.

Gibson, L.J. and Ashby, M.F., 1988, *Cellular Solids: Structure and Properties*. Pergamon Press, New York, pp. 7.

Graff, G., December 1992, "Improving Economics and Replacing CFCs Dominate Polyurethanes," *Modern Plastics*, pp. 44-47.

Graff, G., ed., Mid-November 1993 Issue, *Modern Plastics Encyclopedia '94 & Buyer's Guide Issue*. McGraw-Hill, Inc., Vol. 70, No. 12., New York, pp. 24-45.

Hensen, F., ed., 1988, *Plastics Extrusion Technology*. Oxford University Press, New York, pp. 433-440.

Herrmann, T., May 1994, *Extrusion of Microcellular Plastics: Design Issues for Implementation and Scale-up*, Thesis, University of Stuttgart, Germany and Department of Mechanical Engineering, Massachusetts Institute of Technology, Cambridge, MA.

Herrmann, T., March 1995, *The Role of a Gear Throttle as a Nucleation Device in Continuous Supermicrocellular Polymer Extrusion*, Diploma Engineer's Thesis, University of Stuttgart, Germany and Department of Mechanical Engineering, Massachusetts Institute of Technology, Cambridge, MA.

John, S.S., May 1994, *Microcellular Foaming of Fluorinated Ethylene Propylene and Perfluoroalkoxy*, S.B. Thesis, Department of Mechanical Engineering, Massachusetts Institute of Technology, Cambridge, MA.

Juran, R., ed., Mid-October 1990 Issue, *Modern Plastics Encyclopedia '91*. McGraw-Hill, Inc., Vol. 67, No. 11, New York, pp. 26-70.

Kumar, V., 1991, "Synthesis and Processing of Microcellular Plastics: A Review," *Processing and Manufacturing of Composite Materials*, PED-Vol. 49/MD-Vol. 27, ASME, pp. 185-195.

Levy, Sidney, 1981, *Plastics Extrusion Technology Handbook..* Industrial Press, Inc., New York, pp. vii.

Martini, J.E., 1981, *The Production and Analysis of Microcellular Foam*, S.M. Thesis, Department of Mechanical Engineering, Massachusetts Institute of Technology, Cambridge, MA.

Martini, J.E., Waldman, F.A., and Suh, N.P., 1982, "The Production and Analysis of Microcellular Thermoplastic Foam," *Society of Plastics Engineers Technical Papers*, Vol. 28, pp. 674-676.

Ohanian, Hans C., 1989, *Physics, Second Edition, Vol. II Expanded.* W.W. Norton and Co., New York, pp. 626-630, 662-674.

Park, C.B., May 1993, *The Role of Polymer/Gas Solutions in Continuous Processing of Microcellular Polymers*, Ph.D. Thesis, Department of Mechanical Engineering, Massachusetts Institute of Technology, Cambridge, MA.

Quantum Chemical Corporation Petrothene 1610-PF Material Data Sheet.

Rubin, Irvin I., 1990, *Handbook of Plastic Materials and Technology.* John Wiley and Sons, Inc., New York, pp. 93-340.

Seeler, K.A., and Kumar, V., 1992, "Fatigue of Notched Microcellular Polycarbonate," *Cellular Polymers*, MD-Vol. 38, ASME, pp. 93-108.

Seeler, K.A., and Kumar, V., 1993, "Tension-Tension Fatigue of Microcellular Polycarbonate: Initial Results," *Journal of Reinforced Plastics and Composites*, Vol. 12, pp. 359-376.

Society of Plastics Industry, Inc., 1992, *Guide to the Safe Handling of Fluoropolymer Resins.*

Suh, N.P., 1990, *The Principles of Design.* Oxford University Press, New York.

Tadmor, Z and Gogos, C.G., 1979, *Principles of Polymer Processing.* John Wiley and Sons, New York.

Tensolite, 1974, *Product and Technical Handbook, 2nd Edition*, Carlisle Corp., pp. 130-135.

Times Wire and Cable, 1972, *RF Transmission Line Catalog and Handbook*, #TL-7, p. 2.

Union Carbide DFD-6005 Natural Material Data Sheet.

Van Krevelen, D.W., 1990, *Properties of Polymers*, Elsevier, New York.

Verein Deutscher Ingenieure Gesellschaft Kunststofftechnik, 1979, *Films, Woven and Nonwoven Fabrics made from Polypropylene*, VDI-Verlag, Dusseldorf, pp. 13.

Vukalovich, M.P. and Altunin, V.V., 1968, *Thermophysical Properties of Carbon Dioxide*, translated by Gaunt, D.S., Collet's (Publishers) Ltd., London, pp. 1-72.

Whelan, T. and Dunning, D., 1988, *The Dynisco Extrusion Processors Handbook, 1st Edition.* Dynisco, Inc., pp. 126.

# APPENDIX A
# EXPERIMENTAL SETUPS FOR BATCH PROCESSING

## A.1 Weight Gain and Low Pressure Saturation Setup

The following setup was used for the weight gain experiments of section 3.2 and the batch foaming experiments of section 3.3.1.

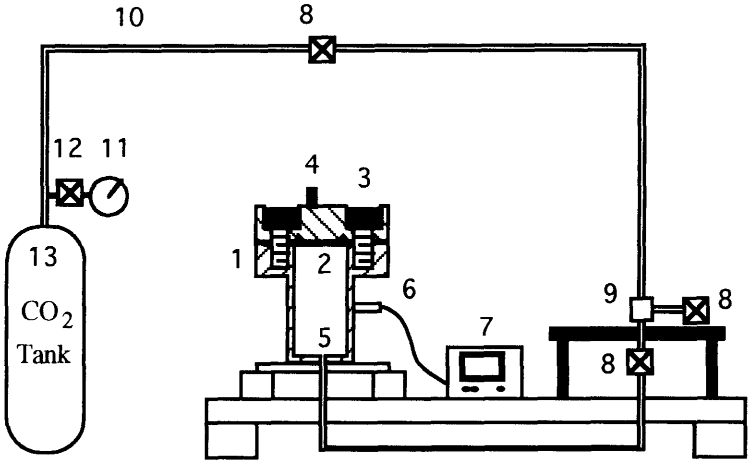

*Figure A.1: Experimental setup for weight gain and batch processing experiments.*

Bill of materials for pressure vessel setup

1) Autoclave Engineers Pressure Vessel Assembly (DD050SS03) (572 ml)
2) Autoclave Engineers Diamond Seal (202B-6815)
3) Autoclave Engineers Hex Socket Head Cap Screw (P-9342)
4) Oseco Over Pressure Rupture Disc (J-2288-01) (3/16 Inconel, 3240 psig @ 72°F)
5) DuPont FEP 4100 and PFA 440 HP Samples
6) Omega Engineering Type J Thermocouple
7) Omega Engineering Temperature Controller (CN 9000)
8) Whitey Integral Bonnet Needle Valve (SS-1VS4)

9) Swagelok Union Tee (SS-400-3)
10) 316 Stainless Steel Tubing (1/4 in O.D., 0.065 in wall thickness)
11) Matheson Pressure Gauge (P/N 63-9123)
12) Matheson Regulator Valve (3-320)
13) $CO_2$ Tank (2370 $in^3$ capacity)

## A.2 Supercritical Fluid Saturation Setup

The following setup was used for the supercritical batch foaming experiments of section 3.3.2.

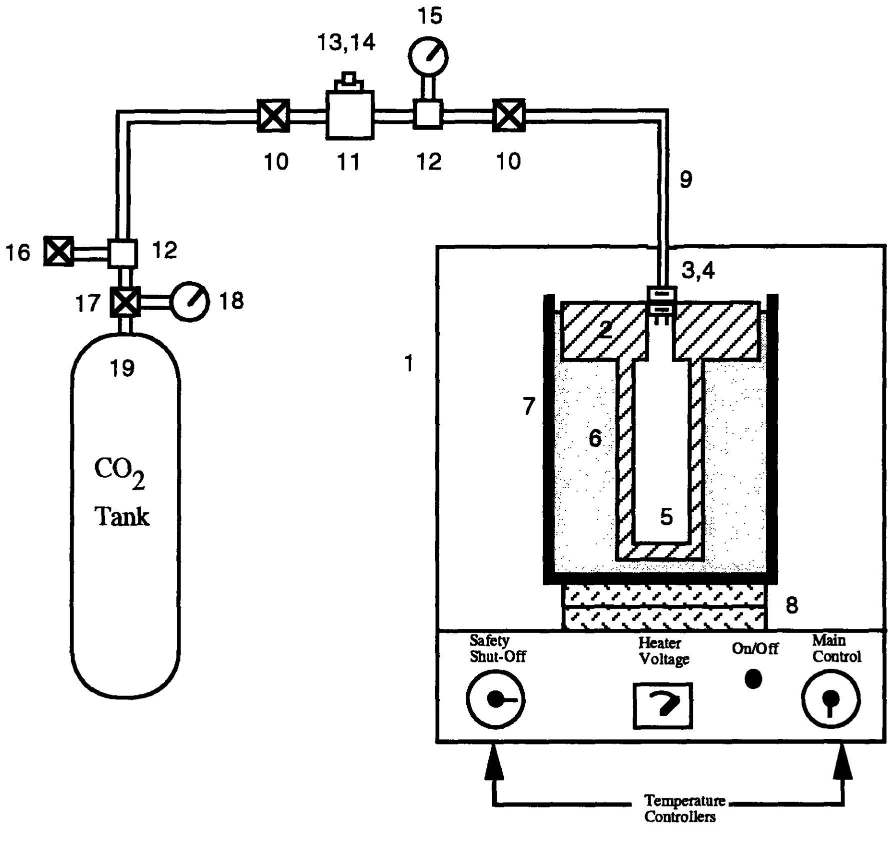

*Figure A.2: Experimental setup for supercritical batch processing.*

Bill of materials for supercritical pressure vessel setup

1) Blue M Constant Temperature Cabinet (D-2631)
2) Pressure Vessel (310 Stainless Steel)
3) Swagelok Nut (SS-402-1)
4) Swagelok Male Connector (SS-400-1-8)
5) DuPont FEP 4100 and PFA 440 HP Samples
6) Ice Bath
7) Polyethylene Container
8) Aluminum Plates
9) 316 Stainless Steel Tubing (1/4 in O.D., 0.065 in wall thickness)
10) Whitey Severe Service Needle Valve (SS-3HNBS4) (10,000 psi)
11) Autoclave Engineers Tee (ST4440-1/4)
12) Swagelok Union Tee (B-400-3)
13) Autoclave Engineers Safety Head Assembly (SS4600 1/4A)
14) Autoclave Engineers Over Pressure Rupture Disc (P-7339 1/4A) (10,000 psi)
15) Matheson Pressure Gauge (P/N 63-3175)
16) Nupro H Series Bellows Sealed Valve (B-4HK)
17) Matheson Regulator Valve (3-320)
18) Matheson Pressure Gauge (P/N 63-9123)
19) $CO_2$ Tank (2370 $in^3$ capacity)

# APPENDIX B

# SUBSYSTEMS FOR SCALED-UP EXTRUSION SYSTEM

## B.1 Water Cooling System

Figure B.1 presents the bill of materials for the water cooling system.

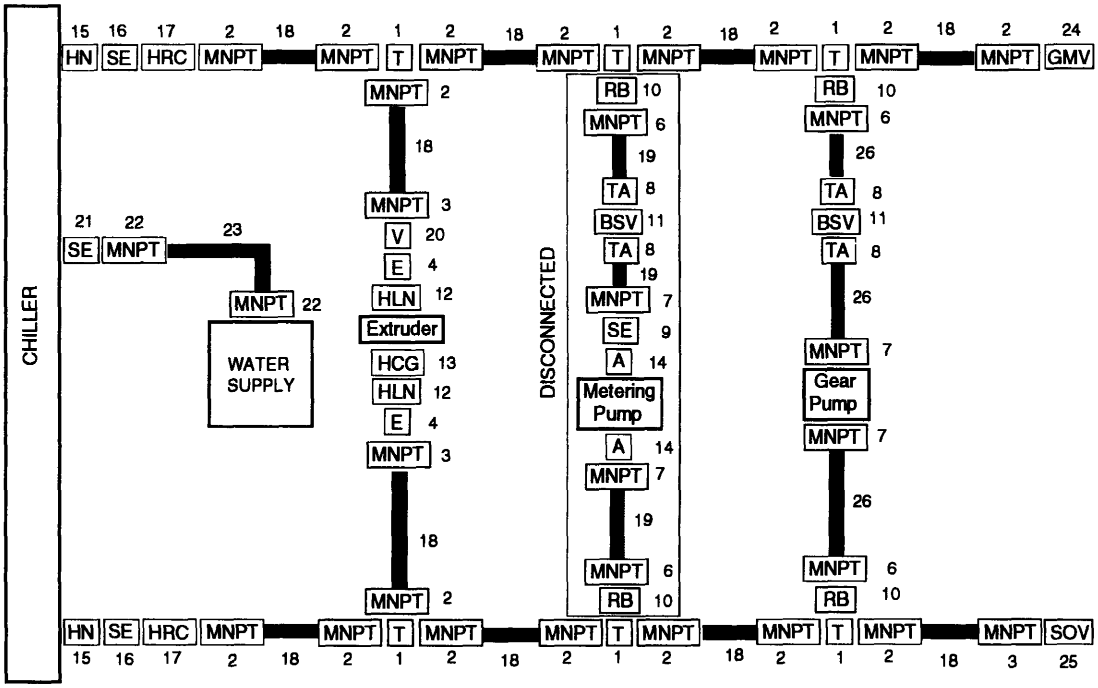

1. B-12-T [Cajon Tee]
2. B-12-HC-1-12 [Swagelok Male NPT]
3. B-12-HC-1-8 [Swagelok Male NPT]
4. B-8-E [Cajon Elbow]
5. B-12-E [Cajon Elbow]
6. B-4-HC-1-4 [Swagelok Male NPT]
7. B-4-HC-1-2 [Swagelok Male NPT]
8. B-4-HC-A-401 [Swagelok Tube Adapter]
9. B-2-SE [Cajon Street Elbow]
10. B-12-RB-4 [Cajon Reducing Bushing]
11. B-4-HK [Nupro H Series Bellows Sealed Valve]
12. B-8-HLN-2 [Cajon Hex Long Nipple]
13. B-8-HCG [Cajon Hex Coupling]
14. SS-2A-2RS [Swagelok Adapter]
15. B-16-HN-16RS [Cajon Hex Nipple]
16. B-16-SE [Cajon Street Elbow]
17. B-16-HRCG-12 [Cajon Hex Reducing Coupling]
18. Reinforced Rubber Hose [3/4 ID, 1-3/16 OD] (McMaster-Carr #5304K44)
19. Nylon Braided Rubber Hose [1/4 ID, 3/8 OD] (McMaster-Carr #5394K16)
20. 1/2 NPT Garden Valve
21. 45 Degree Street Elbow [1/2 NPT]
22. B-10-HC-1-8 [Swagelok Male NPT]
23. Garden Hose [5/8 ID, 3/4 OD]
24. Garden Metering Valve [3/4 NPT]
25. Shutoff Valve [1/2 NPT]
26. Viton Rubber Tubing [1/4 ID, 3/8 OD, Durometer 75] (McMaster-Carr #5119K13)

*Figure B.1: Schematic of the water cooling system.*

## B.2 Carbon Dioxide Metering System

Figure B.2 presents the bill of materials for the carbon dioxide metering system.

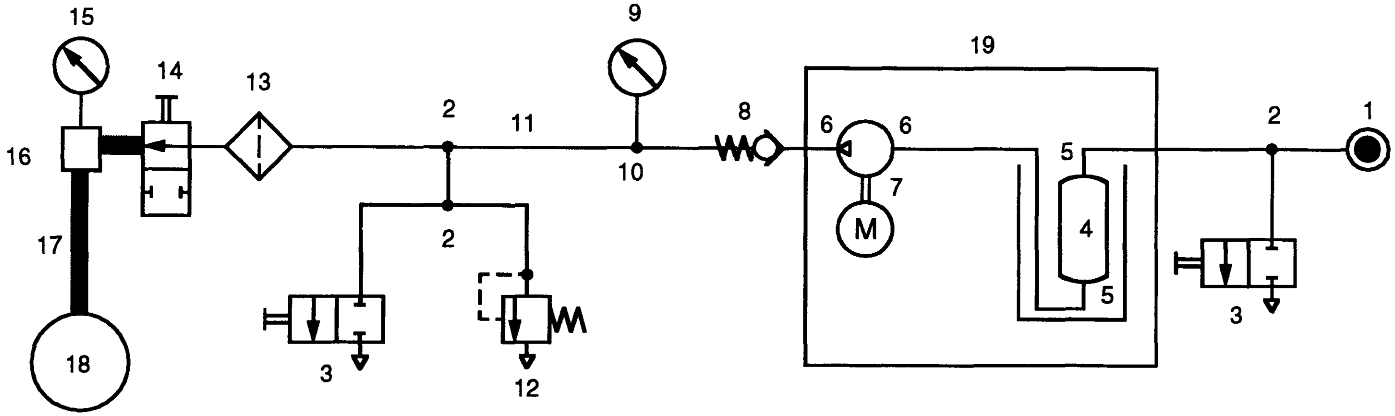

1. Carbon Dioxide Tank
2. Swagelok Union Tee (SS-400-3)
3. Nupro Bellows Sealed Valve (SS-4H)
4. Stainless Steel Liquefaction Chamber
5. Swagelok Male Connector (SS-400-1-8)
6. Swagelok Male Connector (SS-400-1-4)
7. Lewa Metering Pump (FCM 08)
8. High Pressure Equipment Co. Soft Seat Check Valve (10-41AF4-T)
9. Omega Pressure Transducer (PX300-7.5KGV) with Pressure Snubber (PS-4G)
10. Swagelok Female Branch Tee (SS-400-3-4TTF)
11. 316 Stainless Steel Tubing (1/4 in OD, 0.065 in wall thickness)
12. Nupro Relief Valve (SS-4R3A) with 4000-5000 psi Spring (177-R3A-K1-G)
13. High Pressure Equipment Co. Line Filter (10-51AF4)
14. High Pressure Equipment Co. Two Way Angle High Temperature Valve (30-12HF4-HT)
15. Dynisco Pressure Transducer (PT460EH-10M-6)
16. Injection Stem with 110 Viton O-Ring (3/8 ID, 9/16 OD, 3/32 Cross Section)
17. Briskheat Flexible Heating Tape (BWH 102-060) 1" wide, 6' long, 940W, 240V
18. Royle 1" Bronfin Extruder (Serial #5783)
19. General Electric Compact Freezer (CB5DM)

*Figure B.2: Schematic of the carbon dioxide metering system.*

## B.3 Safety Containment System

Polycarbonate sheets obtained from General Electric Plastics were used to fabricate a safety containment system to protect the operator in the event of an extruder or metering system explosion. The different views of the containment device are shown in Figure B.3. Many bolt holes and valve/tubing openings not pictured in these drawings were also drilled into these sheets. The polycarbonate sheets were 3/8 inch thick and fastened with 14 gauge steel angles (McMaster-Carr #4664T33), 14 gauge galvanized steel gusset plates (McMaster-Carr #4664T22), and 3/8-16 inch nuts and bolts. The steel angles measured 2-1/4 inches by 1-1/2 inches by 10 feet.

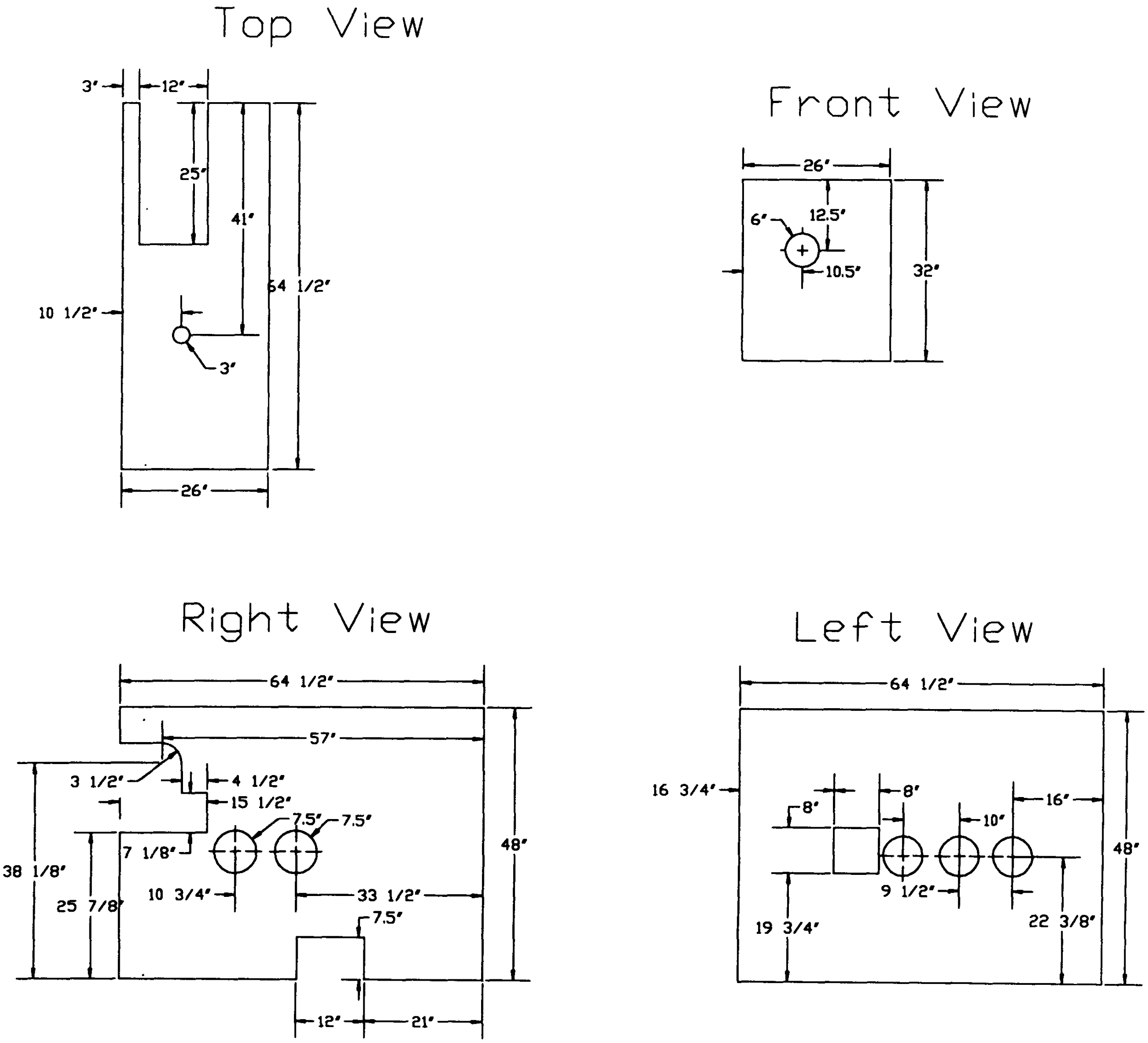

Top View

Front View

Right View

Left View

*Figure B.3: Different views of the safety containment system.*

## B.4 Gear Pump Leveling Stand

A 6061-T6 aluminum stand reinforced with steel angle irons was designed to assure precise alignment of the extruder outlet to the gear pump inlet flow channel. A schematic of the leveling stand is shown in Figure B.4 while the upper base and lower base are shown in Figures B.5 and B.6, respectively. As mentioned in section 4.2.2, the gear pump base was bolted down to the upper aluminum base by three 1/2-13 bolts while three additional 1/2-13 bolts came from underneath the upper base and contacted the underside surface of the gear pump base. Adjustment of the latter three bolts varies both the height and the angular orientation of the gear pump.

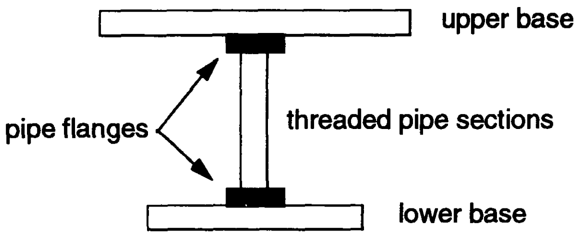

*Figure B.4: Schematic of the gear pump leveling stand.*

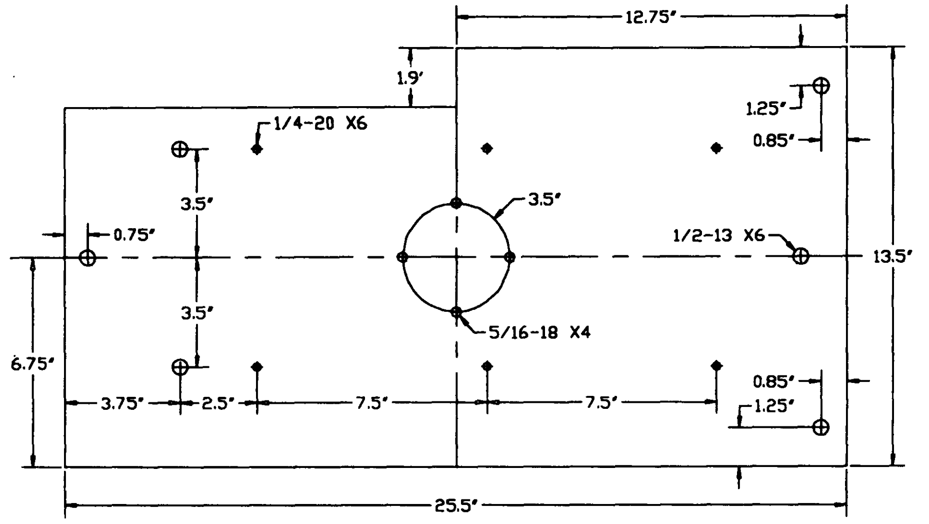

*Figure B.5: Schematic of the upper base.*

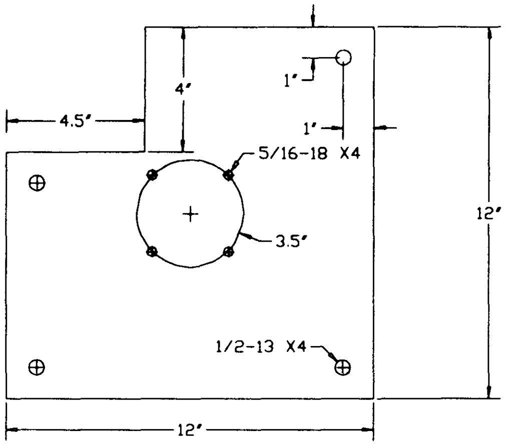

*Figure B.6: Schematic of the lower base.*